Dissertation

submitted to the

Combined Faculties for the Natural Sciences and for Mathematics

of the Ruperto–Carola University of Heidelberg, Germany

for the degree of

Doctor of Natural Sciences

presented by

Sofia Lianou

Born in Peristeri, Greece

Oral examination: 31st January 2011

THE INTERACTING M 81 GROUP OF GALAXIES

Referees: Prof. Dr. Eva K. Grebel
Prof. Dr. Norbert Christlieb

Αφιερωμενο με πολυ αγαπη στη μητερα μου,
στον αδερφο μου και στις ανηψιες μου

Zusammenfassung

Das Thema dieser Arbeit ist die Rolle der Umgebung und Wechselwirkungen auf die Entstehung und Entwicklung von Zwerggalaxien in nahegelegenen Gruppen. Die M 81-Gruppe ist eine hochgradig wechselwirkende Gruppe, die eine einzigartige Gelegenheit bietet, den Einfluss der Umgebung auf die Eigenschaften ihrer Zwerggalaxienpopulation zu studieren. Wir verwenden die Tully–Fisher–Relation, um nach mglichen Gezeiten-Zwerggalaxien in der M 81-Gruppe zu suchen. Keine potentiellen Gezeiten-Zwerggalaxien wurden identifiziert. Darber hinaus leiten wir photometrische Metallizitäts–Verteilungsfunktionen her und untersuchen die Gegenwart von Metallizitätsgradienten bei neun Zwerggalaxien frühen Typs der M 81-Gruppe. Der Vergleich ihrer mittleren Metallizitätseigenschaften mit denen der Zwerggalaxien in der lokalen Gruppe zeigt, dass diese sich ähneln. Nicht alle der Zwerggalaxien weisen einen Metallizitätsgradienten auf, wie es für die Zwerggalaxien der lokalen Gruppe der Fall ist. Der Anteil an leuchtkräftigen AGB-Sternen in jeder Zwerggalaxie ist gering, während ihr Bruchteil als Funktion ihres Abstandes von der Galaxie M 81 keinerlei Trend zeigt. Die Resultate deuten darauf hin, dass die untersuchten Eigenschaften durch interne Prozesse beeinflusst werden. Schließlich wurde unter Verwendung der Galaktischen kugelförmigen Zwerggalaxien die Methode der Herleitung der photometrischen Metallizitäten für Zwerggalaxien ausgewertet, die komplexe Sternentstehungsgeschichten aufweisen. Die resultierenden mittleren photometrischen Metallizitätseigenschaften befinden sich in guter Übereinstimmung mit spektroskopischen Messungen, während die Unterschiede in den individuellen Sternen größer werden, je komplexer die Sternentstehung ist.

Abstract

The topic of this Thesis is the role of the environment and interactions on the formation and evolution of dwarf galaxies in nearby groups. The M 81 group is a highly interacting group, offering a unique opportunity to study the impact of the environment on shaping the properties of its dwarf galaxy population. We use the Tully–Fisher relation to search for potential tidal dwarf galaxies in the M 81 group. No potential tidal dwarfs were identified. Furthermore, we derive photometric metallicity distribution functions and examine the presence of metallicity gradients for nine early–type dwarf galaxies of the M 81 group. The comparison of their mean metallicity properties with those of Local Group dwarfs shows that these are similar. Not all of the dwarfs show a metallicity gradient, as is also the case of Local Group dwarfs. The fraction of luminous asymptotic giant branch stars in each dwarf is small, while their fraction as a function of their distance from the M 81 galaxy does not show any trend. The results indicate that the studied properties are affected by internal processes. Finally, the method of deriving photometric metallicities is evaluated for dwarf galaxies with complex star formation histories,

using Galactic dwarf spheroidals. The resulting mean photometric metallicity properties are in good agreement with spectroscopic measurements, while individual star differences become larger the more complex the star formation is.

Contents

List of Figures

List of Tables

Chapter 1

Introduction

Dwarf galaxies are the dominant galaxy population in groups and in clusters of galaxies. Their morphological types comprise both early– and late–type dwarf galaxies. Early–type dwarfs include dwarf ellipticals and dwarf spheroidals, while late–type dwarfs include dwarf irregulars and blue compact dwarfs. The main difference between these two morphological types is their gas content and star formation activity. The late–type dwarfs are gas–rich objects and have on–going star formation, while the early–type dwarfs do not have enough gas left and thus do not show any on–going star formation (Grebel 1999; Mateo 1998; Tolstoy, Hill & Tosi 2009).

The group that our Galaxy resides in is the Local Group. The Local Group consists of a few massive galaxies, but the majority of its constituents are dwarf galaxies. Detailed photometric studies of the Local Group dwarf galaxies have shown that these objects experienced a variety of star formation histories: while all of them contain an old ($\geq$10 Gyr) stellar population, they contain different fractions of young ($\leq$1 Gyr) and intermediate age (1 Gyr up to less than 10 Gyr) stars (Grebel & Gallagher 2004). In addition, detailed photometric and spectroscopic studies have shown that the mean metallicities and metallicity spreads of Local Group dwarf galaxies cover a wide range of values, with the tendency of dwarf spheroidal galaxies to have higher stellar metallicities when compared to the dwarf irregular ones, at a fixed optical luminosity (Grebel, Gallagher & Harbeck 2003). Furthermore, some dwarfs show a strong population or metallicity gradient, in the sense that the young or metal rich populations are concentrated towards the center of the dwarf galaxy, while other dwarfs do not show such a gradient (e. g., Harbeck et al. 2001; Koch et al. 2007). Interestingly, the population gradients and the metallicity–luminosity relation are well understood in terms of the potential wells that can retain more metals and sustain star formation the deeper they are (more massive galaxies). On the other hand, the large variety of star formation histories is dependent on many factors and not simply understood: the environment in which the dwarf galaxies live may drive their evolutionary histories, or their orbital properties or

internal processes may play a major role.

Since the star formation and chemical evolution histories of the Local Group dwarf galaxies are determined in progressively greater detail, the next step would be to compare their properties with the ones of other nearby groups with very different environments. The motivation for this work is to explore the impact of the environment on the formation and evolution of dwarf galaxies, by studying the dwarf galaxy population of the nearby M 81 group of galaxies.

1.1 The M 81 group of galaxies

The M 81 group of galaxies, which is named after the M 81 galaxy sitting at the center of the group, is one of the nearest groups with a mean distance of $\sim$ 3.7 Mpc (Karachentsev et al. 2002). It is embedded in an extended filament of galaxies and includes the galaxies which are centered around NGC 2403 and around NGC 4236, the two brightest galaxies along with the galaxy M 81. The M 81 group contains about 50 dwarfs of both early– and late–type (Chiboucas, Karachentsev & Tully 2009). This number should be considered as a lower limit, since the discovery of the very faintest and lowest surface brightness galaxies depends on the detection limit of the survey, as well as on the area on the sky covered by the survey (Koposov et al. 2008; Chiboucas, Karachentsev & Tully 2009). As an example, the number of the Local Group members has been significantly increased owing to the Sloan Digital Sky Survey and other surveys, going from roughly 40 dwarfs prior to these surveys to now roughly 60 dwarfs known, and this number is expected to increase even more with future surveys that cover a wider range of the sky (Jerjen 2010; Willman 2010).

The M 81 group resembles the Local Group in many ways, e. g., in its overall morphological galaxy content, but it stands out in one respect: the M 81 group is a highly interacting group. Atomic hydrogen observations have revealed gaseous bridges which connect the three core galaxy members of the group, namely M 81, M 82 and NGC 3077 (Appleton, Davies & Stephenson 1987; Yun, Ho & Lo 1994). An HI map of the central region of the M 81 group, which includes the three main interacting galaxies, is shown in the lower panel of Fig. 1.1, adopted by Yun, Ho & Lo (1994). The tidal bridge towards the south connects the M 81 galaxy with NGC 3077, while the one towards the north connects NGC 3077 and M 82, as seen in the lower panel of Fig. 1.1. The Digitized Sky Survey optical image of the same central region is shown in the upper panel of Fig. 1.1 and shows no evidence of any tidal interactions occurring among these three galaxies. Numerous HI clouds have been detected to be bound to the group and are located along these gaseous streams, thus their origin is thought to be associated with the recent interactions of the group (Brinks, Walter & Skillman 2008; Chynoweth et al. 2008), which occurred within the last 300 Myr (Yun 1999).

The strongly interacting environment makes the M 81 group an important nearby laboratory to study

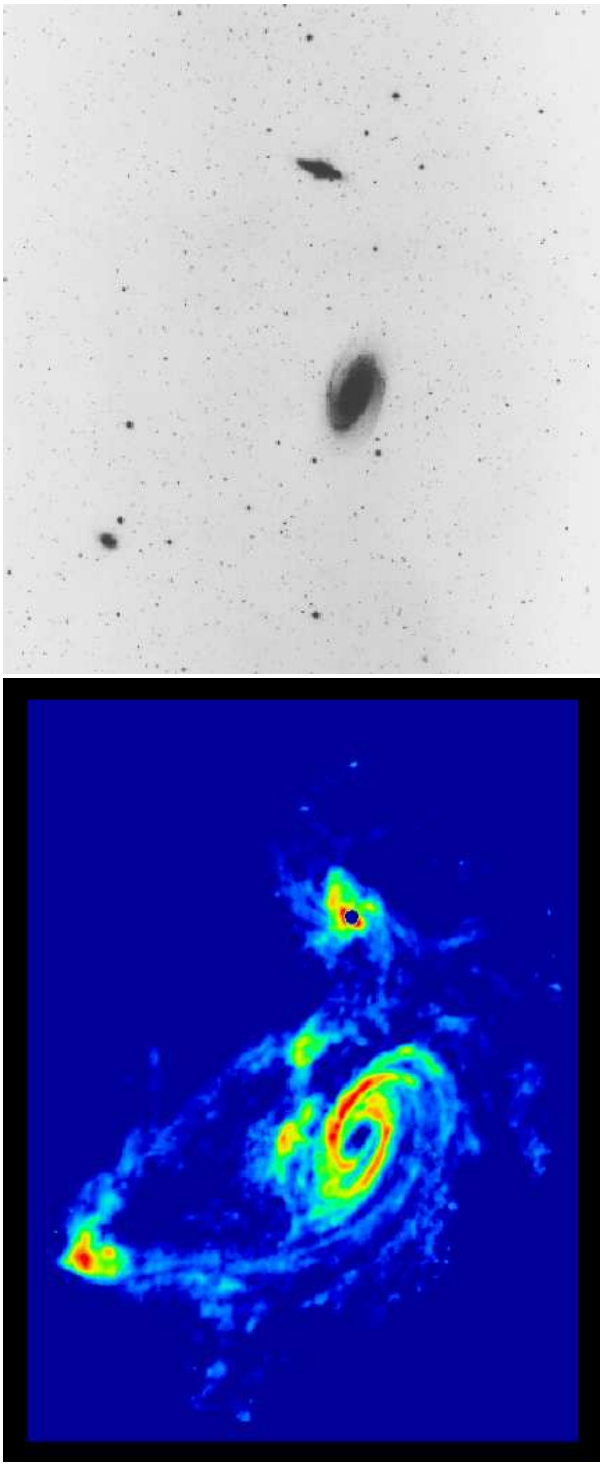

Figure 1.1: The upper panel shows a Digitized Sky Survey optical image of the central region of the M 81 group that includes the galaxies M 81, M 82 and NGC 3077. The lower panel shows an HI map covering the same region and reveals the gaseous tidal bridges that connect the three core members of the group. North is up and east is towards the left. The central object is M 81, the south–eastern is NGC 3077, while M 82 is towards the north. The figure is adopted from Yun, Ho & Lo (1994).

environmental effects and the role of interactions in the formation and evolution of its dwarf galaxy population. It has been suggested that dwarf galaxies may be formed in these tidal streams, thus presenting the opportunity to study the formation of such tidal dwarf galaxies within this nearby group. Tidal dwarf galaxies are bound systems that are formed from the nearly dark matter–free material expelled from the disk of their parent galaxy during the tidal interaction with a companion galaxy (Bournaud et al. 2007; and references therein). Due to their formation mechanism, tidal dwarf galaxies are expected to contain little, if any, dark matter. This is their most important distinguishing characteristic from other dwarfs, such as dwarf spheroidals which are likely the most dark matter dominated systems in the universe with M / L ratios several 100s (e. g. Mateo 1998). In addition, since tidal dwarf galaxies are formed from the recycled material of their parent galaxy, they are expected to be metal enriched and to have unusually high metal abundances for their luminosity (Duc & Mirabel 1998), in the case of recent interactions where the signs of interactions are still detectable. In the case where an interaction is not obvious and given that the star formation history of the potential tidal dwarf galaxy would further shape its chemical evolution history, the stellar metallicity of the tidal dwarf galaxy may be compared to the stellar metallicity of its parent galaxy, although in this case tracing the parent galaxy may be a challenge.

There have been several potential tidal dwarf galaxies identified in the M 81 group as well as new stellar groupings. The tidal dwarf galaxy candidates include Holmberg IX and Garland (Makarova et al. 2002; Sabbi et al. 2008; Croxall et al. 2009). These were identified as such by examination of their stellar populations and through their gas phase metallicities. Stellar populations analyses can indicate whether there is recent star formation occurring in the tidal dwarf galaxy candidate. The onset of the recent star formation should be later than the epoch of the interaction between the parent galaxies of the tidal dwarf galaxy candidate. One difficulty with identifying tidal dwarf galaxy candidates using their resolved stellar populations is that there is an old population present, in addition to the recent star formation. A tidal dwarf galaxy inherits this old population from its parent disk galaxy, while the fraction of this old population can reach up to 40% (Elmegreen, Kaufman & Thomasson 1993; Hunter, Hunsberger & Roye 2000). Numerical simulations for the M 81 group of galaxies show that the interactions have occurred within the last 300 Myr (Yun 1999). The ages inferred for the recent stellar populations in the case of Holmberg IX and Garland are consistent with the ages inferred through the numerical simulations (Makarova et al. 2002; Sabbi et al. 2008). In the case of their gas phase metallicities, when placing these two objects, Holmberg IX and Garland, on the metallicity–luminosity relation, they appear too metal rich compared to other group objects of the same luminosity with available metallicities (Croxall et al. 2009). Furthermore, their gas phase metallicities are similar to the gas phase metallicity of the M 81 galaxy. Therefore, their gas phase metallicities are consistent with Holmberg IX and Garland having formed from the enriched material of the M 81 galaxy.

Within the Local Group and on a smaller scale, the Large and Small Magellanic Clouds (LMC and SMC, respectively) can be considered as the closest extragalactic interacting galaxies. Specifically, the Magellanic Bridge in between them indicates that they are interacting with each other and the Magellanic Stream and Leading Arm additionally indicate an interaction of the Magellanic System as a whole with the Galaxy (Putman et al. 1998; 2003). The proposed physical mechanisms responsible for the observed streams include ram pressure stripping and tidal interactions. The Leading Arm identified by Putman et al. (1998) argues in favour of a tidal interaction between the Magellanic system and the Galaxy as the dominant mechanism. However, new proper motion measurements place the LMC–SMC system either on their first approach towards the Galaxy or on a long period eccentric orbit (Kallivayalil et al. 2006a, 2006b; Piatek, Pryor & Olszewski 2008; Besla et al. 2010), which would make tidal interaction between the Magellanic System and the Galaxy an unlikely primary mechanism for creating the Magellanic Stream and Leading Arm. Another scenario consistent within the proper motion measurements is that the LMC and SMC are not bound to each other, but that the SMC came in to the Local Group for the first time and while passing by the LMC, it triggered their interactions (Kallivayalil et al. 2006b). An alternative formation mechanism for the Magellanic Stream and Bridge is that they originate purely from an interaction between the LMC and the SMC, with no need to have interacted with the Galaxy a priori, and this mechanism agrees with the recent results of the Magellanic Clouds proper motion measurements (Besla et al. 2010). This formation mechanism needs in addition ram pressure stripping in order to shape the Magellanic Stream and the Leading Arm in their observed form.

Ram pressure is the pressure that a gas–rich galaxy feels when it moves through the intergalactic medium of a group or a cluster of galaxies. During this process, the gaseous component of the galaxy is affected by stripping, if the ram pressure is higher than the gravitational pressure which binds the gas to the disk (Gunn & Gott 1972; for a review Boselli & Gavazzi 2006):

$$\rho_{\rm IGM} V_{gal}^2 \geq 2\pi G \Sigma_{star} \Sigma_{gas}, \tag{1.1}$$

where $\rho_{\rm IGM}$ is the density of the intergalactic medium, V_{gal} is the velocity of the galaxy in the group or cluster of galaxies, $\Sigma_{\rm star}$ is the surface density of the stars, and $\Sigma_{\rm gas}$ is the surface density of the gas.

In the Local Group, the atomic hydrogen distribution of the isolated dwarf irregular galaxy Pegasus at the distance of 919 kpc from the Galaxy is reported to have a cometary appearance, which is attributed to the ram pressure stripping by the intra–group medium of the Local Group (McConnachie et al. 2007). This result is evidence for the existence of a Local Group intra–group medium with an estimated density at the distance of Pegasus between 10^{-6} to 10^{-5} atoms per cm^3 (McConnachie et al. 2007). However, recent studies by Kniazev et al. (2009) of the same galaxy Pegasus dwarf irregular do not confirm such a comet–like appearance and thus the existence of an intra–group medium. In the M 81 group, the atomic hydrogen distribution of the dwarf galaxy Holmberg II at the distance of 475 kpc from the M 81 galaxy

is reported to have a comet–like appearance, suggesting that ram pressure from the M 81 intra–group medium is acting on this dwarf. The estimated density of the M 81 intra–group medium at the distance of Holmberg II is larger than $\sim 10^{-6}$ atoms per cm^3, a value consistent with the X–ray properties of small groups of galaxies (Bureau & Carignan 2002). An alternative explanation for the observed shape of the HI distribution of Holmberg II is that of a tidal interaction with a companion, possibly UGC 4483 (Bureau et al. 2004).

The combination of ram pressure stripping, tidal stirring and cosmic ultra–violet background on gas–dominated dwarf galaxies is invoked in order to explain the origin of the gas–deficient dwarf spheroidals and the fact that that they are observed preferentially in the proximity of a massive galaxy such as the Galaxy or Andromeda (Mayer et al. 2006, 2007; Mayer 2010). The combination of these processes may be responsible for transforming a gas–rich dwarf to a gas–poor dwarf spheroidal, by stripping the gas and transforming the gas–rich dwarf from a rotationally supported to a pressure supported system (but see also Grebel, Gallagher & Harbeck 2003). Tidal stirring is the effect of the repeated tidal forces acting on the dwarf galaxy by the primary galaxy, which can transform the dwarf galaxy from a rotationally–supported to a pressure–supported system (Mayer 2010; and references therein). The onset of the action of ram pressure stripping, tidal stirring and cosmic ultra–violet background on the gas–rich dwarf, or the redshift of the infall of these dwarfs into the halo of a massive galaxy, can explain the observed similarities and differences of the dark matter and stellar population properties among the classical dwarf spheroidals of the Local Group (Mayer et al. 2007; Mayer 2010). In the case of the M 81 group, there is the tendency for the early–type dwarf galaxies to cluster around the M 81 galaxy (Chiboucas, Karachentsev & Tully 2009).

1.2 Resolved stellar populations

Stellar populations that can be photometrically resolved into individual stars provide a very important and powerful tool to infer the evolutionary histories of galaxies. This is even more true in the case of more distant galaxies, where any information through spectroscopy of individual red giants is not possible even with the 8–10 m class telescopes. There are numerous extragalactic surveys that make it possible to study the resolved stellar populations of galaxies even as far as the Virgo cluster distance, owing to the high resolution of the Hubble Space Telescope (Caldwell 2006). At the distance of the Virgo cluster, it is possible to resolve only very luminous red giant and super–giant stars, while for dwarf galaxies within the Local Group it has been able to obtain deep color–magnitude diagrams (CMDs) down to and below the oldest main sequence turn off with the use of Hubble Space Telescope observations. Thus, the more distant an object is the less information one can have from its resolved stellar populations. At the distance of the M 81 group, we can resolve the stars that belong to the red

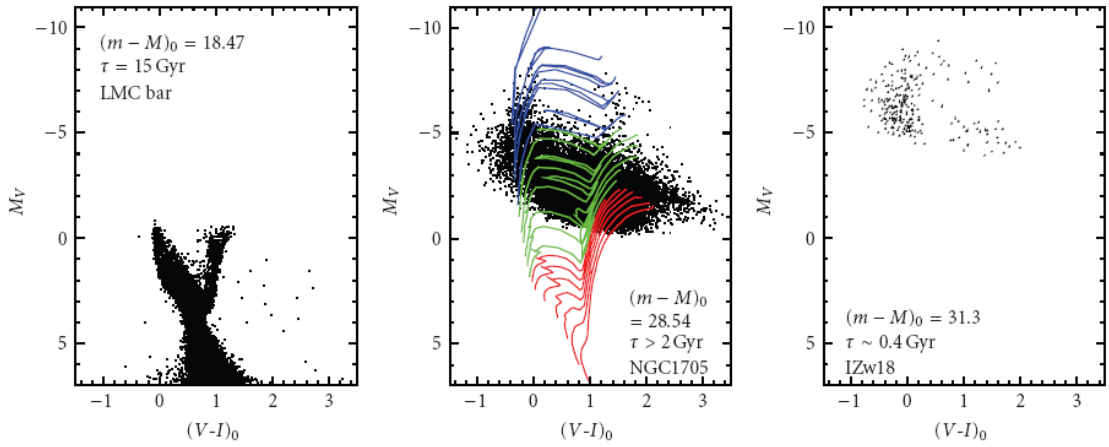

Figure 1.2: The resolvable parts of a galaxy depending on its distance. From left to right, the CMDs in absolute V–band magnitude versus intrinsic color are shown for a nearby late–type galaxy (at a distance of 50 kpc) to more distant late–type galaxies (at distances of 5.1 Mpc and 18 Mpc, respectively). In the middle panel, evolutionary tracks are shown for low–mass stars in red, for intermediate–mass stars in green, and for high–mass stars in blue. The figure is adopted from Cignoni & Tosi (2010). Due to the distance, the stars corresponding to the same evolutionary phase are pushed towards fainter magnitudes, where such an effect becomes obvious in the CMD of the V–band magnitude versus the color. Due to the telescope observational limitations, only the most luminous part can be resolved when going to larger distances. In the first panel, stars brighter than approximately -1 mag are saturated, therefore the corresponding brighter evolutionary phases are not shown.

giant branch, the young main sequence and the blue loop and red super-giant stars. Therefore we can measure ages and metallicities and derive the star formation histories to address the questions raised in the previous section. The part of the CMD that is resolvable in various distances is shown in Fig. 1.2, from left to right for more nearby to more distant galaxies, adopted from Cignoni & Tosi (2010).

A simple stellar population is defined to be composed of stars that have the same age and the same metal abundance. A galaxy is composed of stars of different ages and metal abundances, thus it is far from a simple stellar population. The composite stellar populations present in a galaxy can be regarded as a linear combination of simple stellar populations of different ages and metal abundances. All dwarf galaxies studied so far in detail contain old populations and in addition they may contain intermediate–age or young populations, depending on their star formation histories. Furthermore, the fact that there are populations of different ages present leads to a star–to–star spread in chemical abundances. Alternatively, such spreads in chemical abundances can be generated by inhomogeneous enrichment (Marcolini et al. 2008).

Photometric studies of resolved stellar populations are used in order to derive their star formation and chemical evolution histories. The star formation history can be obtained by comparing the observed

features of a color magnitude diagram (CMD), which is the diagram of the magnitude of a star as a function of its color, with a model CMD. In practise, the density of stars within defined boxes along the observed CMD is compared with the density of the synthetic stars drawn from the model CMD and within the same defined boxes as in the observed CMD (for a review see Aparicio 2002). The boxes are regions in the CMD that have a certain size of color and of magnitude, thus defining a grid in the CMD. The sizes of these boxes in the CMD can be chosen in two ways: either with constant sizes of the color and magnitude (uniform grid), or with variable sizes of the color and magnitude ("a la carta" grid). The former uniform grid is more objective in choosing the sizes of the boxes, while the second "a la carta" grid takes advantage of our a priori knowledge of different evolutionary phases along the CMD, thus sampling in a different way the well and poorly known evolutionary features in the CMD (Aparicio 2002). Synthetic populations are constructed using a set of stellar evolution models, adopting an initial mass function and applying a star formation and a chemical enrichment law (Gallart, Zoccali & Aparicio 2005; Cignoni & Tosi 2010).

The main evolutionary phases a star goes through are the following. The main sequence is the phase where a star spends most of its time and in this phase it burns hydrogen in its core. When the star develops a shell of burning hydrogen around a core of non–burning helium, then this marks the sub–giant branch phase. This phase is very short for intermediate and high mass stars, thus the probability to observe a star in this phase is low. In the red giant branch phase a star, burning hydrogen in a shell and having developed a helium core, undergoes an increase of its luminosity at a constant effective temperature. At the tip of the red giant branch, the onset of the helium burning in the core starts, and in the case of the low mass stars this is done through the helium flash. The horizontal branch phase is when the star burns helium in the core, while in addition there is a shell of hydrogen burning. The phase of burning helium in the core and hydrogen in a shell is called blue–loop in the case of higher mass stars. The asymptotic giant branch phase is when a star has developed a core of carbon and oxygen, while there is a shell of helium and a shell of hydrogen. In the early asymptotic giant branch phase, the main energy input comes from the helium burning in a shell around the carbon–oxygen core. In the thermally–pulsating asymptotic giant branch phase, the energy comes from the hydrogen shell burning with the change from the helium–shell to the hydrogen–shell burning marking the onset of the thermally–pulsating asymptotic giant branch phase. At any metallicity, the stars in the early asymptotic giant branch phase have bluer colors than the stars in the red giant branch phase of the same age. Thus, there is an overlap of the asymptotic giant branch stars that are metal–rich with the red giant branch stars that are slightly more metal–poor, and that would cause a systematic in the determination of the metal abundances using the color of the red giant branch stars.

There are different features in the CMD that can be used as age and metallicity indicators (for a review see Gallart, Zoccali & Aparicio 2005). These features are shown in Fig. 1.3, which shows the

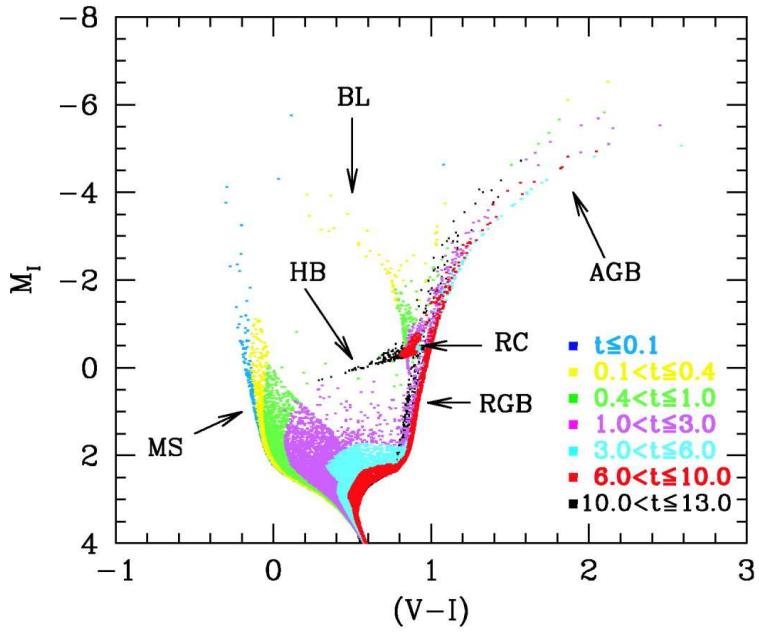

Figure 1.3: The color–magnitude diagram of a synthetic composite stellar population, assuming a constant star formation rate from 13 Gyr ago to date, and a metallicity linearly increasing from Z = 0.0001 to Z = 0.02. The various phases a star goes through during its evolution are marked. The color coding corresponds to stars of different ages. The figure is adopted by Aparicio & Gallart (2004). The phases noted are the following. MS: main–sequence; RGB: red giant branch; RC: red clump; HB: horizontal branch; BL: blue–loop; AGB: asymptotic giant branch.

CMD of a synthetic composite stellar population color coded according to age and is adopted from Aparicio & Gallart (2004). In particular, the main sequence turn–off is a reliable age indicator for a simple stellar population. In galaxies with multiple stellar populations or extended star formation history, the multiple main sequence turn–offs give the age ranges of the populations present in a galaxy. In addition, the blue-most and red-most edges of the main sequence below the oldest main sequence turn–off can be used to infer the metallicity range present in a galaxy. The red giant branch and its slope are rather sensitive to metallicity. The horizontal branch stars can be used to infer the distances, because the horizontal branch luminosity in stellar populations older than approximately 8 Gyr is expected to be independent of age and only mildly dependent on metallicity (Gallart, Zoccali & Aparicio 2005). The asymptotic giant branch stars can serve as a metallicity and a metallicity gradient indicator by estimating the ratio of the carbon stars to the M–type stars (C / M), where the ratio is decreasing with increasing metallicity (Brewer, Richer & Crabtree 1995; Mouhcine & Lancon 2003; Gallart, Zoccali & Aparicio 2005; and references therein). The bolometric luminosity of the tip of the asymptotic giant branch stars can be used to infer the age of the intermediate age stars present (Reid & Mould 1984; Mould & Da Costa 1988; Rejkuba et al. 2006).

The tip of the red giant branch is an important feature in the CMD due to its application as an excellent distance indicator for low mass stars (Lee, Freedman & Madore 1993; Madore & Freedman 1995; Sakai, Madore & Freedman 1996; Salaris & Girardi 2005; and references therein). The tip of the first–ascent red giant branch represents the luminosity of the core helium flash, which is constant and has very little sensitivity to metallicity or age, with the I–band showing the least sensitivity and thus preferred (Lee, Freedman & Madore 1993; Madore & Freedman 1995; Sakai, Madore & Freedman 1996; and references therein). The absolute I–band magnitude of the tip of the red giant branch is equal to approximately -4.0 ± 0.1 mag for the metallicity range of $-2.2 < [\mathrm{Fe/H}] < -0.7$ (dex) (Da Costa & Armandroff 1990; Lee, Freedman & Madore 1993). The tip of the red giant branch as a distance indicator has been calibrated on Galactic globular clusters by Lee, Freedman & Madore (1993) using a revised calibration of Da Costa & Armandroff (1990). Because it forms a discontinuity in the I–band luminosity function, it can be detected by applying an image–processing edge–detection algorithm, with the Sobel filter, i.e. the kernel [-1, -2, 0, +2, +1], the one most commonly used. The Sobel filter when convolved with the I–band luminosity function displays a peak value at the magnitude of the discontinuity, thus allowing to detect the tip of the red giant branch.

Depending on the initial mass of a star, it will evolve along a characteristic path in the Hertzsprung–Russell diagram, which is the theoretical equivalent of the observed CMD, as is shown in Fig. 1.4. In order to transform the theoretical quantities to the observational ones, stellar atmosphere models are used to compute the necessary bolometric corrections in a particular photometric band. According to the initial mass of a star, these are divided in three categories: the low mass stars, the intermediate mass stars, and the high mass stars (for a review Chiosi, Bertelli & Bressan 1992).

Low mass stars ($\leq 2.3\,\mathrm{M}_{\odot}$) are those stars that develop an electron degenerate core composed of helium when they leave the main sequence toward the red giant branch. The stars evolve along the CMD going through the phases of the sub–giant branch, the red giant branch, the horizontal branch, and the asymptotic giant branch. *Intermediate mass stars* ($2.3\,\mathrm{M}_{\odot} \leq \mathrm{M} \leq 7\,\mathrm{M}_{\odot}$) are those stars that develop an electron degenerate core of carbon–oxygen, after the core–He exhaustion, and that experience helium shell flashes or thermal pulses while they go though the asymptotic giant branch phase. The phases the intermediate–mass stars go through are essentially the same as the ones described for the low–mass stars, apart from the phase that the more massive of the intermediate–mass stars go through, which is the blue–loop phase instead of the horizontal branch phase. *High mass stars* ($\geq 7\,\mathrm{M}_{\odot}$) are stars that ignite the carbon non–violently and they develop an iron core, after the core–He exhaustion. These stars go through the sub–giant branch phase after leaving the main sequence and then directly move towards the blue–loop phase.

In early–type dwarf galaxies that contain a mixture of stars with a range of ages and chemical abundances the best way to study their chemical evolution and star formation history is through spec-

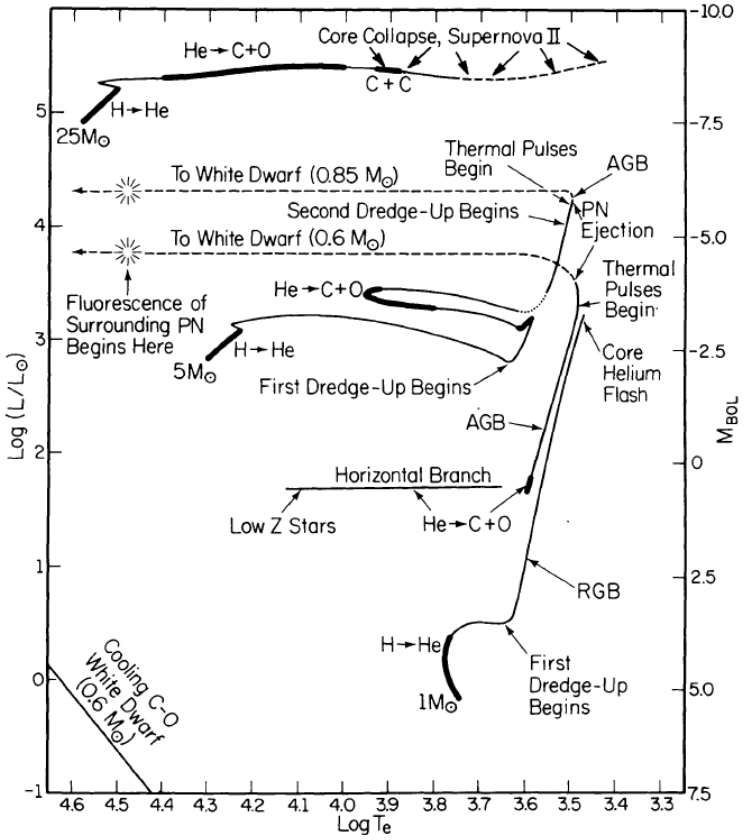

Figure 1.4: The Hertzsprung–Russell diagram that shows the different paths along which a star can evolve depending on its initial mass. The figure is adopted from Iben (1991). The various features shown here are the following. MS: main–sequence; RGB: red giant branch; RC: red clump; AGB: asymptotic giant branch; PN: planetary nebula.

troscopic observations of their red giant stars. Spectroscopic analyses can be done only in nearby early–type dwarf galaxies, due to the fact that their red giant stars become too faint for spectroscopic observations. Therefore, in more distant early–type dwarf galaxies one has to rely on their photometric properties in order to obtain information about their evolutionary histories. One important feature in the CMD that can be resolved in more distant dwarf galaxies is the red giant branch. The stars in the red giant branch phase of early–type dwarf galaxies are assumed to belong to an old population. Given this assumption, one can derive photometric metal abundances for these stars, and compare their metallicity properties to the ones of the Local Group dwarf galaxies in order to explore the impact of the environment in shaping these properties. This is done in this thesis for the early–type dwarf galaxies of the M 81 group. A comparison of early–type dwarf galaxies' metallicities obtained through spectroscopic and photometric observations gives important information on the effect of the complex star formation histo-

ries of early–type dwarf galaxies on their photometrically derived metallicities. The higher the fraction of the intermediate–age stars present, the more discrepant are the metallicities based on spectroscopy and photometry. The information on the fraction of the intermediate–age stars is thus important and can be probed through the fraction of the luminous asymptotic giant branch stars, which belong to the thermally–pulsating asymptotic giant branch phase. This study is performed using Galactic dwarf galaxies.

1.3 Overview

The structure of this Thesis is the following. In Chapter 1, we use the Tully–Fisher relation in order to search for potential tidal dwarf galaxy candidates in the M 81 group of galaxies. In Chapter 3, we use the red giant branch stars of nine early–type dwarf galaxies in the M 81 group in order to derive their metallicity distribution functions and examine the presence of metallicity gradients. In Chapter 4, we examine the effect of the presence of intermediate–age stellar populations on deriving the photometric metallicities in five Galactic dwarf spheroidals that have complex star formation histories with different fractions of intermediate–age populations, thus testing the assumption of a single, old age isochrone in deriving photometric metallicities. In Chapter 5, we summarise and present future prospects coming out of this work.

Chapter 2

Tidal Dwarf Galaxies in the M 81 Group

2.1 Introduction

Tidal dwarf galaxies are defined to be gravitationally bound systems that form during the gravitational interactions, collisions or mergers of massive spiral galaxies (Bournaud 2010; and references therein). They are formed out of the material expelled from their parent disk galaxies (Bournaud et al. 2007; and references therein). Within the framework of Cold Dark Matter theories, dark matter forms a spheroidal halo around galaxies and simulations show that material from the dark matter halo can not participate to the formation of tidal dwarf galaxies, since during their formation only material from rotating disks is involved (Bournaud et al. 2007; Bournaud 2010; and references therein). These rotating disks are assumed to be free of dark matter, unless there exists a disk of cold dark matter around the stellar disk (Bournaud 2010; see also Courteau & Rix 1999). Therefore, due to their formation mechanism, tidal dwarf galaxies are expected to be nearly dark matter free. This property is independent of their formation epoch and thus kinematic studies offer the best means to identify tidal dwarf galaxy candidates. Additionally, since tidal dwarf galaxies form from the recycled material of their parent galaxy, their metallicities are expected to be comparable with the one of their parent galaxy. In the case of a recent interaction, with the interaction signatures still detectable, young tidal dwarf galaxies have higher metallicities for their luminosity (Duc & Mirabel 1998), due to the fact that they form from the enriched material of their parent galaxy. In the case of an old tidal dwarf galaxy candidate, it is not an easy task to associate their metallicities with the ones of their parent galaxies, since their further star formation history shapes their chemical evolution. If the old population of a tidal dwarf galaxy originates from its parent galaxy, then the metallicity of this old population should be comparable to the metallicity of the old stellar population of the potential parent galaxy, though it is not straightforward to identify the parent galaxy once the signatures of the interaction become non–traceable.

In a recent study, Hunter, Hunsberger & Roye (2000) use the Tully–Fisher relation, the luminosity–metallicity relation, the structure, and the stellar populations of a sample of dwarf irregular galaxies, in order to identify potential tidal dwarf galaxies within their sample. The Tully–Fisher relation is examined on the basis that tidal dwarf galaxies are expected to be dark matter free, therefore they would deviate from the Tully–Fisher relation in the sense that they would have a too small maximum rotational velocity (or H I line width) for their luminosity (or baryonic mass). In the luminosity–metallicity relation, tidal dwarf galaxies, associated with interactions that have still traceable signs, should deviate from it in the sense that they would have too high metal abundances for their luminosity, since they are formed from the enriched material expelled from their parent galaxy. Their distinguishing properties based on their structure are discussed in Hunter, Hunsberger & Roye (2000) based on the expectation that tidal dwarf galaxies would not necessarily form as a disk galaxy, and thus may have different structure from other dwarf galaxies. Finally, tidal dwarf galaxies may inherit an old population that originates from their parent galaxy and then may undergo a strong burst of star formation at their formation epoch. This old population can reach up to a fraction of 40% (Elmegreen, Kaufman & Thomasson 1993). Therefore, studying the resolved stellar populations of potential young tidal dwarf galaxies can provide valuable information on their star formation history and put constraints on the epoch of their formation.

Motivated by the study of Hunter, Hunsberger & Roye (2000), we examine the Tully–Fisher relation as a way to search for potential tidal dwarf galaxies in the M81 group. The M 81 group of galaxies is the nearest interacting group and provides a promising environment to search for potential tidal dwarf galaxies. Two likely tidal dwarf galaxies candidates have been previously identified in the M 81 group: Garland and Ho IX. Garland has high oxygen abundance which places it away from the luminosity–metallicity relation and which is comparable to the metallicity of the M 81 galaxy (Croxall et al. 2009). Ho IX has been identified as a potential tidal dwarf galaxy based on a study of its stellar populations by Makarova et al. (2002), and based on its oxygen abundance by Croxall et al. (2009). Other studies of potential tidal dwarf galaxies include Arp's Loop (Makarova et al. 2002; De Mello et al. 2008; from its stellar population analysis), DDO 165 (Hunter, Hunsberger & Roye 2000; from its deviation from the Tully–Fisher relation) and KDG 52 (Hunter, Hunsberger & Roye 2000; Bureau & Carignan 2002; Bureau et al. 2004; from its deviation from the Tully–Fisher relation and its H I morphology).

The Tully–Fisher relation is the correlation between the luminosity and the H I line width of spiral galaxies and has been traditionally used as an extragalactic distance indicator independent of redshift (Tully & Fisher 1977; Sakai et al. 2000; Combes 2009; and references therein). It is an empirical correlation whose tightness, slope and zero point have been used to constrain models of galaxy formation (e.g. van den Bosch 2000; and references in Combes 2009). The slope and scatter of the Tully–Fisher relation depend on the wavelength used, where a better correlation is provided by the infrared Tully–

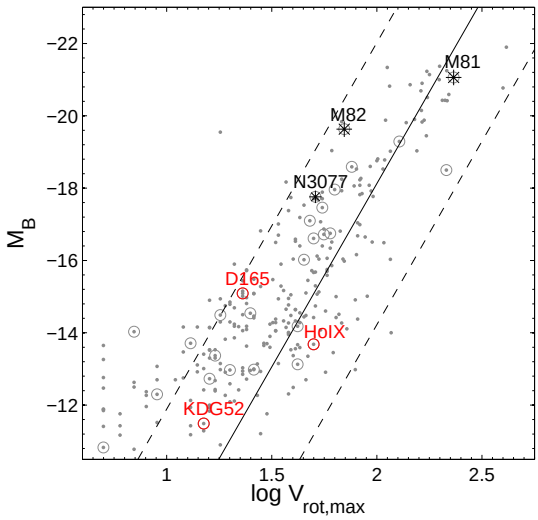

Figure 2.1: Absolute B–band magnitude, M_B, versus the maximum rotational velocity, $V_{rot,max}$ for the galaxies adopted in our sample. The galaxies of the M 81 group are indicated with the grey circles. The asterisks indicate the three interacting M 81 group galaxies, while the red circles indicate potential tidal dwarf galaxies in the M 81 group according to the studies of Hunter, Hunsberger & Roye (2000), Makarova et al. (2002), Sabbi et al. (2008), and Bureau et al. (2002, 2004). The solid line is adopted from Hunter, Hunsberger & Roye (2000), originally from the fit to the spirals of Broeils (1992), while the dashed lines are offsets from the solid line enough to encompass the bulk of the scatter, again adopted from Hunter, Hunsberger & Roye (2000).

Fisher relation (Aaronson, Huchra & Mould 1979). There is a break observed in the Tully–Fisher relation towards fainter magnitudes, where the gas–rich dwarf galaxies fall bellow the relation defined by brighter spirals (Matthews, van Driel & Gallagher 1998). This break towards the fainter magnitudes is reconciled once one uses the total baryonic mass, that is the total mass in stars, gas and dust, instead of the luminosity (McGaugh et al. 2000). Sakai et al. (2000) use the Tully–Fisher relation in order to derive the value of the Hubble constant. They discuss the systematic uncertainties entering the calibration of the Tully–Fisher relation.

2.2 Sample

We adopt a sub–sample of galaxies from the Catalogue of Neighbouring Galaxies (Karachentsev et al. 2004). The Catalogue of Neighbouring Galaxies includes 451 nearby galaxies within the Local Volume that have distances up to approximately 10 Mpc or radial velocities of $V_{LG} < 550$ km / sec. This catalogue provides the optical and H I properties of these galaxies. The selected sub–sample for our study consists of 285 galaxies, which includes those galaxies that have their absolute B–band

magnitudes, rotational velocities, H I masses, and widths of the H I profile measured at the 50% peak of the H I flux (W_{50}) listed in the Catalogue of Neighbouring Galaxies, with Local Group member galaxies excluded. In this sub–sample, there are 28 galaxies that belong to the M 81 group of galaxies. We do not list here the properties of the 285 galaxies, since these are provided in Table 1 and Table 4 of Karachentsev et al. (2004). We note that uncertainties related to the absolute B–band magnitude and H I line widths are not listed in the Catalogue of Neighbouring Galaxies. There are not any dwarf spheroidals galaxies within our sub–sample, since these do not have an H I line width W_{50}.

In order to calibrate the B–band and baryonic Tully–Fisher relation, we use those galaxies in our adopted sub–sample that are in common with the calibrating galaxies of Sakai et al. (2000; their Table 2). The calibrating galaxies of Sakai et al. (2000) consist of 21 spiral galaxies and were chosen such that they have distances determined using Cepheids. An analysis of individual uncertainties and how they affect the calibration of the Tully–Fisher relation is given in Sakai et al. (2000). The common galaxies between our adopted sub–sample from the Catalogue of Neighbouring Galaxies and the calibrating galaxies of Sakai et al. (2000) amounts to 9 galaxies, which now include M 31 and M 33. Given this small number of galaxies, the calibration will yield results with the estimated slopes and zero points having a large standard deviation, as shown in Sakai et al. (2000).

2.3 Results and Discussion

We show in Fig. 2.1 the absolute B–band magnitude, M_B, versus the maximum rotational velocity, $V_{rot,max}$, for our adopted sample of galaxies, shown in grey dots. The three interacting core galaxies M 81, M 82 and NGC 3077 are shown in black asterisks, while in blue circles we indicate tidal dwarf galaxy candidates in the M 81 group. The tidal dwarf galaxy candidates are DDO 165 (Hunter, Hunsberger & Roye 2000), Holmberg IX (Makarova et al. 2002; Sabbi et al. 2008), and KDG 52 (Hunter, Hunsberger & Roye 2000; Bureau et al. 2002, 2004). We note that there are more potential tidal dwarf galaxies in the M 81 group. We include only the above mentioned three candidates since the properties required for this study are included in the Catalogue of Neighbouring Galaxies. We note that KDG 52 is indicated as a potential tidal dwarf galaxy candidate according to the studies of Hunter, Hunsberger & Roye (2000) and Bureau et al. (2002, 2004), while Begum et al. (2006) estimate that its dynamical mass suggests that this dwarf galaxy is dark–matter dominated and thus not a tidal dwarf galaxy candidate. In Fig. 2.1, as already noted by Hunter, Hunsberger & Roye (2000), there is a deviation of the galaxies with $M_B > -15$ mag from the Tully–Fisher relation, indicating that these galaxies have rotational velocities that are too small for their luminosity, which implies that these galaxies have too little dark matter, thus making them suitable tidal dwarf candidates. Since, though, their blue luminosity, which is primarily a tracer of the young and more luminous component, overestimates their luminous mass and

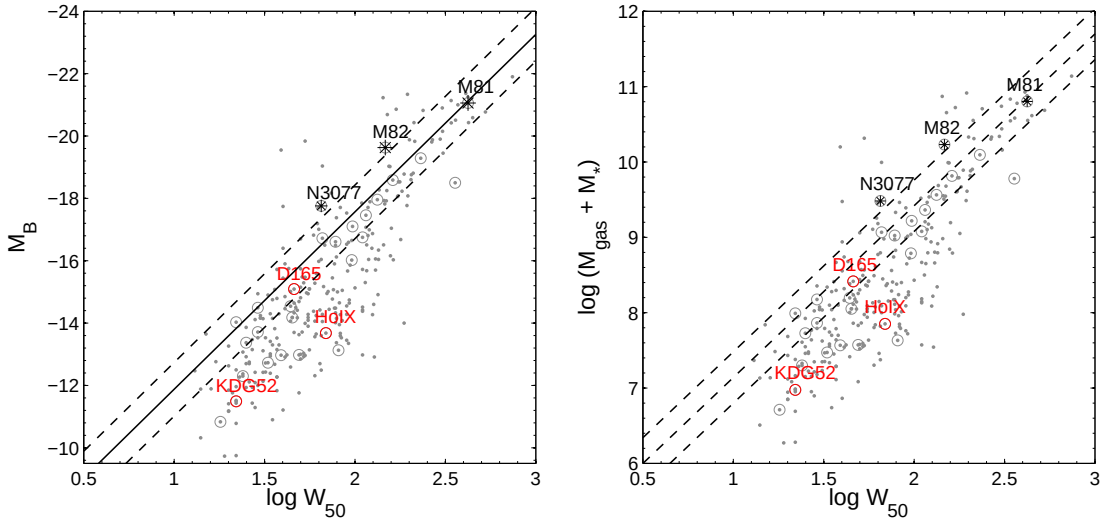

Figure 2.2: *Left:* B–band absolute magnitude versus W_{50}, the width of the logarithm of the H I profile measured at the 50% peak of the H I flux, for the galaxies adopted in our sample. The galaxies of the M 81 group are indicated with the grey circles. The asterisks indicate the three interacting core galaxies of the M 81 group. The red circles indicate potential tidal dwarf galaxies in the M 81 group. The solid line is a fit to the sub–sample spirals, as explained in the main text, while the dashed lines indicate the 1 σ scatter. *Right:* Baryonic Tully–Fisher relation. The symbols indicate the same objects as in the left figure. The solid line is a fit to the sample spirals that coincides with Sakai et al. (2000) calibrating sample, as explained in the text, while the dashed lines indicate the 1 σ scatter.

thus underestimates the total stellar mass, we later on explore the baryonic Tully–Fisher relation.

In the left panel of Fig. 2.2 we show the B–band Tully–Fisher relation for our adopted sample, shown in grey dots. The grey circled dots indicate the available M 81 group galaxies, while the asterisks denote the three core interacting member galaxies, namely M 81, M 82 and NGC 3077. The red circles correspond to the potential tidal dwarf galaxies described in the previous paragraph. The solid line corresponds to the fit of those spiral galaxies in the Catalogue of Neighbouring Galaxies which are in common with the sample of calibrating galaxies in Sakai et al. (2000; their Table 2), as described earlier. This common sample of galaxies corresponds to 9 galaxies and yields a slope of -5.69$\pm$0.34. In the B–band Tully–Fisher relation we note a break of the fainter galaxies from the relation. This deviation has been noted by Matthews, van Driel & Gallagher (1998) in their data who suggested that this is due to the fainter galaxies being highly dark–matter dominated. This deviation of the fainter galaxies from the Tully–Fisher relation should be reconciled if one uses the baryonic mass instead of the blue luminosity, since the dynamics of late–type galaxies may be dominated more by the gaseous component than the stellar components (Matthews, van Driel & Gallagher 1998; McGaugh, Schombert, Bothun & de Blok 2000). Finally we note that the maximum rotational velocity is computed from the

W_{50} through the relation: $V_{rot,max} = W_{50} / (2 \sin i)$, where i is the inclination angle (Karachentsev et al. 2004). Therefore, for constant W_{50} and increasing inclination angles, the $V_{rot,max}$ will decrease, which may explain the deviation to the right in Fig. 2.2 and the deviation to the left in Fig. 2.1.

In the right panel of Fig. 2.2 we show the baryonic Tully–Fisher relation for our adopted sample. The symbols are defined in the same way as in the B–band Tully–Fisher relation and are further explained in the caption of the figure. The baryonic mass is estimated from the stellar and H I mass for each galaxy in the following way. We calculate the mass in stars from the B–band magnitude, assuming that it is 1.54 times the B–band luminosity in solar units (Hunter, Hunsberger & Roye 2000). The mass in gas is assumed to be 1.34 times the mass in H I in order to take account for He. The mass in H I is computed for each galaxy using their H I gas density Σ_{HI} and the relation $\Sigma_{HI} = 4M_{HI}/\pi A_{25}^2$, where A_{25} is the major axis linear diameter (Karachentsev et al. 2004). The solid line corresponds to the fit of those galaxies that are in common between the Catalogue of Neighbouring Galaxies and the calibrating galaxies in Sakai et al. (2000; their Table 2). The slope of the baryonic Tully–Fisher relation is equal to 2.28$\pm$0.34, while the zero point is equal to 4.86$\pm$0.85. The dashed lines correspond to the 1 σ scatter due to the fit.

Even in the baryonic Tully–Fisher, there is a deviation of the fainter galaxies below the relation, indicating that these are dark matter dominated objects. The scope of this study is to identify potential tidal dwarf galaxies using the Tully–Fisher relation. Potential tidal dwarf galaxies should deviate from the Tully–Fisher relation in the sense that they should lie above it, something that is not observed. In addition, the potential tidal dwarf galaxies already identified in other studies, do not show the expected deviation above the Tully–Fisher relation, but instead are shown to be dark–matter dominated. According to the study of Croxall et al. (2009), DDO 165 has an oxygen abundance that follows the luminosity–metallicity relation defined by other members of the M 81 group, consistent with DDO 165 not being a young tidal dwarf galaxy. Ho IX lies in the core of the interaction, which may cause an overestimate of its H I line width. Makarova et al. (2002) and Sabbi et al. (2008) studied the stellar populations of Ho IX and found them consistent with Ho IX being a tidal dwarf galaxy, while Croxall et al. (2009) show that Ho IX has oxygen abundance comparable to the one of the M 81 galaxy. Finally, KDG 52 has a large dynamical mass as estimated by Begum et al. (2006), which makes it not a suitable tidal dwarf candidate.

2.4 Conclusions

Tidal dwarf galaxies are expected to be nearly free of dark matter content, due to their formation mechanism. This property is used in order to identify potential tidal dwarf galaxies using the B–band and baryonic Tully–Fisher relations. In the Tully–Fisher relation, it is expected that potential tidal dwarf

galaxies would lie above the relation defined by the larger spirals, exactly due to the property of tidal dwarf galaxies having little, if any, dark matter as compared to their luminosity or baryonic mass. Based on the Tully–Fisher relation, we do not identify dwarf galaxies in the M 81 group that lie above the relation defined by the larger spirals. Therefore we do not suggest the existence of potential tidal dwarf galaxy candidates in the M 81 group based on the Tully–Fisher relation.

Chapter 3

Dwarf Spheroidals in the M81 Group : Metallicity Distribution Functions and Population Gradients

3.1 Introduction

The dwarf galaxies within our Local Group have been the subject of intensive spectroscopic and photometric observations in different wavelength regimes and thus are well studied objects. Their study has been facilitated by the proximity of these dwarfs so that individual stars may even be resolved down to the main sequence turn-off, depending on their distance. Thus, extending the studies to dwarf galaxies in nearby groups with different environment and comparing their properties are of great importance in order to understand the main drivers of their evolution. In addition, the derived properties can provide a way to constrain models of galaxy formation as well as chemical evolutionary models

In this respect, the M 81 group is an interesting target: despite several differences, it bears close resemblance to our Local Group. The similarity of the M 81 group to our Local Group lies in its binary structure (Karachentsev et al. 2002), while its difference is mainly due to the recent interactions between its dominant constituents as revealed by the formation of tidal tails and bridges detected in HI observations (Appleton, Davies & Stephenson 1981; Yun, Ho & Lo 1994). With a mean distance of $\sim$3.7 Mpc (Karachentsev et al. 2002), the M 81 group is one of the nearest groups to our own Local Group. It consists of about 40 dwarfs of both early-type and late-type, with the addition of 12 recently discovered dwarf candidates (Chiboucas, Karachentsev & Tully 2009).

Here we focus on the dwarf spheroidal galaxies (dSphs) in the M 81 group with available Hubble

Space Telescope (HST) / Advanced Camera for Surveys (ACS) archival data. The dSphs are objects with low surface brightness and poor in gas content. For a summary of their properties we refer to Grebel, Gallagher & Harbeck (2003; and references therein). We use their color-magnitude diagrams (CMDs) to derive the photometric metallicity distribution functions (MDFs) and search for the potential presence of population gradients in the M 81 group dSphs.

The use of the CMD to infer the star formation histories and MDFs is a very powerful tool. For nearby groups at distances, where individual red giants are beyond the reach of spectroscopy even with 8-10 m class telescopes, CMDs are the best means to derive evolutionary histories. With the use of HST observations of adequate depth, the upper part of the red giant branch (RGB) can be resolved into single stars. Many studies have derived the photometric MDFs of distant Local Group dSphs (for example Cetus by Sarajedini et al. 2002; And VI and And VII by Grebel & Guhathakurta 1999) from their CMDs.

The search for radial population gradients in Local Group dwarf galaxies has been favoured by the fact that the resolved stellar populations reach the horizontal branch or extend even below the main-sequence turn-off depending on the distance of the dwarf, permitting one to use a variety of different stellar tracers. There are several studies for population gradients in the Local Group dwarfs and as an example of such studies we refer to the work done by Hurley–Keller, Mateo & Grebel (1999), Harbeck et al. (2001), Battaglia et al. (2006) (photometric) and Tolstoy et al. (2004), Koch et al. (2006) (spectroscopic).

This chapter is structured as follows. In §2 we present the observations, in §3 we show our results, in §4 we discuss our main findings and in §5 we present our conclusions.

3.2 Observations

We use HST / ACS archival data that were retrieved through the Multimission Archive at STScI (MAST). The details of the datasets used are listed in Table 3.1, where the columns show: (1) the galaxy name, (2) and (3) equatorial coordinates of the field centers (J2000.0), (4) the number of the Program ID and the PI, (5) the ACS / WFC filters used, and (6) the total exposure time for each filter.

The data reduction was carried out using Dolphot, a modified version of the HSTphot photometry package (Dolphin 2000) developed specifically for ACS point source photometry. The reduction steps followed are the ones described in the ACS module of the Dolphot manual. In the Dolphot output photometric catalogue, only objects with $S/N > 5$ and "type" equal to 1, which means "good stars", were allowed to enter the final photometric catalogue. The "type" is a Dolphot parameter that is used to distinguish objects that are classified as "good stars", "elongated objects", "too sharp objects"

Table 3.1: Log of Observations.

Galaxy	RA (J2 000.0)	Dec (J2 000.0)	Program ID / PI	ACS / WFC Filters	Exposure time (s)
(1)	(2)	(3)	(4)	(5)	(6)
KDG 61	09 57 03.10	+68 35 31.0	GO 9 884 / Armandroff	F606W / F814W	8 600 / 9 000
KDG 64	10 07 01.90	+67 49 39.0	...	...	...
DDO 71	10 05 06.40	+66 33 32.0	...	...	...
F12D1	09 50 10.50	+67 30 24.0	...	...	...
F6D1	09 45 10.00	+68 45 54.0	...	...	...
HS 117	10 21 25.20	+71 06 51.0	SNAP 9 771 / Karachentsev	F606W / F814W	1 200 / 900
IKN	10 08 05.90	+68 23 57.0	...	...	...
DDO 78	10 26 28.00	+67 39 35.0	GO 10 915 / Dalcanton	F475W / F814W	2 274 / 2 292
DDO 44	07 34 11.50	+66 52 47.0	...	...	2 361 / 2 430

Note.– Units of right ascension are hours, minutes, and seconds, and units of declination are degrees, arcminutes and arcseconds.

and so on. After this first selection, quality cuts were applied so as to further clean the photometric catalogue. These cuts were based on the distributions of the sharpness and crowding parameters, as suggested in the Dolphot manual and also in Williams et al. (2009). Guided by these distributions, we use for the sharpness parameter the restriction of $|sharpness_{filter} + sharpness_{F814W}| < \alpha$, where ($1.0 < \alpha < 1.5$) depending on the dSph, and for the crowding parameter the requirement ($Crowding_{filter} + Crowding_{F814W}$) < 1.0, where "filter" corresponds to either the F606W or the F475W filter. These selections were made so as to ensure that only stellar objects have entered our final photometric catalogue. The number of stars recovered after applying all the photometric selection criteria are listed in Table 3.2, column (3).

The photometry obtained with Dolphot provides magnitudes in both the ACS / WFC and the Landolt UBVRI photometric systems using the transformations provided by Sirianni et al. (2005) for the UBVRI system. In the analysis presented throughout this work, we chose to use the ACS / WFC filter system. Therefore, if we use data from the literature computed in the UBVRI photometric system, we transform them to the ACS / WFC system. There are two cases where this is necessary. The first case is the extinction. The galactic foreground extinction in the V-band and I-band, A_I and A_V, taken from Schlegel, Finkbeiner & Davis (1998) through NED, are transformed into the ACS / WFC system. For the transformation, we use the corresponding extinction ratios $A(P) \,/\, E(B-V)$ for a G2 star, where $A(P)$ corresponds to the extinctions in the filters F814W and F606W (or F475W), which are provided by Sirianni et al. (2005; their Table 14). We note that the assumption of a largely color-independent reddening for the RGB is justified since theoretical models indicate that the expected effect of the change of color across the RGB amounts to at most 0.01 in $E(V-I)$ for our data (see Grebel & Roberts 1995). We multiply these extinction ratios with the $E(B-V)$, in order to finally get the extinctions in the ACS filters. The transformed values, A_{F814W} and A_{F606W} (or A_{F475W}), are listed in Table 3.2, columns (6) and (7) respectively.

The second case is the I-band tip of the RGB (TRGB), which we transform to the F814W-band TRGB in the following way. As already mentioned, Dolphot provides the magnitudes both in the instrumental ACS / WFC system and in the transformed UBVRI. Thus, in the range of magnitudes near the I-band TRGB, we compute the difference in magnitudes between the I-band and F814W-band. This difference is 0.01 mag for all the dSphs except for DDO 44 and DDO 78, where the difference is -0.015 mag. The F814W-band TRGB is then equal to the sum of this difference and the I-band TRGB. We confirm further more this approach of estimating the F814W-band TRGB by applying a Sobel-filtering technique to the luminosity function of some of the dSphs (Lee, Freedman & Madore 1993; Sakai, Madore & Freedman 1996) estimating the location of the F814W-band TRGB. We find that these approaches give values that are in good agreement, with a mean difference between them of the order of 0.05 mag.

Table 3.2: Global Properties (see text for references).

Galaxy	Type	N_*	M_V (mag)	I_{TRGB} (mag)	A_{F814W} (mag)	A_{F606W}[a] (mag)	$(m-M)_O$ (mag)	R (kpc)	r_{eff} ($''$)
(1)	(2)	(3)	(4)	(5)	(6)	(7)	(8)	(9)	(10)
KDG 61	dIrr / dSph	53 543	-13.87	23.86 ± 0.15	0.131	0.202	27.78 ± 0.15	44	48
KDG 64	dIrr / dSph	38 012	-13.43	23.90 ± 0.15	0.099	0.152	27.84 ± 0.15	126	28
DDO 71	dIrr / dSph	37 291	-13.22	23.83 ± 0.15	0.173	0.267	27.72 ± 0.15	211	59
F12D1	dSph	39 519	-12.84	23.95 ± 0.15	0.263	0.404	27.71 ± 0.15	181	31
DDO 78	dSph	21 073	-12.83	23.85 ± 0.15	0.040	0.079	27.85 ± 0.15	223	38
DDO 44	dSph	19 357	-12.56	23.55 ± 0.15	0.075	0.149	27.52 ± 0.15	901	28
IKN	dSph	14 600	-11.51	23.94 ± 0.15	0.111	0.171	27.87 ± 0.18	110	...
F6D1	dSph	14 260	-11.46	23.77 ± 0.14	0.144	0.222	27.66 ± 0.17	218	32
HS 117	dIrr / dSph	4 596	-11.31	24.16 ± 0.15	0.210	0.323	27.99 ± 0.18	204	29

[a] or A_{F475W} in the case of DDO 44 and DDO 78

We list the global properties of the present dSph sample in Table 3.2. The columns contain the following information: (1) the galaxy name, (2) the galaxy type, (3) the number of stars detected after applying all the photometric selection criteria, (4) the visual absolute magnitude M_V of each galaxy adopted from Karachentsev et al. (2000, 2001), Alonso-Garcia, Mateo & Aparicio (2006), Georgiev et al. (2009), (5) the I-band TRGB adopted from Karachentsev et al. (2006, 2001, 2000, 1999), (6) and (7) the foreground extinction derived by us for the ACS / WFC filters F814W, F606W and F475W, as described in Sec. 2, (8) the true distance moduli adopted from Karachentsev et al. (2006, 2001, 2000, 1999), (9) the deprojected distance of the dSphs from the M 81 galaxy, R, adopted from Karachentsev et al. (2002), (10) the effective radius, r_{eff} adopted from Sharina et al. (2008) and Karachentseva et al. (1987). The dSphs in Table 3.2 are sorted according to their M_V value.

Finally, the pixel scale of the ACS / WFC is 0.05″ with a field of view of 202″ × 202″ or 4 096 × 4 096 pixels. Thus for the mean distance of ∼3.7 Mpc of the M 81 group (Karachentsev et al. 2002) this field of view corresponds to 3.6 kpc × 3.6 kpc, or simply 1 pixel corresponds to roughly 1 pc.

3.3 Results

3.3.1 Color–magnitude diagrams

We show the CMDs of the nine dSphs in Fig. 3.1, where we note the difference in the x-axis. The proximity of the M 81 group and the depth of the observations allow us to resolve the upper part of the RGB into individual stars. The most prominent feature seen in our CMDs is the RGB. We note the presence of stars above the TRGB, which is indicated in Fig. 3.1 with a dashed line. These stars are most likely luminous AGB stars, which indicate the presence of stellar populations in an age range from 1 Gyr up to less than 10 Gyr. In addition, some of the dSphs appear to have bluer stars that probably belong to a younger main sequence. The dwarfs in our sample are classified as dSphs (Karachentsev et al. 2004), with the exception of KDG 61, KDG 64, DDO 71, and HS 117 which are classified as transition-types (dIrr / dSph) as they have detectable HI content (Huchtmeier & Skillman 1998; Boyce et al. 2001) or $H\alpha$ emission (Karachentsev & Kaisin 2007; Karachentsev et al. 2006).

3.3.2 Photometric metallicity distribution functions

We show the photometric MDFs for the nine dSphs in Fig. 3.2. These are constructed using linear interpolation between Dartmouth isochrones (Dotter et al. 2008) with a fixed age of 12.5 Gyr. We use Dartmouth isochrones, since they give the best simultaneous fit to the full stellar distribution of a simple stellar population within a CMD as demonstrated by e.g. Glatt et al. (2008a, 2008b) for star clusters.

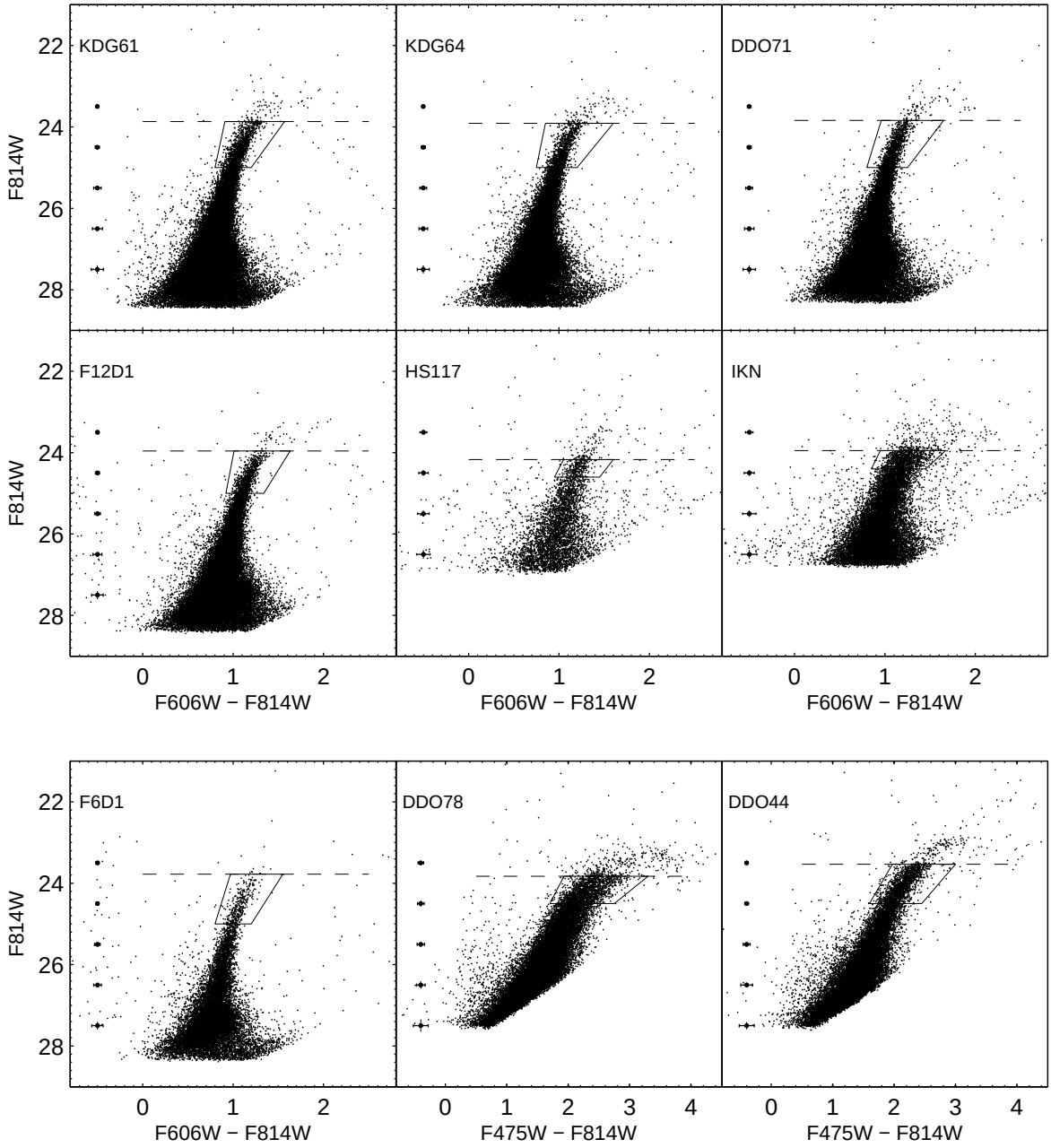

Figure 3.1: Color-magnitude diagrams for the nine dSphs. The horizontal dashed lines show the location of the TRGB. The crosses on the left hand side correspond to the photometric errors as derived from artificial star tests. The boxes enclose the stars for which we derive the photometric metallicities.

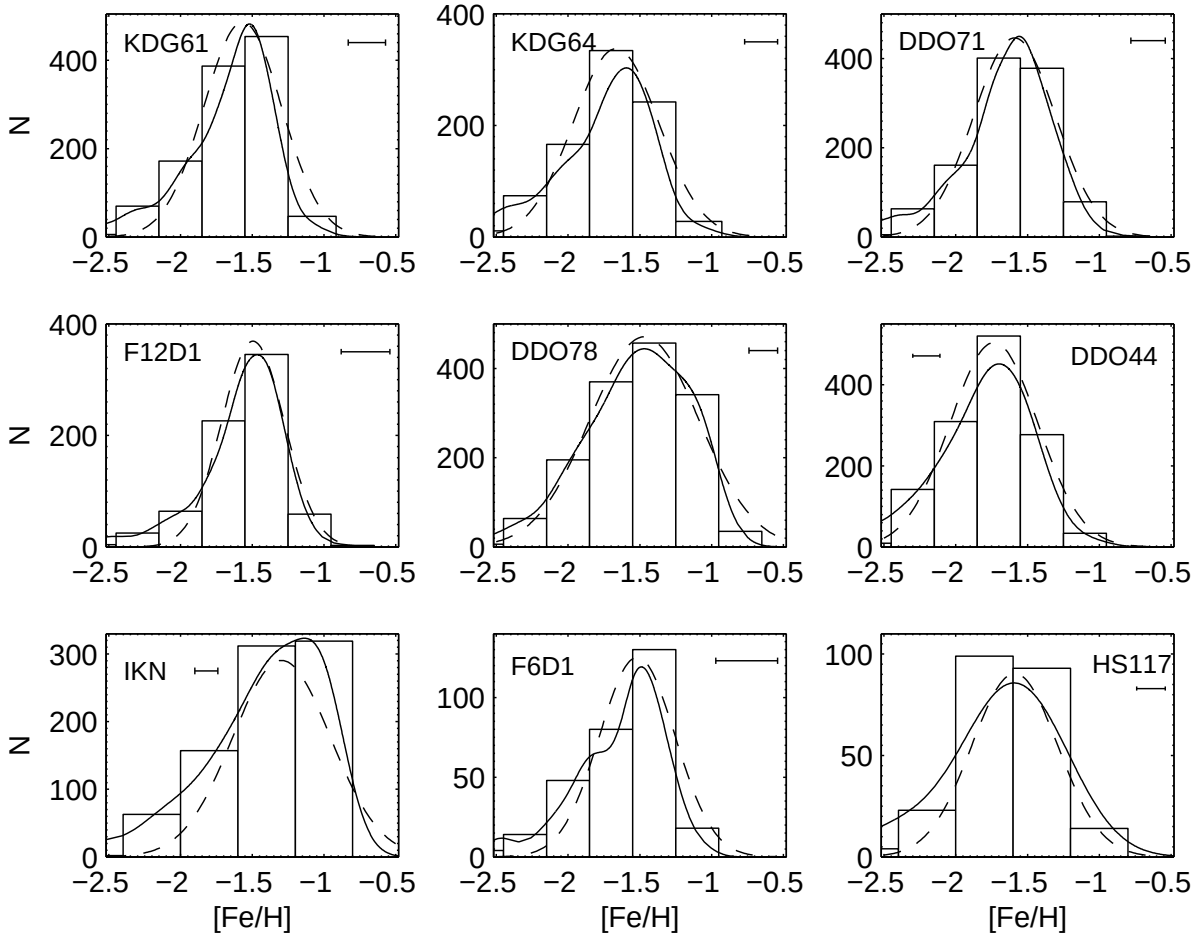

Figure 3.2: Metallicity distribution functions for the nine dSphs sorted by their absolute M_V magnitude, from top to bottom and from left to right. The solid lines show the metallicity distribution convolved with the errors in metallicity. The dashed lines show the fitted gaussian distributions. The error bars in the upper right corner, or upper left in the case of DDO 44, show the 1 σ spread for the weighted mean metallicity we derive from our data. Note the different scaling of the individual y-axes.

We chose the fixed age of 12.5 Gyr since the RGB in these dSphs may be assumed to consist of mainly old stars in an age range of about 10 Gyr to 13 Gyr. The assumption of an old isochrone is also justified by the comparatively small number of luminous AGB stars above the TRGB.

The choice of 12.5 Gyr is an assumption we are making in order to estimate the MDFs for each dwarf, while the choice of another age in the above range would not considerably affect our results, as is shown later on in this section. Indeed, the colors of the stars on the RGB are mostly affected by metallicity differences rather than age differences (see for example Caldwell et al. 1998; Harris, Harris & Poole 1999 (their Fig. 6); Frayn & Gilmore 2002 (their Fig. 2)). Thus the observed spread in the

RGB color is likely caused by a metallicity spread rather than an age spread, justifying our choice of an constant age isochrone.

The isochrone metallicities we used range from -2.50 dex to -0.50 dex with a step of 0.05 dex. The isochrone step we used is chosen such that it is smaller than the photometric errors. Representative photometric error bars are indicated with crosses in Fig. 3.1. To account for the influence of crowding and the photometric quality, we conducted artificial star tests. For that purpose, we used the utilities provided and as described in Dolphot. More specifically, we generate an artificial star list of approximately 10^5 stars for each of the two ACS chips. The artificial stars are randomly distributed across the field of view. We run the photometry using the same parameters as in the case of the true stellar photometry. We apply the same photometric quality cuts in the final artificial stellar catalogue as in the true photometric catalogue.

Given the lack of any spectroscopic information, this method of deriving the MDFs is in general fairly accurate as discussed in Frayn & Gilmore (2002). In practise, we interpolate between the two closest isochrones bracketing the color of a star, in order to find the metallicity of that star.

We only select stars within a box plausibly containing stars on the upper RGB to construct the galaxies' MDF. The bright magnitude limit of the box is chosen to exclude the stars brighter than the TRGB which belong mainly to the luminous AGB phase. The faint magnitude limit of the box is chosen to fulfil the requirement that the formal error in the derived [Fe/H] is less than 0.15 dex, or 0.2 dex in the case of IKN and HS 117 when the photometric errors are taken into account. We employ a different selection criterion in the case of IKN and HS 117 in order to have a significant number of stars in their sample as compared to the one of the remaining dSphs. The selection criterion based on the metallicity formal error depends on the depth of the observations. In our data sample we distinguish three categories, from now on referred to as depth categories. The first depth category contains KDG 61, KDG 64, DDO 71, F6D1 and F12D1. The second depth category contains DDO 44 and DDO 78. The third depth category contains IKN and HS 117. Each depth category contains those dSphs that belong to the same Program ID and thus have the same filters and roughly the same exposure times, as listed in Table 3.1.

In order to estimate the faint magnitude limit for each dSph's RGB box as a function of the error in [Fe/H], we proceed as follows. We extend the faint limit of the bounding box to a magnitude limit of 26 in F814W for all the dSphs. We compute the [Fe/H] for all the stars within each dSph's box, as well as the corresponding errors in metallicity. We show the derived mean errors in metallicity versus the F814W-band magnitude in Fig. 3.3 for KDG 61, DDO 44, IKN and HS 117, which are chosen here as representative examples of the three depth categories. In the case of IKN and HS 117, which belong to the third depth category, we show the corresponding plots for both since the requirement of 0.20 dex leads to slightly different faint limits of the RGB box. Based on these plots and on the metallicity

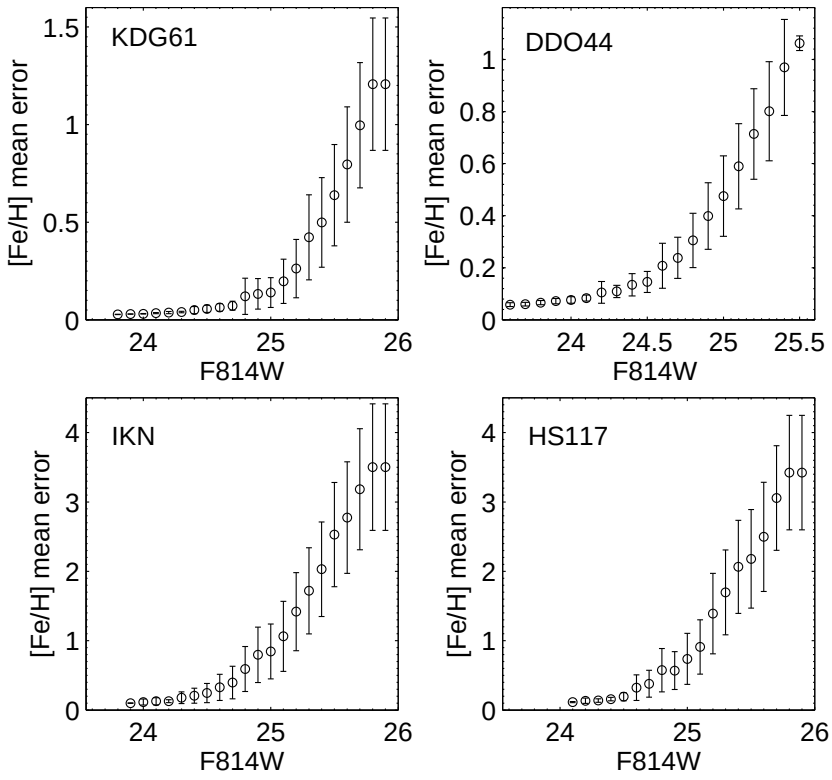

Figure 3.3: Mean error in metallicity versus the F814W-band magnitude. The circles indicate the mean error in metallicity in each magnitude bin, while the error bars indicate the standard deviation of the errors.

requirements, we choose 25 and 24.5 mag as faint limit for the first and second depth category, while in the case of IKN and HS 117 we choose 24.4 and 24.6 mag, respectively. The choice of these limits corresponds to an error in color of less than 0.02 mag for the first depth category and less than 0.07 mag for the remaining two depth categories. We note that the difference in the error in color is due to the different exposure times for each dSph data set, which are listed in the column (6) of Table 3.1. The RGB boxes used in each dSph are drawn in Fig. 3.1.

The distribution of the photometric errors as a function of the F 814 W–band magnitude are shown in Fig. 3.4. The photometric errors shown for the F 814 W–band magnitude range are greater than the ones used to derive the MDFs. Within the ranges defined from the RGB boxes, the photometric errors are less than approximately 0.02 mag for KDG 61, and 0.05 mag for DDO 44 and IKN. The photometric errors depend on the depth of the observations.

The M 81 group lies at a Galactic latitude of approximately 40 °, where the foreground contamination is not significant. At the Galactic latitude of the M 81 galaxy, the expected foreground contamina-

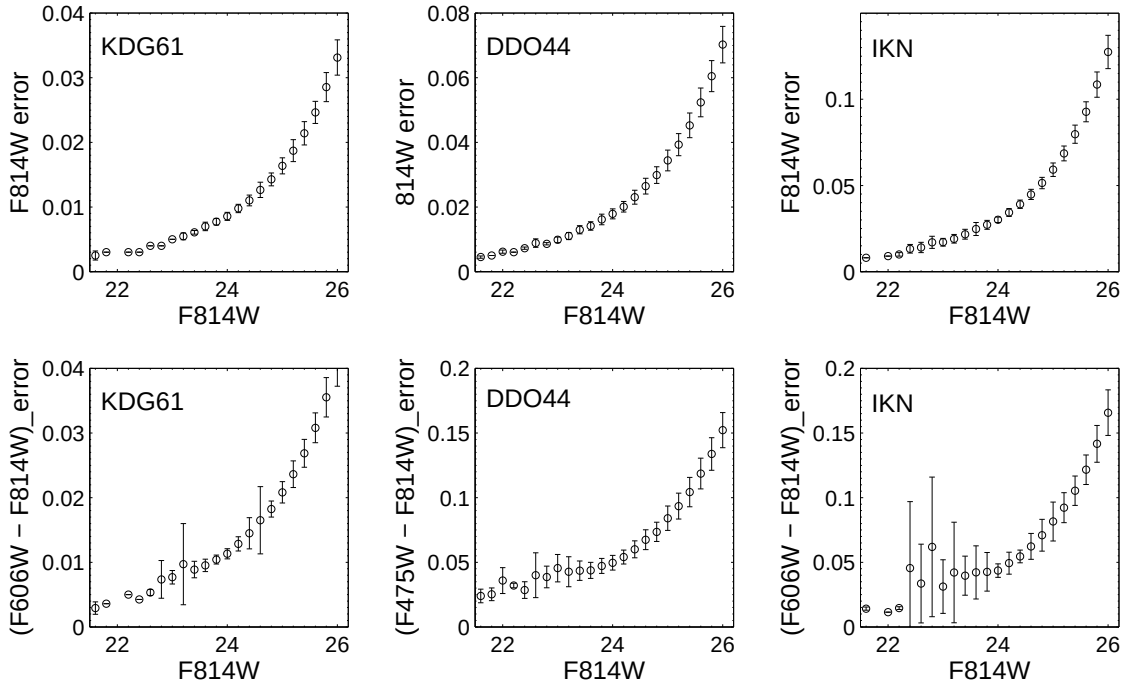

Figure 3.4: Mean photometric errors as a function of the F 814 W–band magnitude for the three depth categories with KDG 61, DDO 44 and IKN as representative examples. The circles indicate the mean error in each magnitude bin, while the error bars indicate the standard deviation of the errors. The upper panels show the F 814 W–band errors as a function of the F 814 W–band magnitude, while the lower panels show the color errors as a function of the F 814 W–band magnitude.

tion is less than 20 stars per arcmin^2 (Williams et al. 2009). For the studied dSphs here, we estimate later on a very low foreground contamination based on the location of the luminous AGB stars in the CMD, of the order of less than approximately 1%. In the case of IKN, foreground stars make it difficult to recover the structural properties of this dSph. In the case of KDG 64, there is a background galaxy sitting in the center of the dwarf.

In Fig. 3.5, left panel, we plot the RGB box used in the case of the dwarf KDG 64 as well as a subset of the isochrones used for the interpolation method, here ranging from -2.50 dex to -0.80 dex. The step remains 0.05 dex. The grid of the theoretical isochrones we use is fine enough that the spacing between them is kept nearly vertical. We correct the magnitudes and colors of the theoretical isochrones for foreground Galactic extinction and for the distance modulus of each dSph. The A_{F814W} and A_{F606W} (or A_{F475W} in the case of DDO 44 and DDO 78) that we calculate and the true distance moduli are listed in Table 3.2, columns (6) and (7) for the extinction and (8) for the distance moduli. The I-band TRGB values shown in column (5) of the same table were used to compute the F814W-band TRGB values, as explained already in Sec. 3. 2.

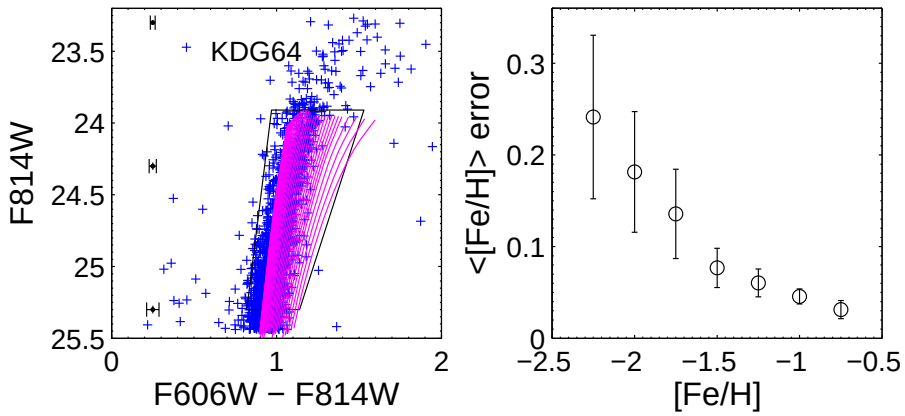

Figure 3.5: *Left panel*: Color-magnitude diagram for KDG 64 zoomed in the RGB part to show the stars selected in the box, shown with the black solid line, for which we compute their photometric metallicities. In the same figure we overplot with solid magenta lines a subset of the isochrones used for the interpolation method, with metallicities ranging from -2.50 dex to -0.80 dex. The black crosses towards the left side correspond to the photometric errors as derived from artificial star tests. *Right panel*: The error in metallicity versus the [Fe/H] as derived with the use of Monte Carlo simulations. The circles indicate the mean metallicity in each metallicity bin, while the error bars indicate the standard deviation of the mean.

We note in Fig. 3.5 the presence of stars within the RGB box bluewards of the most metal-poor isochrone available from the Dartmouth set of isochrones. These stars are not used to construct the MDF. The existence of such stars may indicate the presence of more metal-poor RGB stars or of old AGB stars, with ages typically greater or equal to 10 Gyr. Such old AGB stars that have the same luminosity as RGB stars were also noted, for example, by Harris, Harris & Poole (1999) while constructing the MDF for stars in a halo field of the giant elliptical NGC 5128. It is expected that at most 22 % of the stars in the RGB selection box, and within 1 mag below the TRGB, are actually old AGB stars (Durrell, Harris & Pritchet 2001; Martinez-Delgado & Aparicio 1997; and references therein). In order to quantify the effect of the presence of such stars, we construct the MDF of KDG 61 using Padova isochrones (Girardi et al. 2008; Marigo et al. 2008), which also include the AGB phase. We run the interpolation code once using isochrones that only include the RGB phase and once with isochrones that only include the AGB phase, for a constant age of 12.5 Gyr and a range in metallicities from [Fe/H] $=$ -2.36 dex (or Z $=0.0001$) to [Fe/H] $=$ -0.54 dex (or Z $=0.006$), with a step of 0.1 dex in [Fe/H]. The derived mean values differ only by 0.04 dex in [Fe/H] with a mean of $\langle$[Fe/H]$\rangle$ $=$ -1.24 dex for the MDF constructed using isochrones that include only the RGB phase. The MDF of the stars that were fit using isochrones that include only the AGB phase becomes more metal-rich. Furthermore, the derived 1 σ spreads in [Fe/H] have comparable values of 0.26 dex when we include only the RGB phase and of 0.27 dex when we include only the AGB phase. In addition, if we randomly assign 22 % of the stars

Table 3.3: Derived Properties.

Galaxy	$\langle$[Fe/H]$\rangle \pm \sigma$ (dex)	$\langle$[Fe/H]$\rangle_w \pm \sigma$ (dex)	$K-S^a$ (%)	f_{AGB}
(1)	(2)	(3)	(4)	(5)
KDG 61	-1.65 ± 0.28	-1.49 ± 0.26	16	0.07
KDG 64	-1.72 ± 0.30	-1.57 ± 0.23	12	0.09
DDO 71	-1.64 ± 0.29	-1.56 ± 0.24	0	0.09
F12D1	-1.56 ± 0.27	-1.43 ± 0.34	8	0.07
DDO 78	-1.51 ± 0.35	-1.36 ± 0.20	0	0.09
DDO 44	-1.77 ± 0.29	-1.67 ± 0.19	0	0.11
IKN	-1.38 ± 0.37	-1.08 ± 0.16	...	0.08
F6D1	-1.63 ± 0.30	-1.48 ± 0.43	0.036	0.03
HS 117	-1.65 ± 0.32	-1.41 ± 0.20	55	0.14

[a]The probabilities indicate whether the populations under consideration are from the same distribution.

within the RGB box with metallicities as derived using only the AGB phase, while the remaining 78 % of the stars with metallicities as derived using only the RGB phase, then the resulting MDF has a mean of $\langle$[Fe/H]$\rangle = -1.24$ dex with 1 σ spread in [Fe/H] of 0.29 dex. This mean metallicity is comparable to the one we compute when we use only the RGB phase to derive the metallicities. The shape of the MDFs in all these cases does not change significantly. Thus, we can safely conclude that the presence of these contaminating old AGB stars within the RGB box does not affect the derived MDFs' properties significantly.

In Fig. 3.2 we overplot the metallicity distribution convolved with the errors in metallicity (solid line). Also shown in Fig. 3.2 (dashed lines) are fits of Gaussian distributions with the observed mean and dispersion. For each dSph we compute the mean metallicity, $\langle$[Fe/H]$\rangle$, as well as the error-weighted mean metallicity, $\langle$[Fe/H]$\rangle_w$, along with the corresponding intrinsic 1 σ dispersions. We show them in Table 3.3, columns (2) and (3), while the error bars in Fig. 3.2 indicate the 1 σ dispersion of the error-weighted mean metallicities. The errors in metallicity are computed from a set of Monte Carlo simulations, in which each star is varied by its photometric uncertainties (both in color and magnitude, as given by the Dolphot output) and re-fit using the identical isochrone interpolation as described above. The 1 σ scatter of the output random realisations was then adopted as the metallicity error for each star. In the right panel of Fig. 3.5 we show the errors in metallicity computed as described above versus the metallicities derived for all the stars within the RGB box, here for KDG 64 as an example. The error in metallicity increases towards the metal-poor part, which is due to the spacing between the isochrones that becomes narrower towards the metal-poor part.

In order to further quantify the effect of the assumption of the constant age on the MDFs, we apply again the same analysis using two different constant ages for the isochrones in the interpolation method.

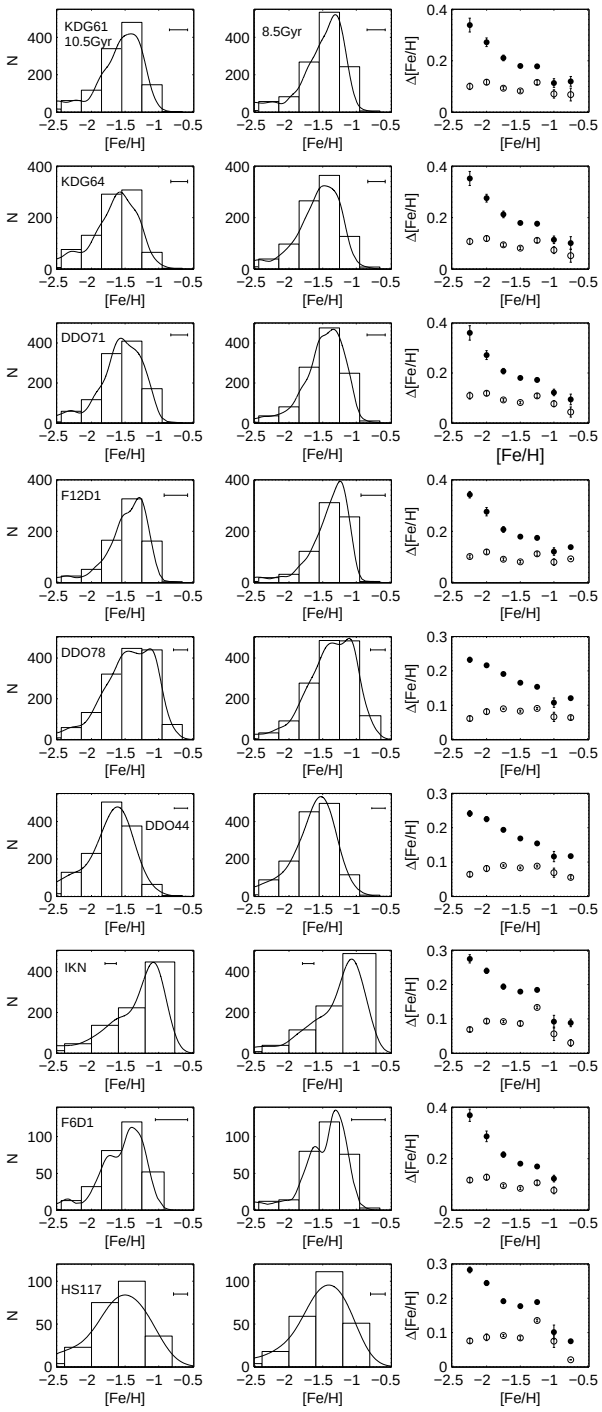

Figure 3.6: Metallicity distribution functions for the nine dSphs computed in the same way using isochrones with two different ages: *left panels* for a constant age of 10.5 Gyr and *middle panels* for a constant age of 8.5 Gyr. The solid lines show the metallicity distribution convolved with the errors in metallicity. The error bars correspond to the 1 σ spread for the weighted mean metallicity we derive from our data. *Right panels:* Star-by-star difference of the derived metallicities, Δ[Fe/H], using the 10.5 Gyr isochrones minus the 12.5 Gyr isochrones versus the [Fe/H] of the 10.5 Gyr isochrones, indicated with the open circles. The star-by-star differences of the 8.5 Gyr isochrones minus the 12.5 Gyr isochrones are indicated with the dots.

Table 3.4: Error-weighted mean metallicities for the 10.5 Gyr and 8.5 Gyr isochrones MDFs.

Galaxy	$\langle$[Fe/H]$\rangle_{w,10.5} \pm \sigma$ (dex)	$\langle$[Fe/H]$\rangle_{w,8.5} \pm \sigma$ (dex)
(1)	(2)	(3)
KDG 61	-1.37 ± 0.27	-1.32 ± 0.27
KDG 64	-1.45 ± 0.25	-1.39 ± 0.26
DDO 71	-1.41 ± 0.25	-1.34 ± 0.27
F12D1	-1.31 ± 0.35	-1.25 ± 0.36
DDO 78	-1.28 ± 0.21	-1.24 ± 0.22
DDO 44	-1.60 ± 0.20	-1.53 ± 0.20
IKN	-1.03 ± 0.17	-0.98 ± 0.17
F6D1	-1.37 ± 0.48	-1.31 ± 0.50
HS 117	-1.31 ± 0.21	-1.27 ± 0.22

The first constant age for the isochrones is 10.5 Gyr, while the second constant age is 8.5 Gyr. We repeat the isochrone interpolation with the bounding boxes and the metallicity ranges being kept the same in all cases. We show the results for the MDFs of all the dSphs in Fig. 3.6, where the MDFs for the 10.5 Gyr isochrones are shown in the left panels and the ones for the 8.5 Gyr isochrones in the middle panels. The derived error-weighted mean metallicities $\langle$[Fe/H]$\rangle_{w,10.5}$ and $\langle$[Fe/H]$\rangle_{w,8.5}$, for the 10.5 Gyr and 8.5 Gyr isochrones, respectively, are shown in Table 3.4, along with their corresponding dispersions.

In addition, the star-by-star difference in [Fe/H] as derived using the 10.5 Gyr and 8.5 Gyr isochrones is shown in Fig. 3.6, right panels. The maximum difference in the derived [Fe/H] using the 10.5 Gyr isochrones minus the isochrones with a constant age of 12.5 Gyr is less than 0.20 dex in all the cases, while the maximum difference in the derived [Fe/H] using the 8.5 Gyr isochrones minus the isochrones with a constant age of 12.5 Gyr is less than 0.40 dex in all the cases. Finally, the overall shape of the MDFs as derived for the 10.5 Gyr and the 8.5 Gyr isochrones does not change significantly.

3.3.3 Population gradients

Population or metallicity gradients provide important information for the chemical enrichment and star formation history of dwarf galaxies. According to Marcolini et al. (2008), supernovae of type II, SNe II, and of type I, SNe Ia, can explain the presence of a metallicity gradient in a dSph with an initial star formation that extends to 3 Gyr. SNe II are produced from massive stars, therefore the SNe II progenitors explode within approximately 10^7 yr after a burst of star formation. SNe II drive the metals outwards and lead to a homogenisation of the metallicity within a dSph. Therefore, in the case of star formation that produces SNe II progenitors, there is mild, or not any, metallicity gradient detectable. SNe Ia are produced from low or intermediate mass stars, and therefore their progenitors require more

time until they explode as SNe Ia. The effect of SNe Ia is to produce iron–rich inhomogeneities ("SNe Ia pockets"), which are preferentially concentrated within 2 core radii of the dSph (Marcolini et al. 2008). Therefore, any subsequent star formation occurring in the vicinity of the SNe Ia pockets would produce iron–rich stars, preferentially concentrated within 2 core radii. This would account for the presence of a [Fe/H] gradient (Marcolini et al. 2008).

In order to examine the presence or absence of population gradients in our dSph sample, we construct the cumulative histograms of the stars in each dSph selected in two metallicity ranges, defined as above and below the respective $\langle$[Fe/H]$\rangle_w$. Since the dSphs can be considered as being elliptical in projection to first order, we define in the following the elliptical radius r as

$$r = \sqrt{x^2 + \frac{y^2}{(1-\epsilon)^2}}, \tag{3.1}$$

where x and y are the distance along the major and minor axis, and ϵ is the ellipticity. The major and minor axes are computed by fitting an ellipse to contours of the number counts of all stars above the 1 σ level. This ellipse is shown in white in Fig. 3.7 and represents the elliptical shape that was chosen for each dSph. In the same Fig. 3.7 we show the contours above the 0.5 σ to 2 σ level, which are overlaid on top of density maps. In the study of population gradients we exclude the IKN dSph since the field of view does not cover the whole extent of the galaxy and furthermore is contaminated by a bright foreground star. In addition, we do not show the elliptical shape for IKN.

We show the cumulative metallicity distributions in Fig. 3.8 and Fig. 3.9 (middle panels). We show in the same figures the radial metallicity distributions (upper panels) and the mean radial metallicity profiles (lower panels). Each radial metallicity profile shows the mean values of metallicity within an elliptical annulus versus the elliptical annulus in units of the effective radius r_{eff}. The values for r_{eff} are listed in the column (10) of Table 3.2. The error bars in the metallicity profile correspond to the standard deviation of the mean metallicity in each elliptical radius annulus.

3.3.4 Density maps of populations of different metallicities

We now examine the spatial distribution of the stellar populations, separated into a metal-poor and metal-rich component. For that purpose, we define two stellar populations, the first includes stars having a metallicity less than or equal to the value of -1.80 dex ("metal-poor"), while the second includes stars with a metallicity larger than or equal to -1.30 dex ("metal-rich"). These metallicity ranges are chosen as such by definition, while guided by the mean metallicities of Local Group dwarf galaxies. Local Group dSphs show a wide range of mean stellar metallicities ranging from -2 dex for Draco, an old population dominated dSph, to -1.2 dex for Fornax, a dSph with extended star formation and

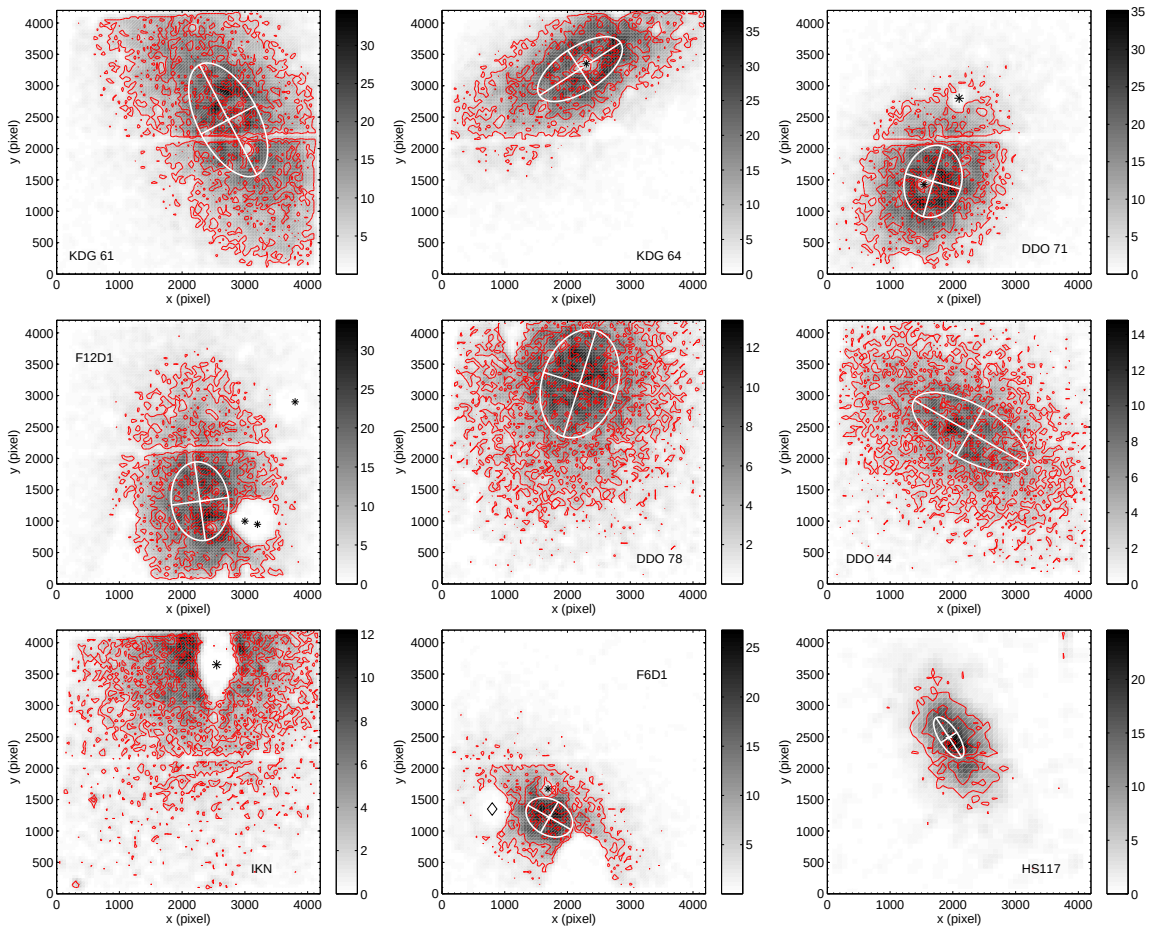

Figure 3.7: Contour plots, shown in red, for the nine dSphs which are overlaid on top of density maps. The elliptical shape chosen for each dSph, with the exception of IKN, is shown with the white ellipse. The star symbols in some plots correspond to bright foreground stars, while in the case of KDG 64 corresponds to a background galaxy. The diamond symbol in the case of F6D1 corresponds to an extended background galaxy. The unit of the colorbars is number of stars per $(50 \text{ pixels})^2$.

chemical evolution history (Grebel, Gallagher & Harbeck 2003). These ranges of the observed stellar metallicities of the Local Group dSphs have influenced our defined limits for the metal–poor and metal–rich populations. All galaxies have peak values that lie well in between those cuts so that the metal-poor and the metal-rich tails are representatively sampled for all dSphs. For these two populations we construct the gaussian-smoothed density maps, shown in Fig. 3.10 and Fig. 3.11, upper and middle panels for each dSph. The spatial distribution of stellar populations selected according to their metallicity provides an additional way to look for variations of metallicity with spatial location.

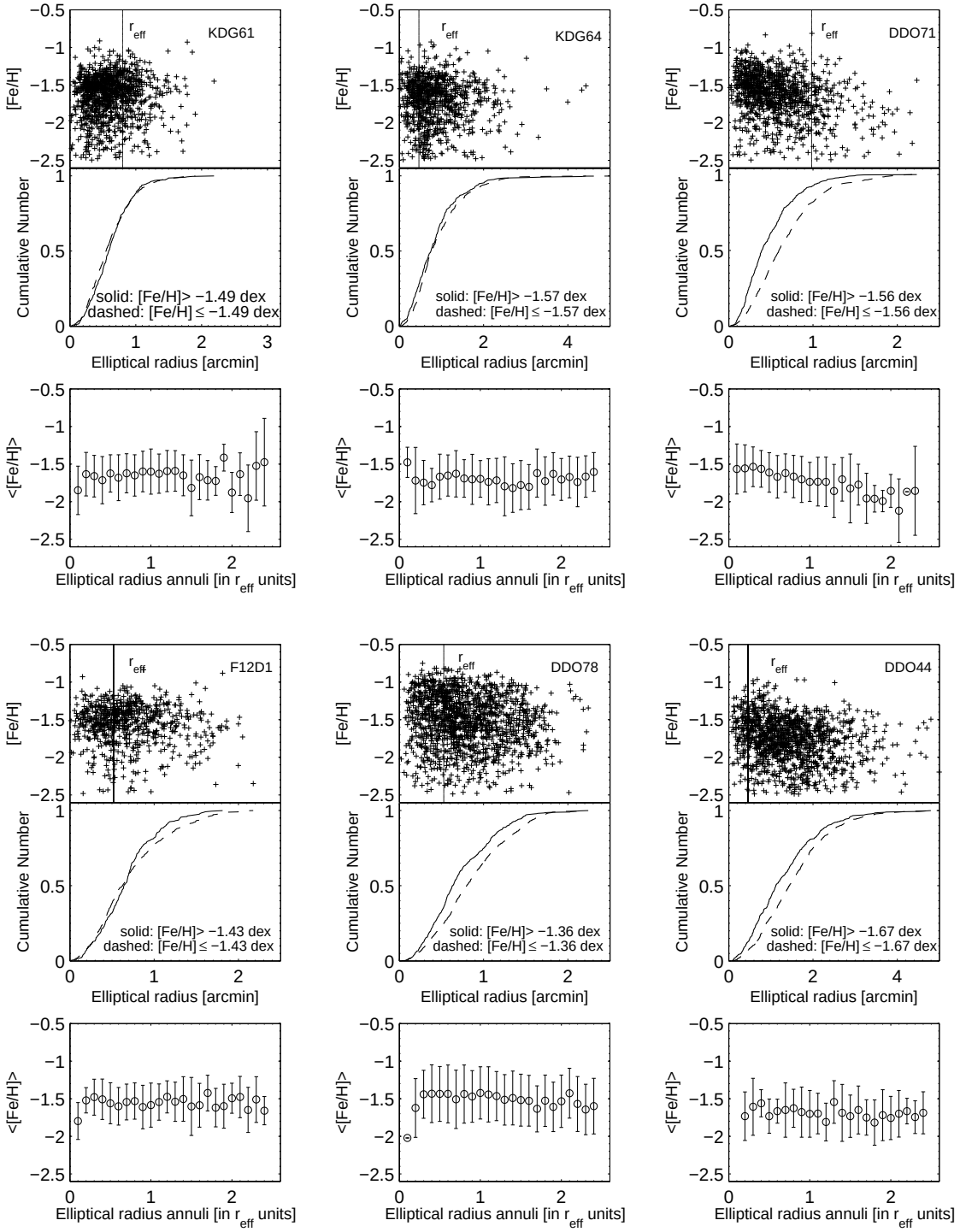

Figure 3.8: In each panel from left to right and from top to bottom we show the radial metallicity distributions (top panels), their cumulative distributions (middle panels), and the radial mean metallicity profile (bottom panels). The cumulative histogram is for stars selected in metallicity above and below the weighted mean value $\langle$[Fe/H]$\rangle_w$ listed in Table 3.3.

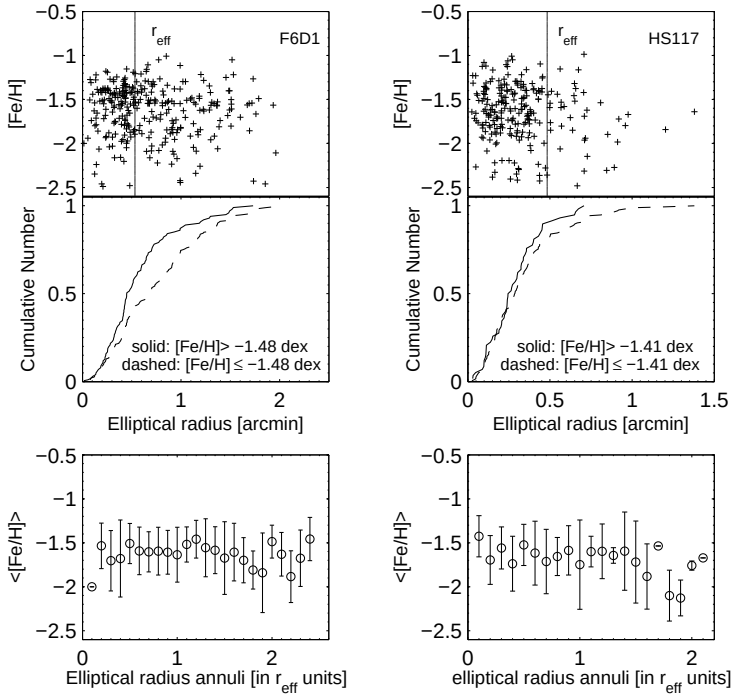

Figure 3.9: Same as in Fig. 3.8 for the remaining two dSphs. Note that IKN is excluded from this analysis.

3.3.5 Luminous AGB stars

As already noted before, all the dSphs in our sample contain a significant number of luminous AGB star candidates. These stars are located above the TRGB and have ages ranging from 1 Gyr up to less than 10 Gyr. We broadly refer to stellar populations in this age range as "intermediate-age" populations. Assuming that the metallicities of dwarf galaxies increase with time as star formation continues, we may also assume that these intermediate-age populations are more metal-rich than the old populations. We note, however, that dwarf galaxies do not necessarily experience smooth metal enrichment as a function of time (see, e.g., Koch et al. 2007a, 2007b).

In Fig. 3.10 and Fig. 3.11, the density maps in the lower panels show the spatial distribution of these intermediate-age stars for each dSph. We consider as luminous AGB stars the stars that are brighter by 0.15 mag than the TRGB (Armandroff et al. 1993) and that lie within 1 mag above ($I_{TRGB}-0.15$) mag. In addition, we consider stars within the color range of $a < (V-I)_0 < a+2.50$ (mag), where the left-hand limit a is equal to the color of the TRGB of the most metal-poor isochrone we use, dereddened for each dSph using the extinction values listed in columns (6) and (7) of Table 3.2. Then, the right-hand limit is the left-hand limit plus 2.50 mag. This selection criterion was motivated by the work of

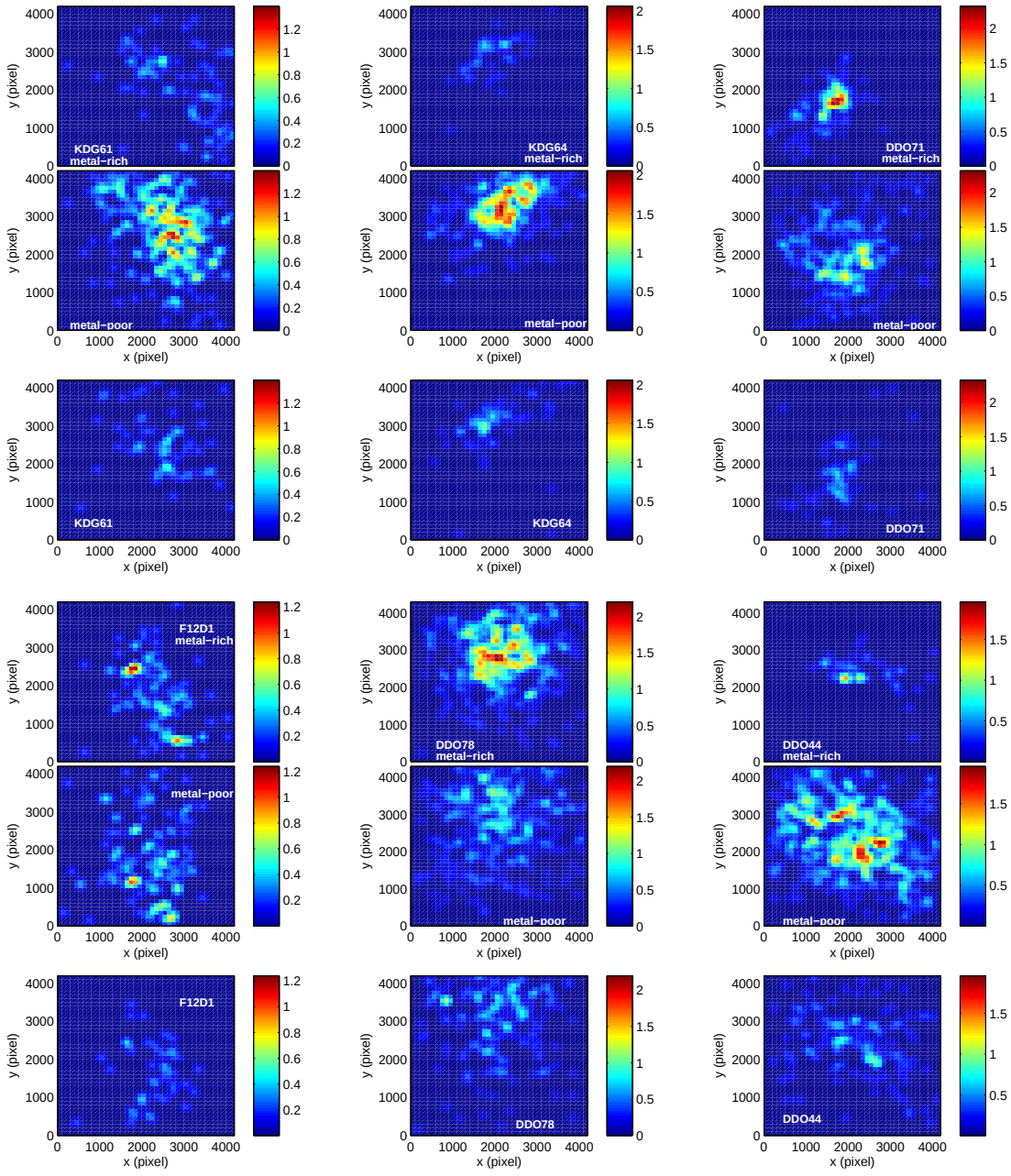

Figure 3.10: From left to right and from top to bottom we show the density maps for each dSph, after smoothing with a Gaussian kernel. In each upper and middle panel, the "metal-rich" population corresponds to stars having [Fe/H]≥ -1.30 dex while "metal-poor" refers to [Fe/H]≤ -1.80. The bottom panel corresponds to the density map of the luminous AGB stars, as defined in the text. The unit of the colorbars is number of stars per (100 pixels)^2.

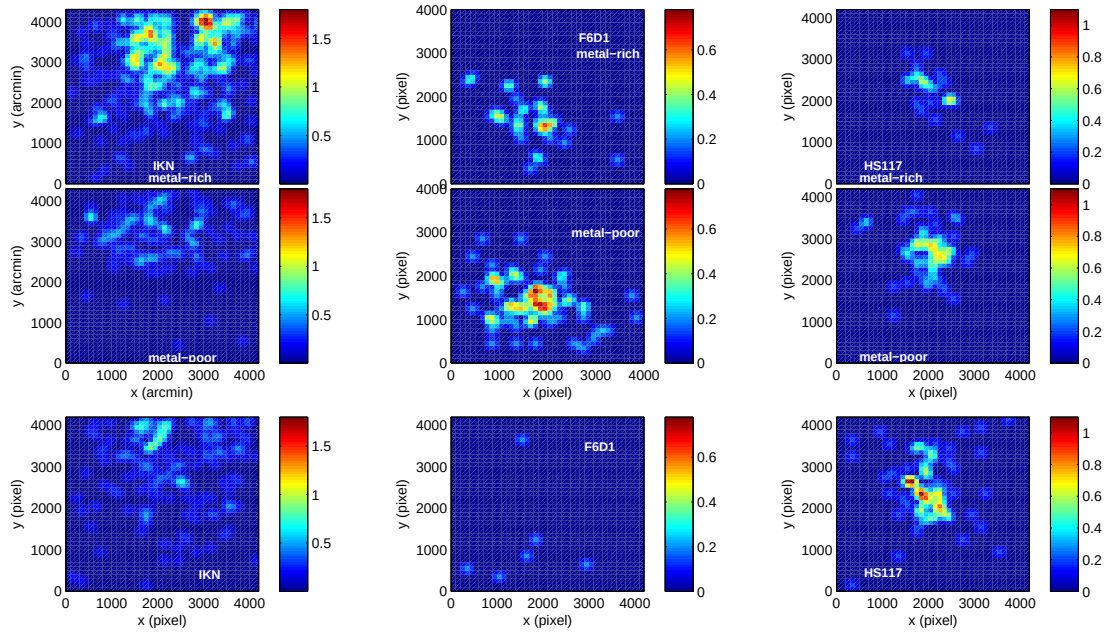

Figure 3.11: The same as in Fig. 3.10 but for the remaining three dSphs. Note that the zero density region in the center of IKN is an artifact due to a bright star contaminating the field of view.

Brewer, Richer & Crabtree (1995) and Reid & Mould (1984).

3.4 Discussion

3.4.1 Photometric metallicity distribution functions

The photometric MDFs in Fig. 3.2 indicate that these dSphs cover a wide range in metallicity. All of them seem to have a steeper cut-off in their metal-rich end. This can be easily seen if we compare the MDFs to the fitted gaussian distributions, indicated by the dashed lines in Fig. 3.2. We do not expect the MDFs to follow a gaussian distribution since they are shaped by the star formation histories of each dSph. For instance, a steep cut-off of the MDF toward the metal-rich tail could be indicative of the occurrence of strong and continuous galactic winds (Lanfranchi & Matteucci 2003, 2007; Koch et al. 2006) or of the effects of extended star formation and SNe Ia "pockets" of localised, inhomogeneous enrichment (Marcolini et al. 2008).

The low mean metallicities, $\langle$[Fe/H]$\rangle$, that are derived from the distribution functions and are shown in Table 3.3, columns (2) and (3), indicate that the M 81 dSphs are metal-poor systems, which points to a low star formation efficiency in analogy with the Local Group dSphs (e.g., Lanfranchi & Matteucci

2003; Grebel, Gallagher & Harbeck 2003; Koch 2009).

One exception is the dSph IKN, which shows a high mean metallicity for its luminosity. Objects that have high metallicity for their luminosity and that, most importantly, are dark matter free are promising candidates for tidal dwarf galaxies. Their properties are set by their formation mechanism. They are believed to form out of the dark matter free material that was expelled during the tidal interaction of the parent galaxies (Bournaud et al. 2007; and references therein). One possible tidal dwarf galaxy candidate has been identified in the M 81 group, namely Holmberg IX (Makarova et al. 2002; Sabbi et al. 2008) and these are favoured to be detected in such recently interacting groups. These systems contain a young stellar component, while their older stellar populations are believed to consist of stars from their parent galaxies, which is M 81 in the case of Holmberg IX.

In the case of IKN, we should consider the fact that its stellar metallicity bears the imprint of the medium that formed these old stars, while young stars are not observed in this dwarf. That makes it distinct from young tidal dwarf candidates like Holmberg IX. A connection with the recent interactions of the M 81 group is not obvious. IKN lies at a deprojected distance of 110 kpc (or 147 kpc if we use the updated TRGB distance measurement of Karachentsev et al. 2006) from the M 81 galaxy.

IKN might be an old tidal dwarf galaxy if such systems exist. Hunter, Hunsberger & Roye (2000) studied a sample of dwarf irregular galaxies within the context of identifying old tidal dwarf galaxies. In order to identify potential old tidal dwarf galaxies, they used the baryonic Tully–Fisher relation, the luminosity–metallicity relation, the structure and the stellar populations of their dwarf galaxy sample. In the baryonic Tully–Fisher relation, potential old tidal dwarf galaxies would have rotational velocities that would be too small for their luminosity and thus would significantly deviate from the baryonic Tully–Fisher relation (Hunter, Hunsberger & Roye 2000). Dwarfs with the latter property may be old tidal dwarf galaxies candidates due to their small dark matter content as compared to their baryonic mass. There is no information available about the presence or absence of dark matter in IKN. This system is classified as dSph with no H I associated or H α detected so far (Karachentsev & Kaisin 2007). In pressure–supported systems one can estimate their dark matter content through their velocity dispersion profiles (e. g. Koch et al. 2007b; Walker et al. 2009b). Due to its distance, velocity measurements for IKN are not currently possible.

Furthermore, tidal dwarf galaxies are formed from the material expelled from their parent galaxies. In this process, it is expected that tidal dwarf galaxies contain up to 40% old stars inherited by its parent galaxy (Hunter, Hunsberger & Roye 2000; and references therein). Therefore, one would expect that the metallicity of the old stars of a potential tidal dwarf galaxy would be comparable to the metallicity of the old stars of their parent galaxy. Interestingly, IKN's high stellar metallicity of -1.38 dex that we estimate in this study is comparable with the stellar metallicity estimates of the halo of the M 81 galaxy. The mean metallicity of the halo of the M 81 galaxy is -1.25 dex, as derived through interpolation

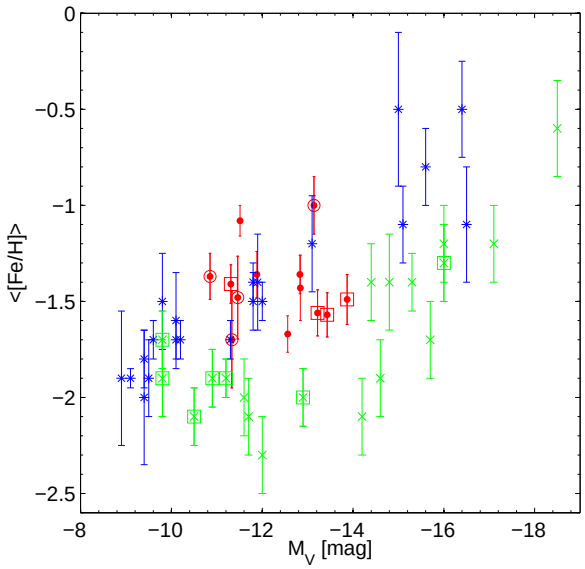

Figure 3.12: Luminosity-metallicity relation for Local Group dwarf galaxies, after Grebel, Gallagher & Harbeck (2003), together with the 13 dSphs of the M 81 group. Local Group dSphs are plotted with blue asterisks, Local Group dIrrs are shown as green crosses, and red dots indicate the available M 81 data. Nine out of the thirteen M 81 group dSphs have been studied here, while the remaining four, marked with a red circled dot, have been adopted from the literature, as discussed in the text. The red squared dots and green squared crosses indicate the transition-types of the M 81 group and Local Group, respectively.

between RGB fiducials of GCs (Mouhcine et al. 2005).

Alternatively, IKN may have undergone substantial mass loss in the past, leaving it as a low-luminosity but comparatively high-metallicity dSph, though we note that its total luminosity may have been underestimated due to the foreground star that is obscuring a part of IKN. Without data on its detailed structure and kinematics, we cannot distinguish between these possibilities.

The metallicity spreads of the studied dSphs are large, spanning 1 σ ranges from 0.27 dex to 0.37 dex, or intrinsic, error-weighted 1 σ ranges from 0.16 dex to 0.43 dex. These abundance spreads are comparable to the ones observed in the Local Group dSphs (Grebel, Gallagher & Harbeck 2003; Koch 2009) and may indicate the presence of multiple stellar populations and / or extended star formation histories. According to the models of Marcolini et al. (2008) and Ikuta & Arimoto (2002), the initial star formation in dSphs may have lasted as long as 3 Gyr or even longer, which can lead to a large dispersion in [Fe/H]. For ages older than 10 Gyr, the shape of the MDF does not depend strongly on age as described in Sec. 3. 3. 2 and shown in Fig. 3.6.

3.4.2 Luminosity–metallicity relation

In Fig. 3.12, we show the luminosity-metallicity relation compiled for the dwarf galaxies in our Local Group as studied by Grebel, Gallagher & Harbeck (2003), with the addition of thirteen dSphs in the M 81 group. This compilation includes Local Group objects with mean metallicities derived from either spectroscopic or photometric studies. The mean metallicities for the nine M 81 group dSphs listed in Table 3.3, column (3), are from this work, while the metallicities for the remaining four dSphs are adopted from the literature and are computed using the mean $(V-I)_0$ color of the RGB stars at the luminosity of $M_I = -3.5$ mag (from Caldwell et al. (1998) for BK5N and F8D1 and from Sharina et al. (2008) for KKH 57 and BK6N).

In order to see how the metallicities of the dSphs adopted from the literature compare with the metallicities we derive with the isochrone interpolation, we re–derive the mean metallicities of our sample using the mean $(V-I)_0$ color of the RGB at the luminosity of $M_I = -3.5$ mag (Lee, Freedman & Madore 1993). At this luminosity, the photometric errors of dwarf galaxies are smaller than the photometric errors in the luminosity of $M_I = -3$ mag, which was initially chosen by Da Costa & Armandroff (1990) due to the small contribution of old AGB stars in their study of Galactic GCs. We use the relation of Lee et al. (1993) defined for the V– and I–band filters, therefore, we use the magnitudes of the stars of each galaxy in the V– and I–band as given from the Dolphot output (see also Sec. 3.2). The resulting mean metallicities are -1.66 ± 0.21 dex for KDG 61, -1.75 ± 0.21 dex for KDG 64, -1.63 ± 0.22 dex for DDO 71, -1.53 ± 0.24 dex for F12 D1, -2.83 ± 1.47 dex for DDO 78, -2.13 ± 1.03 dex for DDO 44, -1.41 ± 0.85 dex for IKN, -1.62 ± 0.20 dex for F6 D1, and -1.65 ± 0.92 dex for HS 117. In the majority of the cases, the mean metallicities $\langle$[Fe/H]$\rangle$ are in excellent agreement between the two methods. There is a poor agreement between the mean metallicities of DDO 78 and DDO 44. These two dSphs are observed in the F 475 W–band of the ACS filter system, and although we used the transformed V–band filter to compute the mean metallicity, the color transformations are sensitive to the object's spectral details (Sirianni et al. 2005). Finally, in the case of the dSphs with shallower data, the 1–σ spread of the metallicities are substantially high due to the photometric errors. We can conclude that the metallicities derived from either method compare quite well.

Overall, the M 81 group dwarfs follow the luminosity-metallicity relation quite well, albeit some of them exhibit a tendency of being slightly more metal-poor than Local Group dSphs of comparable luminosity. Therefore, they mainly populate the region defined by the Local Group dSphs while a few are located in the border region between the dSph and dIrr locus defined by the Local Group dwarfs. The M 81 group dSphs that seem to lie in this apparent transition region are KDG 61, KDG 64, DDO 44 and DDO 71. Out of these four objects, three are classified as transition-types, namely, KDG 61, KDG 64 and DDO 71 (Karachentsev & Kaisin 2007; Boyce et al. 2001) based on HI detections and $H\alpha$ emission. Also among the dwarfs that coincide with the Local Group dSph locus, one dwarf is classified as

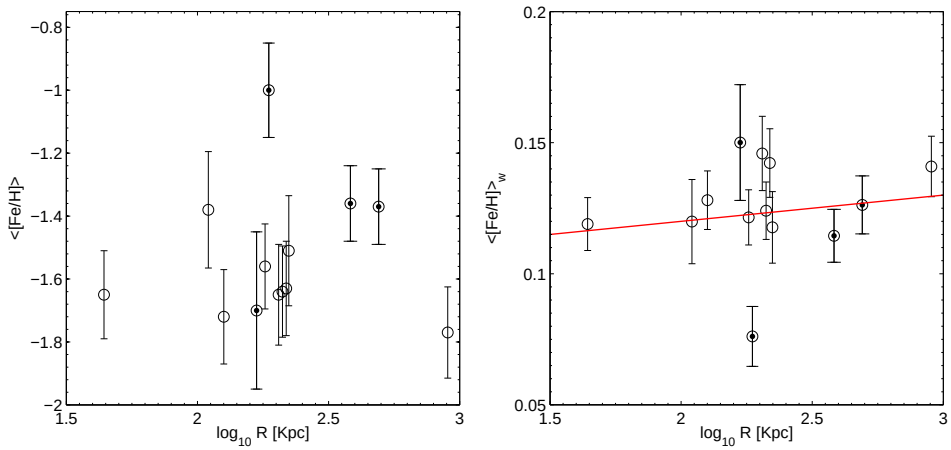

Figure 3.13: *Left*: Mean metallicities versus the deprojected distance, R, from the M 81 galaxy for the 13 M 81 group dSphs. The circled dots correspond to the four dSphs for which the metallicities were adopted from the literature, as discussed in the text. The error bars indicate the 1–σ spread of the metallicity. *Right*: Luminosity–weighted mean metallicities versus the deprojected distance, R, from the M 81 galaxy for the 13 M 81 group dSphs. The red solid line corresponds to the linear least–squares fit to the datapoints. The error bars indicate the 1–σ spread of the metallicity weighted by the luminosity. The circled dots correspond to the mean metallicities adopted from the literature, as discussed in the text.

transition-type, namely HS 117, with HI associated with it (Huchtmeier & Skillman 1998; Karachentsev et al. 2006). At this point, we note that the mean metallicities for the Local Group dwarf galaxies are derived using their RGB stars either through spectroscopic or through photometric methods (Grebel, Gallagher & Harbeck 2003; Grebel 2000). The mean metallicities derived from photometric and spectroscopic measurements of red giants are in quite good agreement (as is shown in the next chapter), with the observed tendency of the dSphs with more extended star formation history to have photometric metallicities slightly more metal–poor than the ones derived from spectroscopic measurements. Therefore, the photometric metallicities derived for the M 81 group dSphs in this work and the ones derived for the Local Group dwarfs are on roughly comparable scales and lead to a true observed trend in the luminosity–metallicity relation. This trend is going to be enhanced in the case of dSphs with an extended star formation history, since their metallicities may be slightly more metal–rich than what we derived with the photometric method.

Transition-type dwarfs are galaxies that share properties of both morphological types. Their stellar populations and star formation histories resemble those of dSphs and their gas content and present-day star formation activity is akin to low-mass dIrrs. It has been suggested that transition-type dwarfs are indeed evolving from dIrrs to gas-deficient dSphs.

The projected spatial distribution of the dSphs within the M 81 group is shown in Fig. 1 of Karachent-

sev et al. (2002), while their three-dimensional view is shown in their Fig. 6. In Fig. 3.13, left panel, we plot the deprojected distances from the M 81 galaxy, R, versus the mean metallicities for the 13 M 81 group dSphs. The deprojected distances from the M 81 galaxy, R, are adopted from Karachentsev et al. (2002) and are listed in Table 3.2, column (9). The most distant dSph is DDO 44 which belongs to the NGC 2403 subgroup, while KDG 61 is the one closest to the M 81 itself. Interestingly, the dwarf KDG 61 which is classified as a transition–type based on HI detections, is the closest to the M 81 itself, with a deprojected distance of 44 kpc (Karachentsev et al. 2002). The remaining three dwarfs classified as transition-types, namely KDG 64, DDO 71 and HS 117, lie in a deprojected distance of more than 100 kpc. As discussed already, the most metal-rich dSph studied by us is IKN, while according to the value that Caldwell et al. (1998) provide for F8D1, this is the most metal-rich dSph in this group so far studied. We see no trend of the mean metallicity with the deprojected distance.

In Fig. 3.13, right panel, we instead plot the luminosity–weighted mean metallicities as a function of the deprojected distances from the M 81 galaxy, R. The weights correspond to the visual absolute magnitude, M_V, listed in Table 3.2. The red solid line is an error–weighted linear fit to the data with a slope of 0.01 ± 0.13, while the correlation is insignificant within the 90% confidence level. Given the luminosity–metallicity relation where the mean metallicities are found to correlate with galaxy luminosity, the latter being a tracer of the potential of each galaxy, the mean metallicities weighted by luminosity may provide valuable information on the influence of the environment alone on the chemical evolution of each galaxy.

3.4.3 Population gradients

By examining the cumulative metallicity distributions in the middle panels in Fig. 3.8 and Fig. 3.9, we conclude that the metallicity gradients are present in the case of DDO 71, DDO 78, DDO 44 and F6D1, while the metallicity gradients are less pronounced or not present in the remaining dSphs. We again separate the RGB stars in each dSph into two samples, where we choose to separate the distributions at the observed weighted mean metallicity. The probabilities from the two-sided Kolmogorov-Smirnov (K-S) test that the two components are drawn from the same parent distribution are listed in Table 3.3, column (4). The K-S results are consistent with showing spatially separated populations in the case of DDO 71, DDO 78, DDO 44 and F6D1. In the case of the remaining dSphs, the gradients are less pronounced and the metal-rich and metal-poor populations have different distributions at the 84 – 99.7 % confidence level ($>1.5\ \sigma$), except for HS 117. In all cases, in which we observe such metallicity segregation, the sense is that more metal rich stars are more centrally concentrated, as also found in the majority of the Local Group dSphs (Harbeck et al. 2001; Tolstoy et al. 2004; Ibata et al. 2006). Since the majority of the dSphs present either a strong or a milder metallicity gradient, this would imply that they lack of SNe II events that would homogenise their metal distribution across the galaxy and therefore erase any

Table 3.5: Metallicity gradients.

Galaxy	$[\mathrm{Fe/H}]_{gradient}$ (dex per kpc)
(1)	(2)
DDO 71	-0.23 ± 0.02
F 12D 1	-0.12 ± 0.03
HS 117	-0.08 ± 0.03
DDO 78	-0.07 ± 0.02
DDO 44	-0.07 ± 0.01
F 6D 1	-0.03 ± 0.04
KDG 64	-0.02 ± 0.02
KDG 61	$+0.08 \pm 0.03$

gradient information (Marcolini et al. 2008).

An error–weighted linear least squares fit to the data points of the metallicity distributions in Fig. 3.8 and Fig. 3.9 yields a metallicity gradient of -0.23 dex per kpc for DDO 71, which presents the strongest metallicity gradient, while in the case of KDG 64 a metallicity gradient of -0.02 dex per kpc is present, thus showing the least significant metallicity gradient. The metallicity gradients are listed in Table 3.5, sorted by decreasing metallicity gradient. Interestingly, one of our studied dSphs, namely KDG 61, presents a positive metallicity gradient, of the order of $+0.08$ dex per kpc, in the sense that there is an increase of the metallicity with increasing the elliptical radius. Such positive metallicity gradients can be explained assuming that the star formation occurs in shells that propagate outwards thus leading to a chemical enrichment of the interstellar medium towards the same direction (Mori et al. 1997). In Fig. 3.14 we show the metallicity gradient, listed in Table 3.5 as a function of the deprojected distance, R, from the M81 galaxy. The red solid line shows the error–weighted linear least squares fit to the data with a slope of -0.25 ± 0.11, where there is no correlation within the 98% confidence level. Considering that the deprojected distances show each dSph's current distance from the M 81 galaxy, it is not possible to draw any conclusion for the effects of any environmental mechanisms acting on these dwarfs.

3.4.4 Density maps of populations of different metallicities

The density maps in Fig. 3.10 and Fig. 3.11 are useful to study the spatial distribution of the metal-rich (upper panels) and metal-poor (middle panels) population of each dSph. From these density maps we conclude that each dSph has a different stellar spatial distribution of their metal-rich and metal-poor stellar component. All of them show either a spatial variation of the centroids of the two stellar populations, as is the case of F12D1 and KDG 64, or that the metal-rich population is more centrally concentrated, as is the case of DDO 71, DDO 44 and F6D1. These findings agree well with the ones

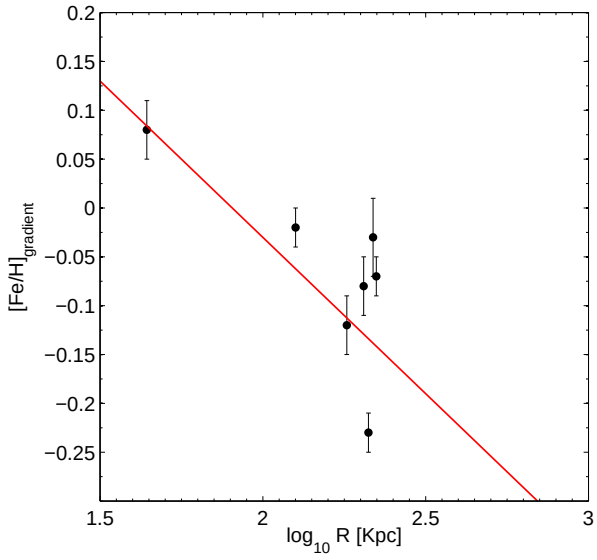

Figure 3.14: Metallicity gradient as a function of the deprojected distance from the M 81 galaxy, for the nine M 81 group dSphs studied here. The red solid line shows the error–weighted linear least squares fit to the data.

from the cumulative histograms, though we should keep in mind that the metal-poor and metal-rich stellar populations involved are differently selected. DDO 78 and IKN are clearly fairly metal-rich while KDG 61, KDG 64 and DDO 44 have prominent metal-poor populations.

3.4.5 Luminous AGB stars

Luminous AGB stars were also detected in two more dSphs in the M 81 group, namely BK5N and F8D1 (Caldwell et al. 1998). These luminous AGB stars may include carbon stars and may be long-period variables (LPVs) as have been found in other early-type dwarf galaxies (e.g., Menzies et al. 2002; Rejkuba et al. 2006; Whitelock et al. 2009), but we can not establish this for certain based on our current data. We compute the fraction of the luminous AGB stars, f_{AGB}, defined as the number of the luminous AGB stars, N_{AGB}, counted within the magnitude bin considered in Sec. 3. 3. 5, over the number of the RGB stars within one magnitude below the TRGB, N_{RGB}. In order to estimate the N_{RGB}, we take into account that approximately 22 % of the stars we count within one magnitude below the TRGB are old AGB stars (Durrell, Harris & Pritchet 2001). Thus, the N_{RGB} is equal to 78 % of the stars we count within one mag below the TRGB. The fractions f_{AGB} we derive in this way are listed in Table 3.3, column (5).

Blends, blue straggler progeny and foreground contamination

We now discuss the possibility that these luminous AGB stars may actually be (1) blends of bright RGB stars (Renzini 1998), (2) blue straggler progeny (Guarnieri, Renzini & Ortolani 1997; and references therein), or (3) due to the foreground contamination.

In order to evaluate case (1), we use our artificial star experiments in order to quantify the number of the blends of bright RGB stars, N_{blends}, that may contribute to the detected number of the observed luminous AGB stars. We only consider here the case of a blend of two equal-magnitude stars. The magnitude of the blended star is always 0.75 mag brighter than the initial magnitude of the two superimposed stars.

We want to determine the location in the CMD of all the RGB stars that can end up as blends within the location in the CMD of the luminous AGB stars, as defined in Sec. 2. 3. 5 and further called as luminous AGB box. For that purpose, if we assume that the stars within the luminous AGB box were all blends, then they would originate from stars that have magnitudes 0.75 mag fainter. Thus, we shift the luminous AGB box by 0.75 mag towards the fainter magnitudes and furthermore we only consider the stars with magnitudes fainter than the TRGB. This procedure defines the location of the RGB stars that can end up as blends within the luminous AGB box and we call this the "RGB blends box".

From the stellar catalogue we use as an input for the artificial star experiments, we select the stars that have such input magnitudes to place them within the "RGB blends box". From these input stars, we consider as blends the ones that have output magnitudes that can place them above the TRGB. We normalise the number of these blends to the number of the total input stars that are located within the "RGB blends box". Finally, the number of the observed blends is proportional to the number of the observed RGB stars located within the same "RGB blends box". Thus, the N_{blends} for all the dSphs computed this way is equal to 5 blends, 11 blends, 12 blends and 2 blends in the case of DDO 44, DDO 78, IKN and HS 117, respectively, while in all the other cases the number of blends is less than 1. Thus, the fraction of the blends defined as the number of blends divided by the number of the RGB stars within 1 mag below the TRGB, is less than 0.6 % in all cases but for IKN which is equal to 0.9 %.

In the case (2), Guarnieri, Renzini & Ortolani (1997) point out that the number of blue straggler progeny is of the order of $\sim$2 % of all stars that reach the luminous AGB phase.

In the case (3), we estimate the foreground contamination using the TRILEGAL code (Vanhollebeke, Groenewegen & Girardi 2009; Girardi et al. 2005). We count the number of foreground stars that fall within the same location in the CMD as in the luminous AGB box and these are considered to be the number of expected foreground contamination. In all the cases, the number of foreground stars is 4, with the exception of DDO 71 and DDO 44 where the number of foreground stars is 3 and 5, respectively. This translates to a fraction of foreground stars, defined as the number of foreground

stars divided by the number of RGB stars within 1 mag below the TRGB, of less than 0.7 %, with the exception of F6D1 where this fraction is equal to 2 %.

We do not consider the case of old AGB LPVs, whose large amplitude variations may place them above the TRGB (Caldwell et al. 1998), as an additional source of contamination in the luminous AGB box, since the studied dSphs have mean metallicities of less than -1 dex. Such old AGB LPVs, with ages greater than or equal to 10 Gyr, have been observed above the TRGB in metal-rich ([Fe/H] $>$ -1 dex) globular clusters (e.g., Guarnieri, Renzini & Ortolani 1997; and references therein).

We can now add all the contributions estimated in the above three cases, for each dSph. We call the sum of these three contributions the number of total contaminants, $N_{cont,tot}$, and compute their fraction $f_{cont,tot} = N_{cont,tot} \,/\, N_{RGB}$. The fraction of the total contaminants is less than 1 % in all cases apart from IKN, HS 117 and F6D1, where the fraction of the total contaminants is approximately 1.1 %, 1.3 % and 2.1 %, respectively. We note that in all cases, there is a significant fraction of luminous AGB stars that can not be accounted for by considering the contribution of blends, binaries and foreground contamination. The dSph F6D1 is an exception to that, where the $f_{cont,tot}$ is $\sim$ 2 %, as compared to the f_{AGB} which is $\sim$ 3 %. We note though that in the case of F6D1 the number of stars counted in the luminous AGB box is equal to 6 stars. Thus, we conclude that the luminous AGB stars are a genuine population for the majority of the dSphs studied here.

These small fractions of luminous AGB stars of less than 1% probe the fraction of the intermediate age stars present in these dSphs and indicate that this is negligible. Therefore, the bulk of the star formation in these dSphs occurred at ancient times, justifying our assumption of an old age used to derive their photometric MDFs.

Luminous AGB density maps and fractions

From the density maps of the luminous AGB stars shown in Fig. 3.10 and Fig. 3.11, lower panels, we see that if we consider the peak densities or the bulk of the luminous AGB stars, then it seems that these are more confined to the central regions of the dwarfs, a behaviour similar to what is found for the Fornax dSph (Stetson, Hesser & Smecker-Hane 1998). If we consider the overall distribution then we note that for most of the dSphs these stars are rather more widely distributed, following the distribution of the metal-poor stars, with the exception of KDG 64 and DDO 71 where their AGB stars' distributions coincide mostly with the metal-rich population, which in the case of DDO 71 is centrally concentrated. We conclude that the intermediate-age stellar component is well-mixed with the old stellar component.

This behaviour is similar to the AGB stars' spatial distribution of the Local Group dwarfs. Indeed, Battinelli & Demers (2004a; and references therein) discuss that for the Local Group dwarfs, for which there are carbon star studies, their Carbon-rich stars are distributed such that they coincide with the

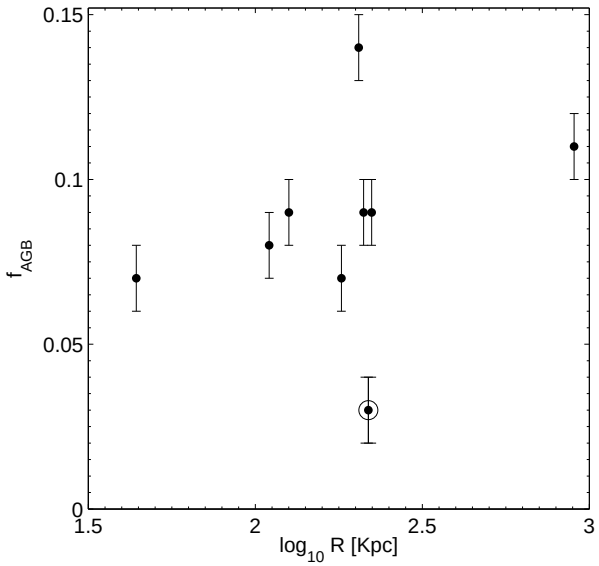

Figure 3.15: Fraction of AGB stars versus the RGB stars within 1 mag below the TRGB, f_{AGB}, versus the deprojected distance from M 81, R, for the nine M 81 group dSphs studied here. With the circled dot we show the corresponding fraction f_{AGB} in the case of F6D1.

spatial distribution of the old stellar component. An exception is the dE NGC 185, where the AGB stars are concentrated more in the centre than the old stellar component (Battinelli & Demers 2004b), a similar behaviour as observed in the two M 81 group dSphs discussed above.

We plot the f_{AGB} versus the deprojected distance from M 81, R, in Fig 3.15. The highest fraction of luminous AGB stars is observed in HS 117 and the lowest one in KDG 61 and F12D1. We do not see any trend of the f_{AGB} with increasing deprojected distance from M 81. If we compute the net fraction of the luminous AGB stars, by subtracting the fraction $f_{cont,tot}$, due to the contribution of blends, binaries and foreground contamination, from the fraction f_{AGB} listed in the column (5) of Table 3.3, none of the trends and conclusions change.

3.5 Conclusions

We use the CMDs of nine dSphs in the M 81 group to construct their photometric MDFs. These MDFs show populations covering a wide range in metallicity with low mean metallicities indicating that these are metal-poor systems. All MDFs show a steeper fall-off at their high-metallicity end than toward their low-metallicity end indicating that galactic winds may play a role in shaping their distribution.

We compute the mean metallicity, $\langle$[Fe/H]$\rangle$, and the mean metallicity weighted by the metallicity

error, $\langle$[Fe/H]$\rangle_w$, along with their corresponding standard deviations. The most metal-rich dSph in our sample is IKN even though it is the least luminous galaxy in our sample. IKN's comparatively high metallicity may indicate that it is a tidal dwarf galaxy or that it suffered substantial mass loss in the past. We do not see any correlation between the $\langle$[Fe/H]$\rangle$ and the deprojected distance from the M 81 galaxy, R.

We use the mean metallicity weighted by the metallicity errors, $\langle$[Fe/H]$\rangle_w$, to select two stellar populations having metallicities above and below that value. For these two stellar populations we construct cumulative histograms, as a way to search for population gradients in metallicity. We find that some dSphs show strong metallicity gradients, while others do not. In dSphs with radial metallicity gradients the more metal-rich populations are more centrally concentrated.

Furthermore, we study the spatial (i.e., two-dimensional) distribution of our defined metal-rich and metal-poor stellar populations. This refined look no longer assumes radial symmetry, and we now find that in some dwarfs the metal-rich population is more centrally concentrated, while others show offsets in the centroid of the two populations. By examining the distribution of the luminous AGB stars, we conclude that, for the majority of the dSphs, these stars have mostly extended distributions, indicating that they have been well-mixed with the metal-poor stellar population. We do not find any correlation between the fraction of luminous AGB stars and the deprojected distance from the M 81 galaxy. While present-day distances may not be indicative of the dwarfs' position in the past and while their orbits are unknown, the apparent lack of a correlation between distance and evolutionary history may suggest that the evolution of the dwarfs was determined to a large extend by their internal properties and not so much by their environment.

Finally, there are some M 81 dSphs that straddle the transition region between Local Group dSphs and dIrrs in the metallicity-luminosity relation. We may be observing low-luminosity transition-type dwarfs moving toward the dSph locus. Interestingly, these dwarfs are slightly more luminous than the bulk of the Local Group transition dwarfs. Perhaps some of the M 81 dwarfs experienced gas stripping during the recent interactions between the dominant galaxies in the M 81 group.

Chapter 4

Spectroscopic versus Photometric Metallicities : Dwarf Spheroidal Galaxies as a Test Case

4.1 Introduction

There are several reliable techniques one can use to derive the photometric metallicities of a stellar system using its resolved old red giant branches (RGBs). These include the use of the $(V-I)_o$ color of the RGB stars at the luminosity corresponding to $M_I = -3.0$ mag or $M_I = -3.5$ mag in conjunction with the empirical relations defined in Da Costa & Armandroff (1990), in Armandroff et al. (1993) and in Lee, Freedman & Madore (1993); the use of the fiducial ridge lines or analytic functions of Galactic globular clusters (GCs) with known metal abundances; as well as the use of theoretical stellar tracks or isochrones (Mould, Kristian & Da Costa 1983; Grebel & Guhathakurta 1999; Harris, Harris & Poole 1999; Harris & Harris 2000, 2002; Saviane et al. 2000; Sarajedini et al. 2002; Caldwell 2006; Williams et al. 2007; Crnojevic, Grebel & Koch 2010; Lianou, Grebel & Koch 2010). The latter two techniques serve to either bracket the range of the metal abundances or to interpolate between them in order to derive the metallicity distribution function. In the case of GCs, dwarf spheroidals (dSphs), and the haloes of galaxies, the assumption under which these techniques are used is that the red giants represent populations of an old age (≥ 10 Gyr). For such old populations, a spread in metallicity produces a broader RGB than would an age spread (Frayn & Gilmore 2002).

The case of the Local Group (LG) dSphs has shown that all of them have a population of old stars (Grebel 2001; Grebel & Gallagher 2004), while a subsample of these systems contains an intermediate

age component (from 1 Gyr up to less than 10 Gyr) in addition to early star formation, thus presenting a rather complex star formation history (SFH) (Grebel 1997; Mateo 1998; Tolstoy, Hill & Tosi 2009; Cignoni & Tosi 2010). Although spectroscopic observations of individual stars, ideally in high–resolution, provide the best means to reveal and break an age–metallicity degeneracy in systems with complex SFHs, as for instance in the case of Carina (Smecker–Hane et al. 1994; Koch et al. 2006), such studies are limited to nearby objects within the LG due to the faintness of the stars to be targeted. Based on the fact that the LG dSphs show complex SFHs, the assumption of a single old age for their stellar populations does not hold, thus it is worth exploring how this assumption affects the photometrically derived metallicities of composite populations with a range of ages.

In the present work we perform a comparison of the mean metallicity properties as well as a direct star–by–star comparison between the spectroscopically and the photometrically derived metallicities. In this latter case we use the stars in common to both samples, using LG dSphs that have been studied in the literature in great detail using both spectroscopic and photometric observations. In order to perform such a star–by–star comparison, we use spectroscopic metallicity results and available photometric datasets for five Galactic dSphs, namely Carina, Leo II, Fornax, Sextans and Sculptor. The three dSphs Carina, Leo II and Fornax have complex star formation and chemical enrichment histories, with a different fraction of their intermediate age stellar populations, while Sextans and Sculptor are dominated by old populations.

Carina appears to have episodic star formation with three distinct populations and with a pause of star formation for 4 Gyr (Smecker–Hane et al. 1994; Smecker–Hane et al. 1996; Mighell 1997; Hurley–Keller, Mateo & Nemec 1998; Monelli et al. 2003) where the majority of the stars formed around 7 Gyr ago (Hurley–Keller et al. 1998; Rizzi et al. 2003). Carina shows a mild radial metallicity gradient in the sense that the metal-rich population is more centrally concentrated (Koch et al. 2006). The same trend is observed for the intermediate age population (Harbeck et al. 2001; Monelli et al. 2003). Leo II has both old and intermediate age populations (Aaronson & Mould 1985; Lee 1995; Mighell & Rich 1996; Gullieuszik et al. 2008). It appears that there is no significant metallicity gradient present in Leo II (Koch et al. 2007). In the case of Fornax, the dominant population is of an intermediate age (ca. 3–4 Gyr; Coleman & de Jong 2008) and it also contains old and a young populations (Stetson, Hesser & Smecker–Hane 1998; Saviane, Held & Bertelli 2000b), while showing a strong radial metallicity gradient (Battaglia et al. 2006).

In the case of Sextans and Sculptor, the dominant population is of an old age (Lee et al. 2003, 2009 for Sextans; Hurley–Keller, Mateo & Grebel 1999 for Sculptor). Sextans shows a population gradient based on its horizontal branch morphology (Harbeck et al. 2001), as well as a metallicity gradient, where the metal–rich stars are more centrally concentrated and have colder kinematics than the metal–poor ones (Battaglia et al. 2010). Sculptor shows two distinct old stellar components (Hurley–Keller,

Mateo & Grebel 1999; Tolstoy et al. 2004), as well as a metallicity gradient (Harbeck et al. 2001). In addition, neutral hydrogen clouds appear to be associated with Sculptor (Bouchard, Carignan & Mashchenko 2003), and Battaglia et al. (2008) found likely signatures of an intrinsic rotation through detected velocity gradients.

The spectroscopic metallicities [Fe/H] of dSphs can be inferred either directly by high resolution measurements of individual Fe lines, or through low / medium resolution spectroscopic measurements of red giants. The latter method is the one widely used since it provides spectra for a large number of stars within a reasonable integration time and the spectroscopic [Fe/H] metallicities are inferred from the strength of the Ca II triplet (Ca T) lines at 8498 Å, 8542 Å and 8662 Å. The measured property is the sum of the equivalent widths, ΣW, either of two or of a combination of all three Ca T lines. The sum of the equivalent widths, ΣW is then used to derive the reduced equivalent width, W$'$, using empirical calibrations between the ΣW and the (V–V$_{HB}$), as defined in Armandroff & Da Costa (1991) who used the sum of the two strongest Ca T lines. The calibration of ΣW as a function of (V–V$_{HB}$) is chosen because it provides a calibration independent of the reddening and distance modulus (Armandroff & Da Costa 1991). The equivalent width W$'$ is then used to derive the metallicity, based on, for instance, a calibration of Galactic GCs spectroscopic iron abundances as a function of their reduced Ca T equivalent widths W$'$.

The Galactic GC metallicities are derived either using metallicity sensitive spectrophotometric indices of their integrated light or using high resolution spectroscopic measurements of their red giants. Thus, several metallicity scales have been defined so far, which include the Zinn & West (1984; hereafter ZW84), the Carretta & Gratton (1997; hereafter CG97), the Kraft & Ivans 2003; hereafter KI03) and the Carretta et al. (2009; hereafter CBG09) metallicity scales. The first one uses metallicity sensitive spectrophotometric indices of the integrated light of Galactic GCs, while the latter three use high resolution spectroscopic measurements of Galactic GC red giants to infer their iron abundance from individual Fe lines.

A calibration between Galactic GCs metallicity and the reduced equivalent width W$'$ of their red giants derived from Ca T is given by Armandroff & Da Costa (1991) and Da Costa & Armandroff (1995) in the ZW84 metallicity scale, while Rutledge, Hesser & Stetson (1997; hereafter R97) provide a calibration in the ZW84 and CG97 metallicity scales which includes a large sample of Galactic GCs. Among these calibrations, the definition of the Ca T sum of the equivalent widths, ΣW, is different. KI03 provide a similar calibration between their defined scale of iron abundances and the Ca T reduced equivalent widths W$'$ of GCs, as well as Carretta et al. (2009) for their defined metallicity scale. In Table 4.1 we show as an example the metallicities of three Galactic GCs with metallicities in the ZW84, CG97, KI03, and CBG09 metallicity scales, as well as the metallicity derived through isochrone fitting using Dartmouth isochrones (Dotter et al. 2007, 2008, 2010).

Table 4.1: Galactic GC metallicities in different metallicity scales.

GC	[Fe/H]$_{ZW84}$ (dex)	[Fe/H]$_{CG97}$ (dex)	[Fe/H]$_{KI03}$ (dex)	[Fe/H]$_{CBG09}$ (dex)	[Fe/H]$_{Dartmouth}$ (dex)
(1)	(2)	(3)	(4)	(5)	(6)
47 Tuc	-0.71 ± 0.05	-0.78 ± 0.02	-0.70 ± 0.09	-0.743 ± 0.026	-0.70
NGC 3201	-1.53 ± 0.03	-1.24 ± 0.03	-1.56 ± 0.10	-1.495 ± 0.073	-1.50
NGC 6397	-1.94 ± 0.02	-1.76 ± 0.03	-2.02 ± 0.07	-1.993 ± 0.060	-2.10

The Ca T method is calibrated on Galactic GCs, which are old populations and to first order, simple stellar populations, of a single metallicity, and have different chemical enrichment history as compared to the ones of the dSphs (Armandroff & Da Costa 1991; Venn et al. 2004; Koch et al. 2008a, 2008b). Nevertheless, this method is widely used to derive the metallicities of galaxies that have more complex star formation and chemical enrichment histories than that of the calibrating Galactic GCs. The implications of the different chemical enrichment and star formation history in the dSphs and the Galactic GCs for the Ca T method have been discussed in Da Costa & Hatzidimitriou (1998), Cole et al. (2000, 2004), Pont et al. (2004), Bosler et al. (2007), Battaglia et al. (2008) and Koch et al. (2008a). Cole et al. (2004) have shown that the effect is negligible as compared to the intrinsic scatter of the Ca T method for the metallicity ranges in CG97 between -2.0 and -0.2 dex in [Fe/H], while at lower metallicities there is an overestimate of the metallicities as compared with metallicities derived from high–resolution measurements (e.g. Battaglia et al. 2008; Koch et al. 2008a). Therefore, the Ca T method can be used to infer the metallicities of dSphs within the metallicity ranges of -2.0 dex to -0.2 dex and the age ranges of 2.5 Gyr to 13 Gyr (Cole et al. 2004), even though dSphs have experienced extended star formation and chemical evolution histories as compared to the calibrating Galactic GCs.

This chapter is structured as follows. In §2 we present the spectroscopic and photometric datasets we use. In §3 we show our results on the comparison of the mean metallicity properties as well as on the star–by–star comparison. In §4 we discuss our main findings and in §5 we present our conclusions.

4.2 Observations

We use the spectroscopic metallicities and the photometric results for the five Galactic dSphs Carina, Leo II, Fornax, Sextans and Sculptor. For Carina, the spectroscopic metallicities are adopted from Koch et al. (2006), for Leo II from Koch et al. (200), for Fornax from Battaglia et al. (2006), for Sextans from Battaglia et al. (2010; and private communication, 2010), and for Sculptor from Battaglia et al. (2008). We refer to these publications for the description of the spectroscopic observations and analysis. In all cases, the strength of the Ca T lines is used as a metallicity indicator for the individual red giant stars from either low or medium resolution spectroscopy. The spectroscopic metallicities for Carina, Leo II,

Table 4.2: Global properties.

Galaxy	M_V	A_V[a]	A_I[b]	$(m-M)_O$	TRGB
	(mag)	(mag)	(mag)	(mag)	(mag)
(1)	(2)	(3)	(4)	(5)	(6)
Carina	-9.4	0.18	0.11	19.87 ± 0.11	15.98 ± 0.10
Sextans	-9.5	0.03	0.02	19.90 ± 0.06	15.95 ± 0.04
Sculptor	-9.8	0.245	0.117	19.65 ± 0.14	15.70 ± 0.10
Leo II	-10.1	0.070	0.040	21.84 ± 0.13	18.35
Fornax	-13.1	0.067	0.039	20.72 ± 0.04	16.75 ± 0.02

[a] or A_g in the case of Leo II
[b] or A_i in the case of Leo II

Fornax and Sculptor are inferred through the calibration in the sense of R97, while for Sextans the calibration defined in Starkenburg et al. (2010) is used. The main difference between the calibration in Starkenburg et al. (2010) and in the remaining calibrations in the sense of R97 is that the first one is not a linear relation between the metallicity and the sum of the equivalent widths of the Ca T lines, Σ W, while the second is a linear one. In addition, the first one is calibrated to hold for metallicities from -4 dex to -0.5 dex, while the second, as already described earlier, is calibrated to hold from -2 dex to -0.2 dex. All the spectroscopic metallicities are placed in the CG97 metallicity scale.

The photometry of Carina, Fornax and Sculptor was adopted from Walker et al. (2009; and private communication, 2010), of Leo II from Koch et al. (2007a), and of Sextans from Lee et al. (2003). We refer to these works for further details on the photometric observations and analysis. Here we briefly mention that in the case of Carina, Fornax, Sextans and Sculptor the final photometric datasets were placed on a common V, I photometry in the UBVRI photometric system (Walker et al. 2007 for Carina; Walker et al. 2006 for Fornax; Lee et al. 2003 for Sextans; Walker et al. 2006 and Coleman, Da Costa, & Bland-Hawthorn 2005 for Sculptor). In the case of Leo II, we use the photometric dataset in the SDSS filter system, using the transformations in eq. 2 and eq. 3 derived by Koch et al. (2007a) in the g– and i–band filters. We note that in the case of Carina, Fornax and Sculptor, there is EIS photometry available to match exactly the spectroscopic targets (Carina: Koch et al. 2006; Fornax and Sculptor: Battaglia et al. 2006, 2008, and private communication), but we choose not to use these datasets since they are poorly calibrated (Koch et al. 2004a, 2004b).

The global properties of the five dSphs, sorted by decreasing absolute V-band magnitude, are listed in Table 4.2. We show in column (1) the galaxy name; in column (2) the absolute V–band magnitude adopted from Grebel, Gallagher & Harbeck (2003); in columns (3) and (4) the V– and I–band extinctions (or the SDSS g– and i–band extinctions in the case of Leo II), respectively, taken from Schlegel, Finkbeiner & Davis (1998) for Leo II and Fornax, from Mighell (1997) for Carina, from Lee

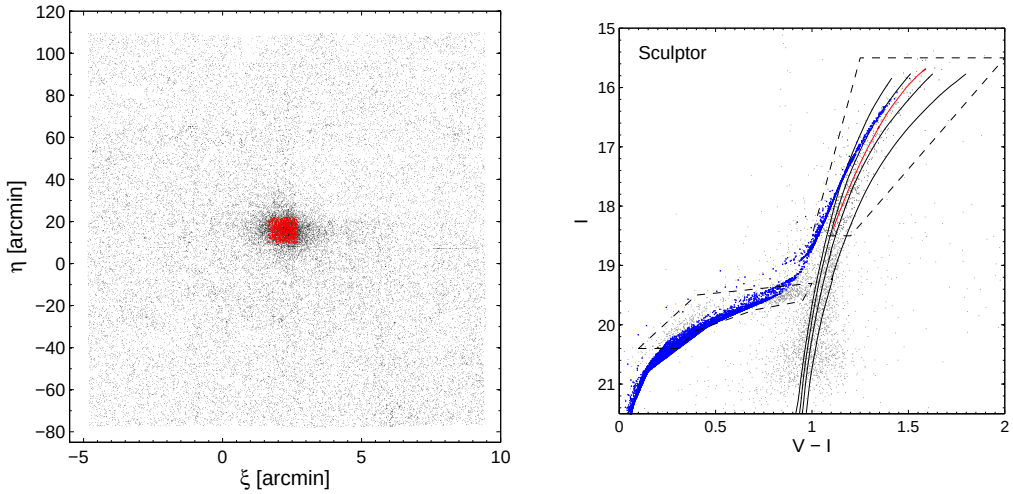

Figure 4.1: *Left panel*: Map of Sculptor, shown in black dots in standard coordinates ξ and η, along with the central region selected to derive the distance modulus, shown in red dots. The radius of the central region is approximately 8.5 arcmin, or 1.47 r_c, where r_c is the core radius of Sculptor, adopted from Irwin & Hatzidimitriou (1995). *Right panel*: Color–magnitude diagram of the central region of Sculptor, with Dartmouth isochrones of a fixed age of 12.5 Gyr overplotted as solid black lines. From left to right, the isochrones correspond to metallicities of -2.5, -2.0, -1.5 and -1.0 dex in [Fe/H]. The red line corresponds to the ridgeline, which is a second order polynomial fit to the stars inside the RGB box denoted with the black dashed lines. The blue dots correspond to the Dartmouth synthetic horizontal branch isochrone, computed for the distance modulus, reddening and the metallicity that best fit the ridgeline.

et al. (2003) for Sextans, while we derive our own values for Sculptor, as explained in the following paragraph; in column (5) the distance modulus, taken from Mighell (1997) for Carina, from Bellazzini, Gennari & Ferraro (2005) for Leo II, from Rizzi et al. (2007a) for Fornax, from Lee et al. (2003) for Sextans, while for Sculptor we derive our own distance modulus; in column (6) the tip of the RGB, taken from Mighell (199) for Carina, from Rizzi et al. (2007a) for Fornax, from Lee et al. (2003) for Sextans, from the position of the tip of the RGB in the transformed SDSS isochrones for Leo II, while for Sculptor we derive our own measurement.

For Sculptor, we derive our own distance modulus and extinction, since there is reliable photometry available down to the horizontal branch level. In order to avoid foreground contamination, we select potential Sculptor member stars by confining the selection of stars to the central region of Sculptor, as shown in the left panel of Fig. 4.1. We derive the distance modulus and the reddening using the method of the tip of the RGB (TRGB; Lee, Freedman & Madore 1993).

In the TRGB method, a 4–point Sobel filter, [-2 -1 0 1 2], is applied to the I–band luminosity

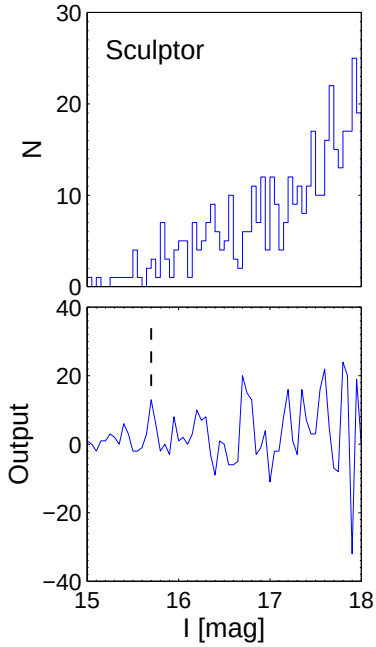

Figure 4.2: I–band luminosity function of the central region of Sculptor, upper panel, and the Sobel filter output, lower panel. The TRGB is indicated with the dashed line in the lower panel.

function, in order to detect the I–band magnitude of the TRGB, which appears as a discontinuity in the I–band luminosity function. The Sobel filter response peaks at the discontinuity and the I–band magnitude of the peak of the filter response indicates the I–band magnitude of the TRGB, as shown in Fig. 4.2. The detected TRGB magnitude equals to I_{TRGB} =15.70±0.10 mag. Assuming an absolute TRGB magnitude of $M_{I,TRGB} = -4.05 \pm 0.10$ (Da Costa & Armandroff 1990) and using the calibration provided in Lee, Freedman & Madore (1993) for the metallicity [Fe/H] versus the color of the RGB at the level of $M_I = -3.5$ mag, we derive the distance modulus and the reddening for Sculptor. This step is an iterative procedure and in practice we require that the slope of the RGB ridgeline is fitted by the Dartmouth isochrone of 12.5 Gyr when applying the derived values of the distance modulus, metallicity and reddening. In addition, we require that the Dartmouth horizontal branch isochrone of 12.5 Gyr fits the observed horizontal branch, when the derived parameters for the distance modulus, metallicity and reddening are applied to the horizontal branch isochrone. These two requirements are shown and further explained in the right panel of Fig. 4.1. The derived distance modulus is $(m-M)_0$ =19.65±0.14 mag, in agreement with the one derived by Rizzi et al. (2007b). The derived I– and V–band extinctions are listed in Table 4.2, for which we assumed the reddening law of Cardelli, Clayton & Mathis (1989).

4.3 Results

4.3.1 Color–magnitude diagrams

We show the color–magnitude diagrams (CMDs) of the five Galactic dSphs Carina, Leo II, Fornax, Sextans and Sculptor in Fig. 4.3, along with Dartmouth isochrones overplotted with a fixed age of 12.5 Gyr and metallicities ranging from -2.5 dex to 0 dex (or to -1.5 dex in the case of Leo II) with a step size of 0.5 dex (or 0.2 dex in the case of Leo II). The thick dots represent the stars in common between the photometric and spectroscopic samples. These were found by matching the spectroscopic and photometric datasets according to their coordinates. The number of stars in common is equal to 144 for Carina, 47 for Leo II, 288 for Fornax, 60 for Sextans, and 82 for Sculptor. We note that these numbers are further reduced after applying the photometric and spectroscopic metallicity cuts, as explained later on in the analysis.

4.3.2 Photometric metallicities

For the five studied Galactic dSphs, we derive their photometric metallicities using linear interpolation between Dartmouth isochrones with a fixed age of 12.5 Gyr, with a range in metallicities from -2.50 dex to 0 dex and with a step size of 0.05 dex (e. g., Lianou, Grebel & Koch 2010). We correct the magnitudes and colors of the theoretical isochrones for foreground Galactic extinction in the V–band and I–band (or the SDSS g–band and i–band in the case of Leo II) and for the distance moduli, listed in columns (3), (4) and (5) of Table 4.2, respectively. We analyse all bona–fide RGB stars that lie within 3 mag below the TRGB, listed in Table 4.2, regardless of whether they were observed spectroscopically, in order to derive the mean photometric metallicity properties and compare them with the mean spectroscopic properties. We impose a metallicity cut on the derived photometric metallicities so as to only include stars that fall within the theoretical isochrones' metallicity range used in the interpolation method, thus excluding any extrapolated values, and additionally we require the photometric metallicity uncertainties to be less than 0.2 dex, in order to be comparable with the spectroscopic metallicity uncertainties. The random uncertainties of the photometric metallicities are estimated by accounting for the photometric errors. For that purpose, each star is varied by its photometric uncertainties (both in color and magnitude) and re–fit using the same isochrone interpolation code. The $1\,\sigma$ scatter of the output random realisations is then adopted as the metallicity error for each star.

We show the derived photometric metallicity distribution functions (MDFs) with the white histograms in Fig. 4.4 for Carina, Leo II, Fornax and Sculptor, and in Fig. 4.5 for Sextans. The derived mean photometric metallicities [Fe/H]$_{phot}$ are listed in Table 4.3.

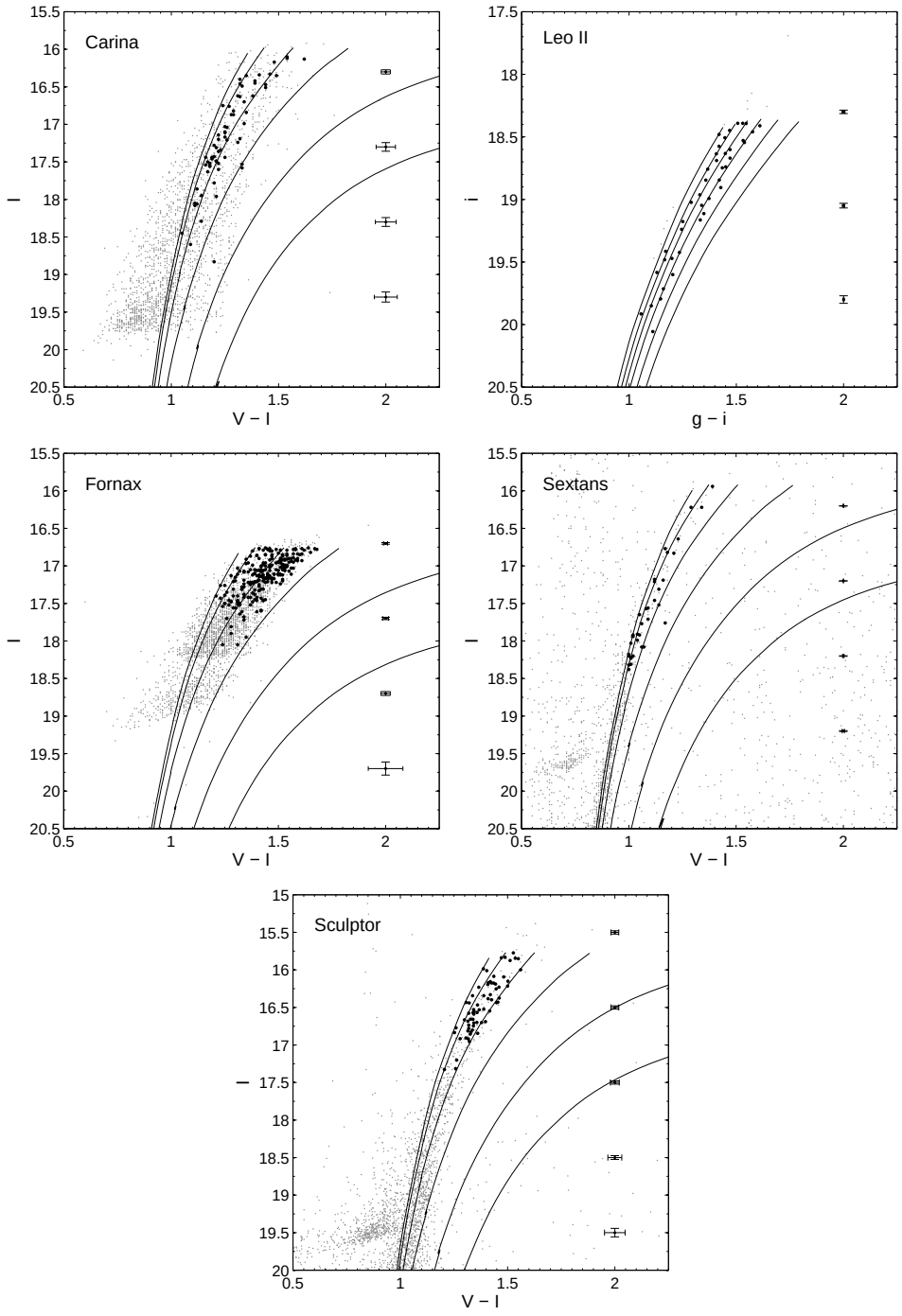

Figure 4.3: Color–magnitude diagrams of the five Galactic dSphs. Dartmouth isochrones are overplotted as solid lines, for a fixed age of 12.5 Gyr, a range in metallicities from -2.5 to 0 dex, or to -1.5 dex in the case of Leo II, and a step size of 0.5 dex, or 0.2 dex in the case of Leo II. The thick dots correspond to the stars in common to the photometric and spectroscopic sample. The error bars correspond to the photometric errors.

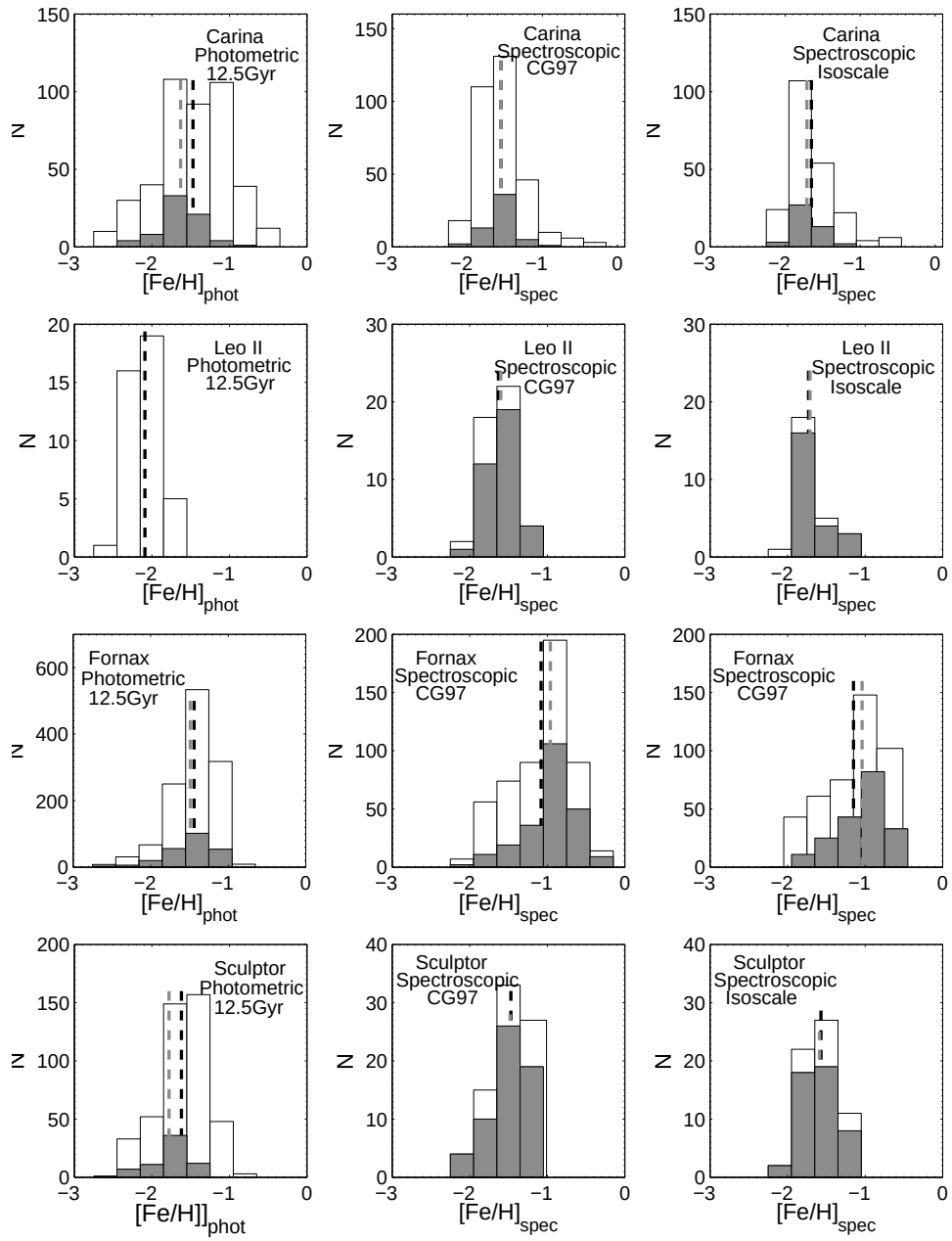

Figure 4.4: Left panels: The open histograms show the photometric metallicity distribution function of all the stars within 3 mag below the TRGB. The shaded histograms show the photometric metallicity distribution function of the stars in common to both the spectroscopic and photometric sample. Note that in the case of Leo II, the photometric sample coincides with the spectroscopic sample, thus the lack of the shaded histogram. Middle panels: The open histograms show the spectroscopic metallicity distribution functions in the CG97 scale for the full available spectroscopic sample. The shaded histograms show the spectroscopic metallicity distribution function in the CG97 for the stars in common to both the spectroscopic and photometric samples. Right panels: The open histograms show the spectroscopic metallicity distribution functions in the isoscale, while the shaded histograms show the same but for the common stars. In all cases, the black dashed line corresponds to the mean metallicity value of the full sample, while the shaded dashed line corresponds to the mean metallicity value of the common stars.

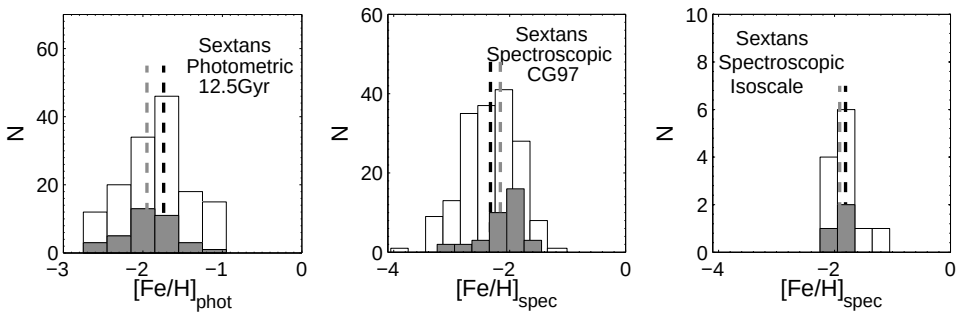

Figure 4.5: The same as in Fig.4.4 for Sextans. Note that in the isoscale metallicity distribution function of the common stars (right panel; shaded histogram), the total number of stars is three. The number of stars corresponding to the open histogram in the isoscale (right panel) is twelve.

Table 4.3: Mean metallicity properties.

Galaxy	Carina	Leo II	Fornax	Sextans	Sculptor
$[Fe/H]_{phot}$	-1.47 ± 0.45	-2.09 ± 0.20	-1.44 ± 0.29	-1.82 ± 0.40	-1.61 ± 0.31
$[Fe/H]_{CG97}$	-1.55 ± 0.29	-1.63 ± 0.23	-1.08 ± 0.40	-2.33 ± 0.46	-1.47 ± 0.26
$[Fe/H]_{isoscale}$	-1.65 ± 0.30	-1.73 ± 0.22	-1.15 ± 0.39	-1.81 ± 0.25	-1.57 ± 0.23

4.3.3 Dartmouth isochrones metallicity scale

In order to perform a direct comparison between the photometric and the spectroscopic metallicities, it is important to clarify with which metallicity scale the photometric metallicities conform. The photometric metallicities are tied to the isochrone models that are used in the interpolation method. The Dartmouth isochrones used here are not explicitly tied to any of the spectroscopic, standard abundance scales (i.e., ZW84; CG97; KI03; CBG09). Their determination is rather based on the mass fractions of the heavy elements and hydrogen in the models along with the adopted solar abundances. In that sense, the photometric metallicities based on the Dartmouth isochrones form a metallicity scale on their own. However, the Dartmouth models tend to lie much closer to either the ZW84 or to the KI03 metallicity scales (Aaron Dotter, private communication; see also Dotter et al. 2010).

In the left panel of Fig. 4.6 we plot the Galactic GC fiducials of M 15, NGC 6397, M 2 and Tuc 47, adopted from Da Costa & Armandroff (1990), along with Dartmouth isochrones for a fixed age of 12.5 Gyr. The [Fe/H] metallicities of the Galactic GC fiducials are -2.17, -1.91, -1.58 and -0.71 dex, respectively, in the ZW84 scale, and the same metallicities are chosen for the Dartmouth isochrones. In the middle and right panels we plot the analytic fits to the fiducial loci of GCs adopted from Saviane et al. (2000a), in the ZW84 and CG97 metallicity scales, respectively. The correspondence between the Dartmouth isochrones and the GC fiducials in the ZW84 scale is better than the one in the CG97 scale, but in all three cases the match is far from perfect.

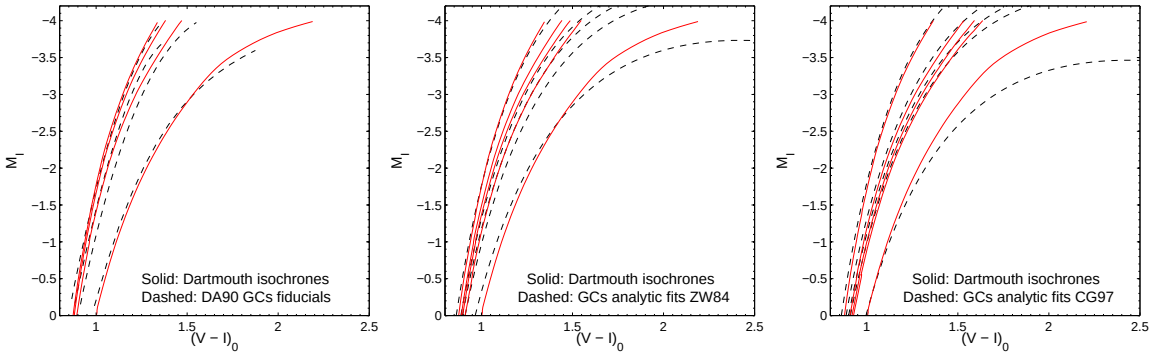

Figure 4.6: Left panel: Galactic GC fiducials from Da Costa & Armandroff (1990) shown with the black dashed lines, along with Dartmouth isochrones shown with the red solid lines. From left to right, the Galactic GC fiducials correspond to M 15, NGC 6397, M 2 and Tuc 47, where each GC has [Fe/H] equal to -2.17, -1.91, -1.58 and -0.71, respectively, in the ZW84 scale. The isochrones correspond to an age of 12.5 Gyr and have the same metallicities as the Galactic GCs, from left to right. Middle panel: Analytic functions of Galactic GCs fiducial loci from Saviane et al. (2000a) in the ZW84, black dashed lines, along with Dartmouth isochrones of 12.5 Gyr, red solid lines. The metallicities correspond to -2.11, -1.67, -1.53, -1.33 and -0.71 from left to right, respectively. Right panel: The same as in the middle panel but for the CG97 metallicity scale. The metallicities correspond to -1.99, -1.37, -1.23, -1.15 and -0.7 from left to right, respectively.

Therefore, based on the fact that the Dartmouth isochrones form a metallicity scale of their own, we transform the spectroscopic metallicities of all five dSphs to the metallicity scale defined by the Dartmouth isochrones. The metallicity scale defined by the Dartmouth isochrones is further simply called "isoscale". In order to define the transformation between the CG97 metallicity scale and the isoscale, we use the metallicities of those Galactic GCs in Dotter et al. (2010; their Table 2), derived using isochrone fitting, that also have metallicities in the CG97 scale as derived in R97 (their Table 2). The calibration of the metallicities from the CG97 to the isoscale reads as follows:

$$[\mathrm{Fe/H}]_{\mathrm{iso}} = 1.35_{\pm 0.04}[\mathrm{Fe/H}]_{\mathrm{CG97}} + 0.27_{\pm 0.06}, \tag{4.1}$$

and holds within the metallicity range of $-2.02 \leq [\mathrm{Fe/H}]_{CG97} \leq -0.5$ (dex), as imposed by the availability of GCs with [Fe/H] in the CG97 scale that also have [Fe/H] based on the Dartmouth isochrone fitting. The calibration is plotted in Fig. 4.7. The reversed metallicity calibration from the isoscale to the CG97 metallicity scale reads as follows:

$$[\mathrm{Fe/H}]_{\mathrm{CG97}} = 0.70_{\pm 0.02}[\mathrm{Fe/H}]_{\mathrm{iso}} - 0.26_{\pm 0.04}, \tag{4.2}$$

and holds within the metallicity range of $-2.40 \leq [\mathrm{Fe/H}]_{iso} \leq -0.5$ (dex), which is defined by the

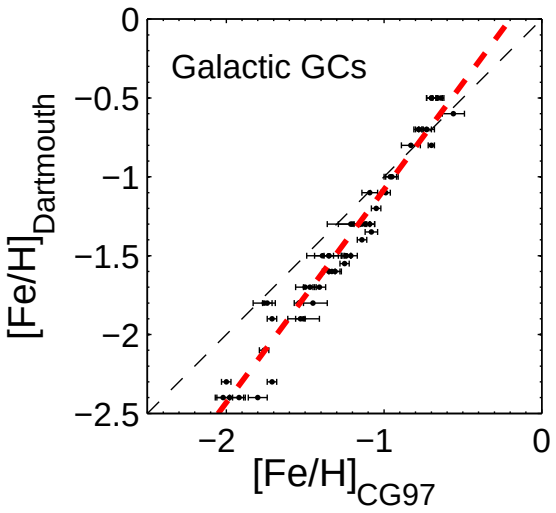

Figure 4.7: Calibration from the CG97 scale to the Dartmouth isochrone metallicity scale, simply called "isoscale". The red solid line corresponds to the error–weighted linear least squares fit to the data. The black dashed line corresponds to unity.

available metallicities of the GCs based on the isochrone fitting.

4.3.4 Spectroscopic metallicities

We show in Fig. 4.4 with the open histograms the spectroscopic MDFs in the CG97 metallicity scale and the isoscale, in the middle and right panels, respectively, for Carina, Leo II, Fornax, and Sculptor, and in Fig. 4.5 for Sextans. These were derived using the whole available spectroscopic sample with the requirement that the spectroscopic metallicities are within the range of $-2 \leq$[Fe/H]$_{CG97} \leq -0.2$ (dex) for the CG97 scale (Cole et al. 2004), apart from Sextans, and $-2.02 \leq$[Fe/H]$_{CG97} \leq -0.5$ (dex) for the isoscale. For Sextans in the CG97 metallicity scale, we adopt the metallicity range of $-4 \leq$[Fe/H]$_{CG97} \leq -0.5$ (dex) (Battaglia et al. 2010), where a revised calibration of the Ca T has been applied between the [Fe/H] and the sum of the Ca T lines, Σ W, in the CG97 scale. Starkenburg et al. (2010) perform a synthetic spectral analysis of the Ca T lines down to -4 dex in [Fe/H] and they find that a simple linear relation of [Fe/H] as a function of Σ W does not hold for metallicities lower than -2.5 dex and therefore they provide a revised calibration. For the remaining dSphs except from Sextans, the linear calibration between [Fe/H] and W′(or Σ W) has been applied, which is valid for metallicities in the range from $-2 \leq$[Fe/H]$_{CG97} \leq -0.2$ (dex) for the CG97 scale (Cole et al. 2004). The mean spectroscopic metallicities are listed in Table 4.3 for both the CG97 scale and the isoscale.

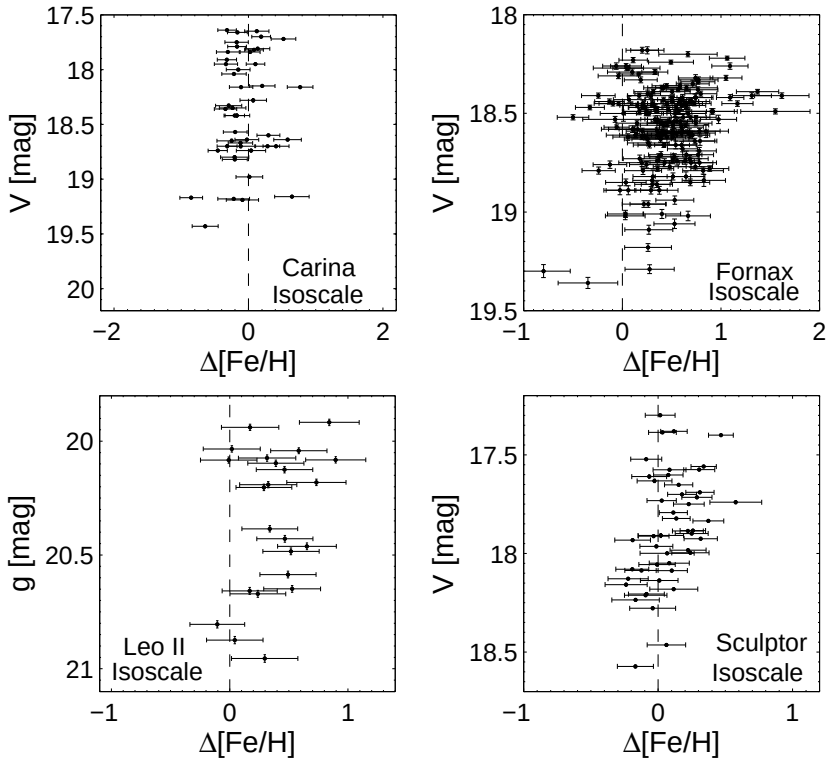

Figure 4.8: V–band magnitude versus the difference in spectroscopic minus the photometric metallicities in the isoscale for Carina, Leo II, Fornax and Sculptor.

4.3.5 Photometric and spectroscopic metallicities of the common stars

The photometric and spectroscopic MDFs for those stars with both photometric and spectroscopic measurements are shown as the shaded histograms in Fig. 4.4 for Carina, Leo II, Fornax and Sculptor, and in Fig. 4.5 for Sextans. In order to construct the photometric MDFs of the common stars, only those stars within the photometric metallicity range of $-2.5 <$ [Fe/H]$_{photometric} \leq 0$ (dex) and with an error of less than 0.2 dex are retained, while in the spectroscopic MDFs of the common stars in addition to the photometric metallicity cuts we impose the spectroscopic metallicity cuts as described in the previous paragraph. The number of the common stars in the CG97 scale and the isoscale are listed in Table 4.4, except for Sextans. As shown in Fig. 4.5, Sextans only has three stars in common between the photometric metallicities and the spectroscopic ones transformed in the isoscale. Thus we exclude Sextans from any further analysis regarding the common stars.

The differences of the spectroscopic minus the photometric metallicities versus the V–band magnitudes (or g–band magnitude in the case of Leo II) are shown in Fig. 4.8 for Carina, Leo II, Fornax, and Sculptor in the isoscale. There is a slight trend of the metallicity differences to become negative as the

V–band magnitude becomes fainter, and to become positive as the V–band magnitude becomes brighter. We note that the isochrones tend to cluster towards the metal–poor end so that an unambiguous assignment of metallicities becomes difficult. This is due to the fact that the isochrone resolution towards bluer colors and fainter magnitudes becomes narrower, thus demonstrating the inability of the photometric metallicities to reproduce the spectroscopic metal poor tail of the MDF (cf. Koch et al. 2008b). On the other hand, the Ca T method has its largest sensitivity at the metal–poor end.

4.4 Discussion

In a stellar system with a complex SFH where both old and intermediate age stellar populations are present, its RGB contains stars belonging to the full age range of approximately 1.5 Gyr and higher (Salaris, Cassisi & Weiss 2002). Thus the assumption of a single old age for the stellar populations and therefore for the isochrones used in the interpolation holds only in the case of a negligible intermediate age population. In dSphs, the initial star formation may have lasted as long as 3 Gyr or even longer (Marcolini et al. 2008; Ikuta & Arimoto 2002), thus leading to large metallicity dispersions. In the case of dSphs dominated by old populations with ages larger than 10 Gyr, this extended star formation does not substantially affect their photometric metallicities and can lead to individual star photometric metallicity differences of approximately 0.1 dex, as demonstrated in Lianou, Grebel & Koch (2010) using M 81 group dSphs as a test case. Here we explore the effects of the presence of an intermediate age population on deriving photometric metallicities by comparing to metallicities derived through the Ca T method.

4.4.1 Mean metallicity properties

In Table 4.3 we list the mean photometric and spectroscopic metallicities for the five studied dSphs. For the spectroscopic metallicities we list both the mean metallicities in the CG97 scale and the isoscale. These mean photometric and spectroscopic metallicities were derived using the open histograms shown in Fig. 4.4 and Fig. 4.5, therefore they do not correspond to the common stars.

In the case of Sculptor and Sextans, the difference between their mean photometric and mean spectroscopic metallicities in the isoscale is 0.04 dex and 0.01 dex, respectively. Sculptor and Sextans are dominated by old populations, with their fraction reaching to 95% for Sculptor and 100% for Sextans (Dolphin et al. 2005). It is therefore encouraging that the photometric and spectroscopic metallicities in the isoscale are in quite good agreement, with the photometric mean metallicity being slightly metal–rich than the spectroscopic one. The same holds for the mean photometric metallicity of Sculptor as compared to the spectroscopic metallicity in the CG97 scale, with a difference from the mean

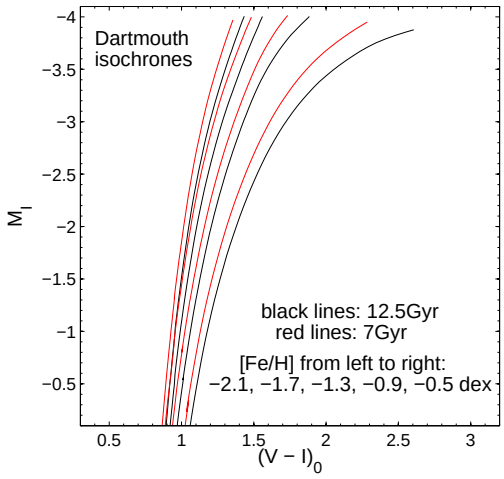

Figure 4.9: Dartmouth isochrones for an age of 12.5 Gyr (black) and 7 Gyr (red), and for a range in metallicities from -2.1 to -0.5 dex. The intermediate age isochrone lies bluewards to the old age isochrone, at a fixed metallicity. Note that for a constant age and varying the [Fe/H] the slope of the RGB changes, while for a varying age and a constant [Fe/H] the slope of the RGB remains unchanged.

photometric metallicity of 0.14 dex. This is not the case for Sextans, where the difference of the mean spectroscopic metallicity in the CG97 scale from the mean photometric metallicity amounts to 0.51 dex, based on 173 stars with spectroscopic metallicities in the CG97 scale (Battaglia et al. 2010) and shown with the open histogram in the middle panel of Fig. 4.5. This mismatch between the two mean metallicity values for Sextans can be explained if one considers that the individual spectroscopic metallicities in the CG97 scale include metallicity values as metal–poor as -4 dex (Battaglia et al. 2010), while the individual photometric metallicities can reach up to -2.5 dex, which is the most metal–poor value of metallicity provided with the Dartmouth isochrones. Therefore, the different selection criteria in terms of metallicity ranges used for the metallicities in the CG97 scale and the photometric metallicities can account for this large difference, which further suggests that such a comparison for Sextans should not be made.

Carina, Leo II and Fornax have complex star formation and chemical enrichment histories including substantial intermediate–age populations, thus we do not expect a priori that there will be an agreement between the mean photometric and spectroscopic metallicities. The existence of a mixed–age population is expected to lead to an overestimate of the photometric metallicities towards the metal–poor part. At fixed metallicities, an intermediate age population would lie bluewards to the old population. Thus, intermediate age populations would be assigned more metal–poor metallicities than their true value, if they were erroneously assumed to belong to an old population. This photometric metal–poor bias is demonstrated in Fig. 4.9, where isochrones of two fixed ages of 12.5 Gyr and 7 Gyr are overplotted with

the same ranges in metallicities from -2 to -0.5 dex, as detailed in the Figure. Carina, Leo II, and Fornax are, in different amounts, intermediate–age dominated populations. The difference of their mean photometric from their mean spectroscopic metallicity is indeed non–zero, with the tendency of the mean photometric metallicities to be more metal–poor than the spectroscopic ones, apart from Carina which seems to have a photometric mean metallicity more metal–rich than the spectroscopic one. The maximum difference in the isoscale and the CG97 scale occurs for Leo II which amounts to 0.36 dex and 0.46 dex, respectively.

4.4.2 Star–by–star metallicity differences

For those stars with both spectroscopic and photometric measurements, we show the photometric versus the spectroscopic metallicities in the upper panels of Fig. 4.10, separately in the CG97 scale and the isoscale for Carina, Leo II, Fornax and Sculptor. The lower panels each show the residuals of the comparison and in all cases, the Δ [Fe/H] corresponds to the spectroscopic metallicities minus the photometric metallicities.

A difference Δ[Fe/H] with a positive sign means that the spectroscopic metallicities are more metal–rich than the photometric metallicities. The photometric systematic uncertainty that can contribute to a positive difference Δ[Fe/H] is the photometric metal–poor bias due to the presence of an intermediate age population. This metal–poor bias has been estimated to be up to 0.4 dex, in the case of deriving photometric metallicities assuming an age of 12.5 Gyr for the underlying population minus the photometric metallicities assuming an age of 8.5 Gyr (Lianou, Grebel & Koch 2010), with the maximum difference occurring in the metal–poor end.

Possible sources of uncertainties that can contribute to the photometric metallicities are the distance modulus and reddening. In the case of Sculptor, a variation of the distance modulus by ± 0.14 mag leads to a relative difference of photometric metallicities of 10%, where the variation of the distance modulus $+0.14$ mag leads towards more metal poor metallicities. A variation of the reddening by ± 0.02 mag leads to a relative difference of the photometric metallicities of 10%, where an increase in the reddening of $+0.02$ mag leads again towards more metal poor metallicities.

Another source of uncertainty comes from the assumption of a scaled–solar composition of the [α/Fe] chosen for the Dartmouth isochrones. Again, choosing Sculptor as a test case, we choose an [α/Fe] equal to $+0.2$ dex, constant through the whole range of the photometric metallicities. This choice leads to more metal poor photometric metallicities, by 6% for the relative differences, and makes the mean photometric metallicity metal–poor by 0.1 dex for the mean metallicity (see also Kalirai et al. 2006). Individual α–element ratios for Sculptor indicate that the [α/Fe] has an average value of approximately 0 dex (Venn et al. 2004; their Figure 2 and Figure 7), across the range of metallicities

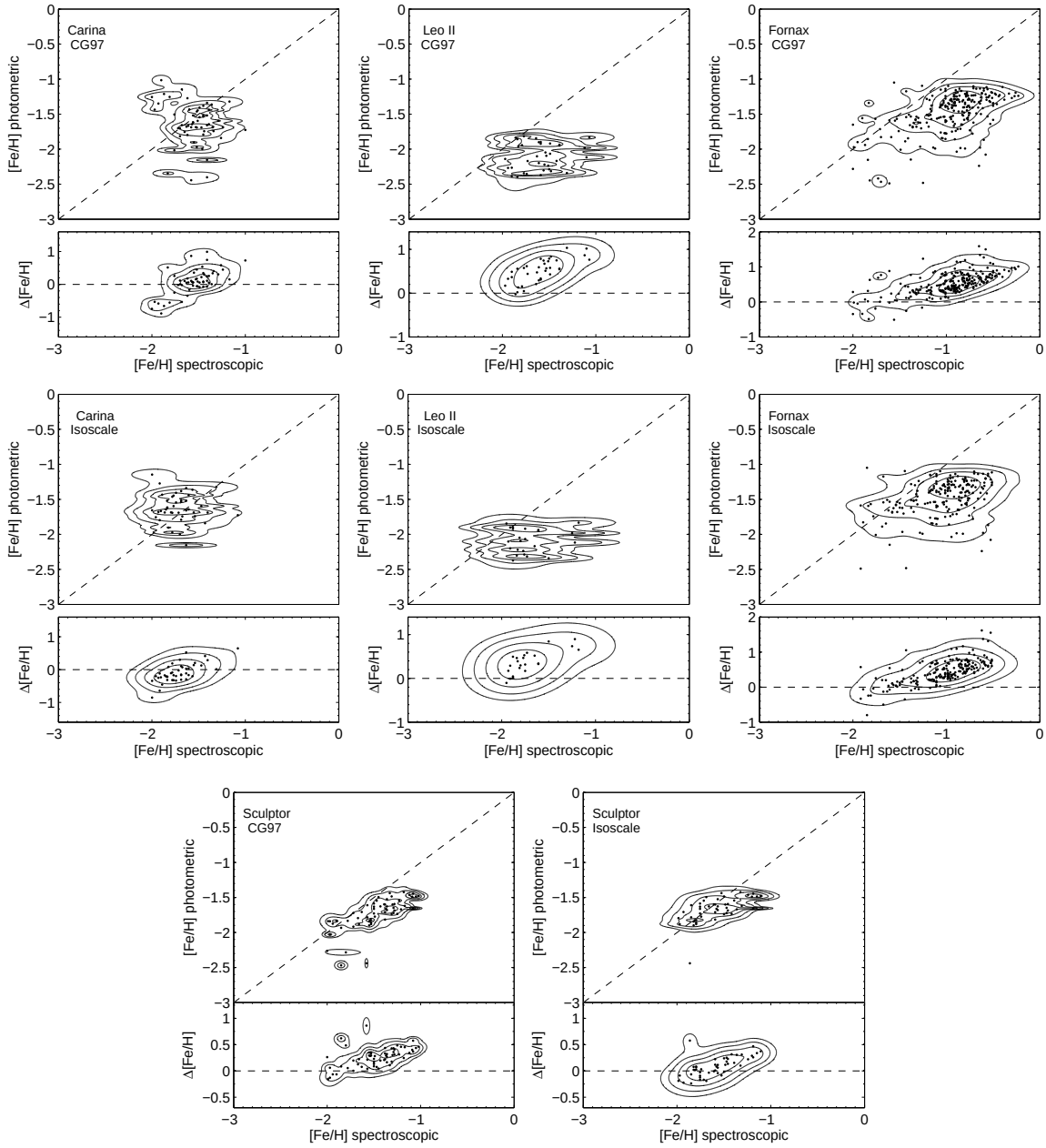

Figure 4.10: The first two rows show, from left to right, the photometric versus the spectroscopic metallicities (upper panels), as well as the residuals of the comparison (lower panels), in the CG97 scale and the isoscale for Carina, Leo II and Fornax. The last row shows the same for Sculptor. The contours correspond to the photometric and spectroscopic uncertainties within 0.5 to 2.5 σ.

we consider here for the isoscale of $-2.02 \leq$[Fe/H]$_{CG97} \leq -0.5$ (dex). For the dSphs that have more complex SFHs, the choice of an [α/Fe] of zero is justified by the range of ages of the stars present, where their [α/Fe] tends to solar values, as discussed in Koch et al. (2008b). Furthermore, for Carina and for the metallicity ranges we consider here, the [α/Fe] has an average value of approximately 0 dex (Koch et al. 2008a; their Figure 2, left bottom panel), and the same stands for Fornax (Venn et al. 2004; their Figure 2).

Sculptor

In the case of a purely old population as is Sculptor, one should expect the photometric metallicities to match the spectroscopic metallicities once everything has been placed on the same metallicity scale. This is not what is observed in Fig. 4.10 for Sculptor, where there is an excess of stars with positive Δ[Fe/H] which increases towards the spectroscopic metal–rich end. The median value of the difference Δ[Fe/H] is equal to 0.08 dex with a full range of 0.82 dex. The minimum Δ[Fe/H] is equal to -0.24 dex and the maximum is equal to 0.58 dex. The slope of the difference in metallicities Δ[Fe/H] versus the spectroscopic metallicity is listed in Table 4.4.

Sculptor is an old–age dominated system, with 95% of its stars having ages larger than 10 Gyr. The presence of old AGB stars may contribute to the Δ[Fe/H] becoming positive, due to the photometric metal–poor bias, but the overall mean metallicity properties are unaffected. Indeed, the use of isochrones with a fixed age of 12.5 Gyr that include only the AGB phase result in a mean metallicity of -1.20$\pm$0.27 dex that is comparable with the mean metallicity derived using only the RGB phase of -1.24$\pm$0.26 dex, while the mixture of populations assuming a 22% of AGB stars and a 78% of RGB stars result to a mean metallicity of -1.24$\pm$0.39 dex which is comparable to the mean metallicity derived when including only the RGB phase (Lianou, Grebel & Koch 2010). The errors quoted refer to the 1 σ spread, while these calculations were performed using as a test case the colors and magnitudes of the resolved stars of KDG 61 dSph, which belongs to the M 81 group.

Hurley–Keller, Mateo & Grebel (1999) discuss that Sculptor may contain two old stellar populations, based on its horizontal branch morphology, while Harbeck et al. (2001) find a population gradient and Tolstoy et al. (2004) two kinematically distinct ancient components. Therefore, if we use an isochrone of 10 Gyr to derive the photometric metallicities of Sculptor, then the new metallicity becomes more metal–rich by 0.13 dex. The median of the differences of the photometric metallicities based on a 12.5 Gyr isochrone minus the ones based on the 10 Gyr isochrone is equal to -0.12 dex, with a full range of 0.16 dex. Thus, the potential existence of two old populations in Sculptor does not lead to the observed differences between the spectroscopic and photometric metallicities.

If we use the high–resolution spectroscopic metallicities from Battaglia et al. (2008), instead of the

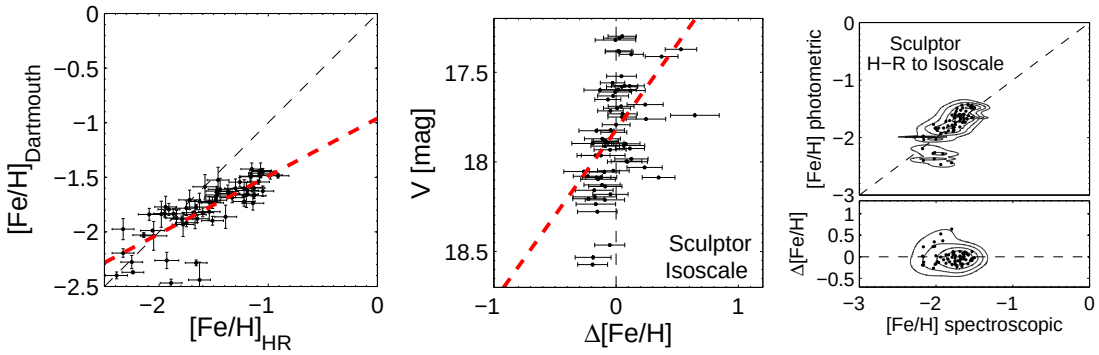

Figure 4.11: Left: The calibration from the high–resolution spectroscopic measurements to the isoscale for Sculptor. Middle: V–band magnitude as a function of the Δ[Fe/H] in the isoscale for Sculptor. The red dashed line corresponds to the error–weighted linear least squares fit to the data. Right: The Δ[Fe/H] as a function of the high–resolution spectroscopic metallicity placed on the isoscale.

Ca T based spectroscopic metallicities, then the metallicity differences become smaller. For that reason, we place the high–resolution metallicities on the metallicity scale defined by the Dartmouth isochrones. To do so, we use the stars in common that have photometric metallicities and high–resolution spectroscopic metallicities, in order to derive their transformation from the high–resolution metallicity scale to the Dartmouth isochrone metallicity scale. Given that Sculptor is an old–age dominated system, we do not expect to have any age effects on the metallicities, thus we can perform this transformation for individual stars in the same way as in Sec. 4.3.3. The derived calibration is shown in the left panel of Fig. 4.11. In the same Fig. 4.11 we show the Δ[Fe/H], in the sense of high–resolution spectroscopic metallicities minus photometric metallicities, versus the V–band magnitude, middle panel, and versus the high–resolution spectroscopic metallicities, right panel. The agreement in metallicities is better in this case. The median of the relative differences Δ[Fe/H]/[Fe/H]$_{spec}$ in this case is approximately 7%. Even though there is a better match between the high–resolution spectroscopic metallicities and the photometric metallicities, the question still remains regarding the mismatch of the Ca T based spectroscopic metallicities and the photometric metallicities.

Carina, Leo II and Fornax

Carina, Leo II and Fornax have a significant fraction of intermediate age stars that lead to an age–metallicity degeneracy in the RGB, as shown in Fig. 10 of Koch et al. (2006) for Carina, in Fig. 8 of Koch et al. (2007a) for Leo II, and in Fig. 22 of Battaglia et al. (2006) for Fornax. This complex SFH will affect their photometric metallicities in the sense of the photometric metal–poor bias. In all cases, just as with Sculptor, Fig. 4.10 shows a trend of increasing positive Δ [Fe/H] differences with increasing [Fe/H]. The positive differences of metallicities are attributed to the presence of intermediate age stars,

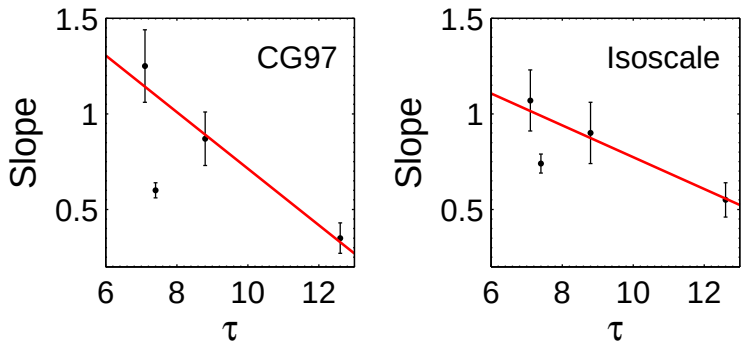

Figure 4.12: Slopes of the error–weighted linear least squares fit to the datapoints of the lower panels of Fig. 4.10 as a function of the mass–weighted mean age for Carina, Leo II, Fornax and Sculptor. The red solid line corresponds to an error-weighted linear least squares fit to the data. The error bars correspond to the error of the coefficients of the fit to the datapoints of Fig. 4.10.

which have bluer colors than old stars at a given metallicity, as demonstrated in Fig. 4.9. The negative differences can be attributed to the poorer resolution of the isochrones towards the metal–poor end. The median of the Δ[Fe/H] is -0.17 dex, 0.34 dex and 0.42 dex for Carina, Leo II and Fornax, respectively, while the full range of the Δ[Fe/H] is 1.5 dex, 1 dex and 2.42 dex respectively. The values quoted refer to the isoscale.

An error-weighted linear least squares fit to the datapoints of the lower panels of Fig. 4.10, which show the Δ[Fe/H] as a function of the spectroscopic metallicities, results in the slopes listed in Table 4.4. In the case of a purely old population, one would expect that the slope would be zero, as a result of ideally zero differences between the photometric and spectroscopic metallicities. The non–zero slopes of the Δ[Fe/H] as a function of the [Fe/H]$_{spec}$ are shown in Fig. 4.12 which are now plotted against the mass–weighted mean age, τ, of each dSph, adopted from Orban et al. (2008); the values of τ are listed in Table 4.4. It seems that increasing the mass–weighted mean age leads to an increase of the slope (of the Δ[Fe/H] as a function of the [Fe/H]$_{spec}$). This is demonstrated by the red solid line which is an error–weighted linear least squares fit to the data points in Fig. 4.12. The error bars correspond to the errors of the coefficients of the fit to the datapoints of the lower panels of Fig. 4.10.

4.4.3 Application of the photometric method

The presence of an intermediate age population in a dSph leads to a metal–poor bias of the photometric metallicities, in the sense that the photometric metallicities are assigned a more metal–poor value than their true one. In the case of the Galactic dSphs studied here, which all have a pronounced or even dominant intermediate age population, the individual stellar differences of the spectroscopic minus the

Table 4.4: Slopes of the Δ[Fe/H] versus the spectroscopic [Fe/H].

Galaxy	Carina	Leo II	Fornax	Sculptor
τ (Gyr)	7.1	8.8	7.4	12.6
$N_*, CG97$	57	41	235	59
$N_*, isoscale$	43	23	194	47
$CG97_{slope}$	1.25 ± 0.19	0.87 ± 0.14	0.60 ± 0.04	0.35 ± 0.08
$Isoscale_{slope}$	1.07 ± 0.16	0.90 ± 0.16	0.74 ± 0.05	0.55 ± 0.09

photometric metallicities can reach up to approximately 2.4 dex, in the case of Fornax which has the most extended star formation and chemical evolution history, while the mean metallicity properties remain consistent within the uncertainties of the methods. In practice, the photometric metallicities become more metal–poor as compared to the Ca T spectroscopic metallicities. In dSphs where the fraction of the intermediate age population is small, the effect on the photometric metallicities is negligible. In the case of Sculptor, there is a scatter between the photometrically and spectroscopically Ca T based metallicities, that lead to individual star differences of the metallicities between these two methods that can reach up to approximately 0.8 dex.

In more distant dSphs where the use of the Ca T method to derive spectroscopic metallicities is not available due to the faintness of the stars to be targeted, one has to rely on the photometric method in order to have an estimate of their metallicity. The mean metallicities derived from the photometric method in the case of a purely old dSph are biased towards the metal–poor end by approximately 0.04 dex. Therefore one can safely use the photometric method in order to derive the mean metallicity properties of a dSph, especially in the case when no other means of deriving metallicities is available.

Given the fraction of the intermediate age population in a dSph, one can derive an estimate of how much offset the photometric metallicities may be as compared to the spectroscopic metallicities. In more distant dSphs, the ability of deriving accurate SFHs is hampered by the same fact examined here of the age–metallicity degeneracy (Gallart, Zoccali & Aparicio 2005) on the RGB. Therefore, one has to rely on the presence of luminous AGB stars as a probe of the presence of intermediate age populations. In a study of metallicity distribution functions of nine dSphs in the M81 group of galaxies (Lianou, Grebel & Koch 2010), there are luminous AGB stars detected in all of them, but with a small fraction. If we assume the small fraction of luminous AGB stars to be indicative of a small fraction of intermediate age stars present in these dwarf galaxies, then the photometric metallicities would compare with the potential spectroscopic metallicities in the same way as in the case of Sculptor. Therefore, the presence of intermediate age populations as probed by the luminous AGB stars should have a negligible effect on the photometrically derived metallicities.

4.5 Conclusions

We use the resolved RGBs of five Galactic dSphs, namely Carina, Leo II, Fornax, Sextans and Sculptor in order to derive their photometric metallicities using a linear interpolation method assuming a constant old age for the theoretical isochrones and a wide range in metallicities. We compare the photometric metallicities with the spectroscopic metallicities from the literature in several ways in order to examine the effect of the presence of intermediate age stellar populations on the derivation of the photometric metallicities. The comparison between the photometric and spectroscopic metallicities is performed both in the CG97 metallicity scale and in the metallicity scale defined by the Dartmouth isochrones.

The comparison of the *mean* photometric metallicity properties with the *mean* spectroscopic ones shows that these are in as much good agreement as permitted given the presence of a significant intermediate–age component. For those stars that are in common in the spectroscopic and photometric samples, the differences between their individual star metallicities derived from both methods show a large scatter towards the metal–rich spectroscopic end.

Given the fraction of the intermediate–age population present, the differences of the metallicities between the two methods increase as a function of decreasing mass–weighted mean age. Thus, one can estimate the expected differences of metallicities between the two methods, once there is an estimate of the intermediate–age population present. The luminous AGB stars can be used as an indication of the presence of the intermediate age stars.

Chapter 5

Summary and Outlook

In this Thesis, we focus on the effect of the M 81 group of galaxies environment on the formation and evolution of its dwarf galaxy population. The highly interacting environment of the M 81 group offers a unique opportunity to study dwarf galaxies that may be in formation. Such dwarf galaxies forming in interactions are called tidal dwarf galaxies. In the M 81 group potential young tidal dwarf galaxies were identified by examining their gas phase metallicities and their stellar population content in comparison to the M 81 galaxy. We searched for old tidal dwarf galaxies in the M 81 group using the Tully–Fisher relation and the distinguishing property of the tidal dwarf galaxies to be dark matter free due to their formation mechanism. No potential old tidal dwarf galaxy candidates were identified.

Furthermore, we examine the stellar populations of the early–type dwarf galaxies of the M 81 group using Hubble Space Telescope archival observations. In particular, we use the stars in the red giant branch phase in order to derive their photometric metallicity distribution functions and to examine the potential presence of metallicity gradients. We find that the studied dwarf spheroidals within the highly interacting environment of the M 81 group show similar mean metallicity and metallicity gradient properties as the Local Group dwarf spheroidals. In two very different environments, the dwarf spheroidals show the same diverse properties which indicates that at least these properties are influenced more by internal processes than by external effects. Furthermore, the intermediate–age stars in the early–type dwarfs, probed by the luminous asymptotic giant branch stars, are not significant in number. Considering the fraction of the luminous asymptotic giant branch stars as a function of their deprojected distance from the M81 galaxy, for the sample considered in this work, there is not any trend observed. This would imply that the ability of the studied dwarfs to form stars in this age range may not be a function of their environment, although one should keep in mind that their deprojected distances only show their current location within the group while their actual orbits remain unknown. It would be thus very interesting to examine the luminous asymptotic giant branch stars of a larger sample of dwarf galaxies

as a function of their current location within the M 81 group. Furthermore, it would be interesting to consider different environments and in addition to compare the findings with theoretical modelling. Future studies concerning the star formation and chemical evolution histories of galaxies in nearby groups could lead to an improved understanding of the processes that are connected with the environment a galaxy lives in and of those processes that are internal to galaxies.

The method of deriving photometric metallicities may be affected by the presence of intermediate–age populations. Therefore, we evaluated this method for different cases ranging from dwarf galaxies dominated by old populations to dwarfs with a significant fraction of intermediate–age populations. For that purpose, we compare the photometrically derived metallicities with the spectroscopically derived ones in five Galactic dwarf spheroidals that show different degrees of complexity in their star formation histories. The mean metallicities derived by the two methods are in very good agreement for those dwarf spheroidals that are dominated by old populations, while the agreement is good in the case of dwarf spheroidals that show a complex star formation history. There is the tendency of the mean photometric metallicity to be lower than the mean spectroscopic metallicity, in the case of the presence of intermediate–age population, and the more extended the star formation is the larger the discrepancy becomes. The same stands when comparing the photometric metallicities of individual stars with their spectroscopic metallicities. Therefore, an estimate of the intermediate–age stars present is important when one uses the photometric method of deriving metallicities. In the case of the M 81 group dwarf spheroidals, the fraction of the intermediate–age stars, probed by the luminous asymptotic giant branch stars, is small, therefore the photometric results are expected to be in quite good agreement with potential future spectroscopic analyses. To this end, it is important to calibrate the number of intermediate–age stars, which can in principle be done via the number of their luminous asymptotic giant branch stars.

Acknowledgements

Heidelberg has offered to me one of the most wonderful experiences so far. I would best describe my staying in Heidelberg like a punch in the stomach. Though strong the punch, the stomach still remains.

I would like to thank my supervisor Eva K. Grebel for her guidance and continuous support. I have appreciated her professional behaviour and scientific ethics that make me feel very happy to have been her student. I would like to also thank her for giving me the chance to work with people that have proven to be of high quality. Therefore, I am grateful that one of the kindest persons, Andreas Koch, has crossed my path. I would like to thank him for his support, the programming tips, the excellent communication and collaboration. I have appreciated the support and discussions with my co–advisors Thorsten Lisker and Rainer Spurzem, both of whom I thank. I am grateful for the patience of my thesis referee Norbert Christlieb.

I would like to acknowledge and thank the HGSFP for their support during these three and a half years, and especially Prof. Klevansky and Mrs. Heinzelmann. I have enjoyed being a member of IMPRS for Astronomy and Cosmic Physics and many thanks go to Dr. Christian Fendt, as well as to all my IMPRS co–fellows for the great time we have spent during various IMPRS events.

Since the beginning of my Ph D, I have appreciated discussions with Aurelie Lecureur, Elena Sabbi, and Matthias Frank, as well as Arnaud Cassan, Jose Fiestas, Alexander Hansson, Shoko Jin, Katrin Jordi, Stefan Lieder, Sarah Martell, Hagen Meyer, Christoph Olczak, Xiaoying Pang, Stefano Pasetto, Sanjaya Paudel, Justus Schneider. I am grateful to Andreas Koch and Jonathan Downing for a careful reading of this thesis, as well as Andreas Ernst for a careful proof–reading and the German translation of the abstract. My life in Heidelberg would have been boring without my friends Angelos, Anna, Cedric, Christina, Christian, Denis, Ghazal, Ioanna, Marios, Octavian, Vassiliki, and Wendy, who filled it up with great memories.

Saving the best for last, my mother and father, and my brother have always kept on encouraging me and supporting me through all these years. I especially thank my mother for her patience and trust. Two happy thoughts kept me smiling all along my PhD life： Tonia and Maria, my beautiful nieces!

Bibliography

[1] Aaronson, M., Huchra, J. & Mould, J. 1979, ApJ, 229, 1

[2] Aaronson, M. & Mould, J. 1985, ApJ, 290, 191

[3] Alonso-Garcia, J., Mateo, M. & Aparicio, A. 2006, PASP, 118,580

[4] Aparicio, A. 2002, ASPC, 274, 429

[5] Aparicio, A. & Gallart, C. 2004, AJ, 128, 1465

[6] Armandroff, T. E. & Da Costa, G. S. 1991, AJ, 101, 1329

[7] Armandroff, T. E., Da Costa, G. S., Caldwell, N. & Seitzer, P. 1993, AJ, 106, 986

[8] Appleton, P. N., Davies, R. D. & Stephenson, R. J. 1981, MNRAS, 195, 327

[9] Battaglia, G., Irwin, M., Tolstoy, Hill, V., Helmi, A., Letarte, B. & Jablonka, P. 2008, MNRAS, 383, 183

[10] Battaglia, G., Tolstoy, E., Helmi, A., Irwin, M. J., Letarte, B., Jablonka, P., Hill, V., Venn, K. A., Shetrone, M. D., Arimoto, N., Primas, F., Kaufer, A., Francois, P., Szeifert, T., Abel, T. & Sadakane, K. 2006, A&A, 459, 423

[11] Battaglia, G., Tolstoy, E., Helmi, A., Irwin, M., Parisi, P., Hill, V. & Jablonka, P. 2010, MNRAS, in press (arXiv:1009.4857v2)

[12] Battinelli, P. & Demers, S. 2004a, A&A, 418, 33

[13] Battinelli, P. & Demers, S. 2004b, A&A, 417, 479

[14] Begum, A., Chengalur, J. N., Karachentsev, I. D., Kaisin, S. S. & Sharina, M. E. 2006, MNRAS, 365, 1220

[15] Bellazzini, M., Gennari, N. & Ferraro, F. R. 2005, MNRAS, 360, 185

[16] Besla, G., Kallivayalil, N. & Hernquist, L. 2010, ApJ, 721L, 97

[17] Boselli, A. & Gavazzi, G. 2006, PASP, 118, 517

[18] Bosler, T. L., Smecker–Hane, T. A. & Stetson, P. B. 2007, MNRAS, 378, 318

[19] Bouchard, A., Carignan, C. & Mashchenko, S. 2003, AJ, 126, 1295

[20] Bournaud, F. 2010, AdAst, 2010E, 1

[21] Bournaud, F., Duc, P. -A., Brinks, E., Boquien, M., Amram, P., Lisenfeld, U., Koribalski, B. S., Walter, F. & Charmandaris, V. 2007, Science, 316, 1166

[22] Boyce, P. J., Minchin, R. F, Kilborn, V. A., et al. 2001, ApJ, 560, 127

[23] Brewer, J. P., Richer, H. B. & Crabtree, D. R. 1995, AJ, 109, 2480

[24] Brinks, E., Walter, F. & Skillman, E. 2008, in IAU Symposium, Vol. 244, Dark Galaxies and Lost Baryons, ed. J. I. Davies & M. J. Disney, 120

[25] Bureau, M. & Carignan, C. 2002, AJ, 123, 1316

[26] Bureau, M., Walter, F., van Gorkom, J. & Carignan, C. 2004, IAUS, 217, 452

[27] Caldwell, N. 2006, AJ, 651, 822

[28] Caldwell, N., Armandroff, T. E., Da Costa, G. S. & Seitzer, P. 1998, AJ, 115, 535

[29] Cardelli, J. A., Clayton, G. C. & Mathis, J. S. 1989, ApJ, 345, 245

[30] Carretta, E., Bragaglia, A., Gratton, R., D'Orazi, V. & Lucatello, S. 2009, A&A, 508, 695

[31] Carretta, E. & Gratton, R. G. 1997, A&AS, 121, 95

[32] Chiboucas, K., Karachentsev, I. D. & Tully, R. B. 2009, AJ, 137, 3009

[33] Chiosi, C., Bertelli, G. & Bressan, A. 1992, ARA&A, 30, 235

[34] Chynoweth, K. M., Langston, G. I., Yun, M. S., Lockman, F. J., Rubin, K. H. R., Scoles, S. A. 2008, AJ, 135, 1983

[35] Cignoni, M. & Tosi, M. 2010, AdAst, 2010E, 3

[36] Cole, A. A., Smecker-Hane, T. A. & Gallagher, J. S., III 2000, AJ, 120, 1808

[37] Cole, A. A., Smecker-Hane, T. A., Tolstoy, E., Bosler, T. L. & Gallagher, J. S. 2004, MNRAS. 347, 367

[38] Coleman, M. G., Da Costa, G. S. & Bland-Hawthorn, J. 2005, AJ, 130, 1065

[39] Coleman, M. G. & de Jong, J. T. A. 2008, ApJ, 685, 933

[40] Combes, F. 2009, A&A, 500, 119

[41] Courteau, S. & Rix, H.-W. 1999, ApJ, 513, 561

[42] Croxall, K. V., van Zee, L., Lee, H., Skillman, E. D., Lee, J. C., Ct, S., Kennicutt, R. C. & Miller, B. W. 2009, ApJ, 705, 723

[43] Crnojevic, D., Grebel, E. K. & Koch, A. 2010, A&A, 516A, 85

[44] Da Costa, G. S. & Armandroff, T. E. 1990, AJ, 100, 162

[45] Da Costa, G. S. & Armandroff, T. E. 1995, AJ, 109, 2533

[46] Da Costa, G. S. & Hatzidimitriou, D. 1998, AJ, 115, 1934

[47] de Mello, D. F., Smith, L. J., Sabbi, E., Gallagher, J. S., Mountain, M. & Harbeck, D. R. 2008, AJ, 135, 548

[48] Dolphin, A. E. 2000, PASP, 112, 1383

[49] Dolphin, A. E., Weisz, D. R., Skillman, E. D. & Holtzman, J. A. 2005, astro.ph 6430

[50] Dotter, A., Chaboyer, B., Jevremovic, D., Baron, E., Ferguson, J. W., Sarajedini, A. & Anderson, J. 2007, AJ, 134, 376

[51] Dotter, A., Chaboyer, B., Jevremovic, D., Kostov, V., Baron, E. & Ferguson, J. W. 2008, ApJS, 178, 89

[52] Dotter, A., Sarajedini, A., Anderson, J., Aparicio, A., Bedin, L. R., Chaboyer, B., Majewski, S., Marin–Franch, A., Milone, A., Paust, N., Piotto, G., Reid, I.N., Rosenberg, A. & Siegel, M. 2010, ApJ, 708, 698

[53] Duc, P. –A. & Mirabel, I. F. 1998, A&A, 333, 813

[54] Durrell, P. R., Harris, W. E. & Pritchet, C. J. 2001, AJ, 121, 2557

[55] Elmegreen, B. G., Kaufman, M. & Thomasson, M. 1993, ApJ, 412, 90

[56] Frayn, C. M. & Gilmore, G. F. 2002, MNRAS, 337, 445

[57] Gallart, C., Zoccali, M. & Aparicio, A. 2005, ARA&A, 43, 387

[58] Georgiev, I. Y., Puzia, T. H., Hilker, M. & Goudfrooij, P. 2009, MNRAS, 392, 879

[59] Glatt, K., Gallagher, J. S., III, Grebel, E. K., et al. 2008a, AJ, 135, 1106

[60] Glatt, K., Grebel, E. K., Sabbi, E., et al. 2008b, AJ, 136, 1703

[61] Girardi, L., Dalcanton, J., Williams, B., de Jong, R., Gallart, C., Monelli, M., Groenewegen, M. A. T., Holtzman, J. A., Olsen, K. A. G., Seth, A. C. & Weisz, D. R. 2008, PASP, 120, 583

[62] Girardi, L., Groenewegen, M. A. T., Hatziminaoglou, E. & da Costa, L. 2005, A&A, 436, 895

[63] Grebel, E. K. 1997, RvMA, 10, 29

[64] Grebel, E. K. 1999, in IAU Symposium, Vol. 192, The Stellar Content of Local Group Galaxies, ed. P. Whitelock & R. Cannon, 17

[65] Grebel, E. K. 2000, in Star Formation from the Small to the Large Scale, ed. F. Favata, A. A. Kaas, & A. Wilson (SP–445) (Noordwijk: ESA), 87

[66] Grebel, E. K. 2001, Astrophysics and Space Science Supplement, 277, 231

[67] Grebel, E. K. & Gallagher, J. S., III 2004, ApJ, 610, 89

[68] Grebel, E. K., Gallagher, J. S., III & Harbeck, D. 2003, AJ, 125, 1926

[69] Grebel, E. K. & Guhathakurta P. 1999, ApJ, 511, 101

[70] Grebel, E. K. & Roberts, W. J. 1995, A&AS, 109, 293

[71] Guarnieri, M. D., Renzini, A. & Ortolani, S. 1997, ApJ, 477, L21

[72] Gullieuszik, M., Held, E. V., Rizzi, L., Girardi, L., Marigo, P. & Momany, Y. 2008, MNRAS, 388, 1185

[73] Gunn, J. E. & Gott, J. R., III 1972, ApJ, 176, 1

[74] Harbeck, D., Grebel, E. K., Holtzman, J., Guhathakurta, P., Brandner, W., Geisler, D., Sarajedini, A., Dolphin, A., Hurley–Keller, D. & Mateo, M. 2001, AJ, 122, 3092

[75] Harris, G. L. H. & Harris, W. E. 2000, AJ, 120, 2423

[76] Harris, W. E. & Harris, G. L. H., 2002, AJ, 123, 3108

[77] Harris, G. L. H., Harris, W. E. & Poole, G. B. 1999, AJ, 117, 855

[78] Huchtmeier, W. K. & Skillman, E. D. 1998, A&AS, 127, 269

[79] Hunter, D. A., Hunsberger, S. D. & Roye, E. W. 2000, ApJ, 542, 137

[80] Hurley–Keller, D., Mateo, M. & Grebel, E. K. 1999, ApJ, 523, 25

[81] Hurley–Keller, D., Mateo, M. & Nemec, J. 1998, AJ, 115, 1840

[82] Ibata, R., Chapman, S., Irwin, M., Lewis, G. & Martin, N. 2006, MNRAS, 373, 70

[83] Iben, Icko, Jr. 1991, ApJS, 76, 55

[84] Ikuta C. & Arimoto N. 2002, A&A, 391, 55

[85] Irwin, M. & Hatzidimitriou, D. 1995, MNRAS, 277, 1354

[86] Jerjen, H. 2010, AdAst, 2010E, 2

[87] Kalirai, J. S., Gilbert, K. M., Guhathakurta, P., Majewski, S. R., Ostheimer, J. C., Rich, R. M., Cooper, M. C., Reitzel, D. B., Patterson, R. J. 2006, ApJ, 648, 389

[88] Kallivayalil, N., van der Marel, R. P. & Alcock, C. 2006b, ApJ, 652, 1213

[89] Kallivayalil, N., van der Marel, R. P., Alcock, C., Axelrod, T., Cook, K. H., Drake, A. J. & Geha, M. 2006a, ApJ, 638, 772

[90] Karachentsev, I. D., Dolphin, A. E., Geisler, D., Grebel, E. K., Guhathakurta, P., Hodge, P. W., Karachentseva, V. E., Sarajedini, A., Seitzer, P., Sharina, M. E. 2002, A&A, 383, 125

[91] Karachentsev, I. D., Dolphin, A., Tully, R. B., Sharina, M., Makarova, L., Makarov, D., Karachentseva, V., Sakai, S. & Shaya, E. J. 2006, AJ, 131, 1361

[92] Karachentsev, I. D. & Kaisin, S. S. 2007, AJ, 133, 1883

[93] Karachentsev, I. D., Karachentseva, V. E., Dolphin, A. E., Geisler, D., Grebel, E. K.. Guhathakurta, P., Hodge, P. W., Sarajedini, A., Seitzer, P., Sharina, M. E. 2000, A&A, 363, 117

[94] Karachentsev, I. D., Karachentseva, V. E., Huchtmeier, W. K. & Makarov, D. I. 2004, AJ, 127, 2031

[95] Karachentsev, I. D., Sharina, M. E., Dolphin, A. E., Geisler, D., Grebel, E. K., Guhathakurta, P., Hodge, P. W., Karachentseva, V. E.; Sarajedini, A. & Seitzer, P. 2001 A&A, 375, 359

[96] Karachentsev, I. D., Sharina, M. E., Grebel, E. K., Dolphin, A. E., Geisler, D., Guhathakurta, P., Hodge, P. W., Karachentseva, V. E., Sarajedini, A., Seitzer, P. 1999, A&A, 352, 399

[97] Karachentseva, V. E., Karachentsev, I. D., Richter, G. M., von Berlepsch, R. & Fritze, K. 1987, AN, 308, 247

[98] Kniazev, A. Y., Brosch, N., Hoffman, G. L., Grebel, E. K., Zucker, D. B., Pustilnik, S. A. 2009, MNRAS, 400, 2054

[99] Koch, A. 2009, AN, 330, 675

[100] Koch, A., Grebel, E. K., Wyse, R. F. G., Kleyna, J. T., Wilkinson, M. I., Harbeck, D. R., Gilmore, G. F., Evans, N. W. 2006, AJ, 131, 895

[101] Koch, A., Grebel, E. K., Kleyna, J. T., Wilkinson, M. I., Harbeck, D. R., Gilmore, G. F., Wyse, R. F. G. & Evans, N. W. 2007a, AJ, 133, 270

[102] Koch, A., Wilkinson, M. I., Kleyna, J. T., Gilmore, G. F., Grebel, E. K.; Mackey, A. D., Evans, N. W. & Wyse, R. F. G. 2007b, ApJ, 657, 241

[103] Koch, A., Grebel, E. K., Gilmore, G. F., Wyse, R. F. G., Kleyna, J. T., Harbeck, D. R., Wilkinson, M. I. & Wyn E. N. 2008, AJ, 135, 1580

[104] Koch, A., Odenkirchen, M., Grebel, E. K. & Caldwell, J. A. R. 2004a, AN, 325, 299

[105] Koch, A., Grebel, E. K., Odenkirchen, M., Martnez-Delgado, D. & Caldwell, J. A. R. 2004b, AJ, 128, 2274

[106] Koch, A., Rich, R. M., Reitzel, D. B., Martin, N. F., Ibata, R. A., Chapman, S. C., Majewski, S. R., Mori, M., Loh, Y. –S., Ostheimer, J. C. & Tanaka, M. 2008, ApJ, 689, 958

[107] Koposov, S., Belokurov, V., Evans, N. W., Hewett, P. C., Irwin, M. J., Gilmore, G., Zucker, D. B., Rix, H. –W., Fellhauer, M., Bell, E. F. & Glushkova, E. V. 2008, ApJ, 686, 279

[108] Kraft, R. P. & Ivans, I. I. 2003, PASP, 115, 143

[109] Lanfranchi, G. & Matteucci, F. 2003, A&A, 100, 500

[110] Lanfranchi, G. & Matteucci, F. 2007, A&A, 468, 927

[111] Lee, M. G. 1995, AJ, 110, 1155

[112] Lee, M. G., Freedman, W. L. & Madore, B. F. 1993, ApJ, 417, 553

[113] Lee, M. G., Park, H. S., Park, J. –H., Sohn, Y.–J., Oh, S. J., Yuk, I. –S., Rey, S. –C., Lee, S.–G., Lee, Y.–W., Kim, H.–I., Han, W., Park, W.–K., Lee, J. H., Jeon, Y.–B., Kim, S. C. 2003, AJ, 126, 2840

[114] Lee, M. G., Yuk, I. –S., Park, H. S., Harris, J. & Zaritsky, D. 2009, ApJ, 703, 692

[115] Lianou, S., Grebel, E. K. & Koch, A. 2010, A&A, 521A, 43

[116] Makarova, L. N., Grebel, E. K., Karachentsev, I. D., Dolphin, A. E., Karachentseva, V. E., Sharina, M. E., Geisler, D., Guhathakurta, P., Hodge, P. W., Sarajedini, A., Seitzer, P. 2002, A&A, 396, 473

[117] Marcolini, A., D'Ercole, A., Battaglia, G. & Gibson B. K. 2008, MNRAS, 386, 2173

[118] Marigo, P., Girardi, L., Bressan, A., Groenewegen, M. A. T., Silva, L. & Granato, G. L. 2008, A&A, 482, 883

[119] Martinez-Delgado, D. & Aparicio, A. 1997, ApJ, 480, L107

[120] Mateo, M. L. 1998, ARA&A, 36, 435

[121] Matthews, L. D., van Driel, W. & Gallagher, J. S., III 1998, AJ, 116, 2196

[122] Mayer, L. 2010, AdAst, 2010E, 25

[123] Mayer, L., Kazantzidis, S., Mastropietro, C. & Wadsley, J. 2007, Nature, 445, 738

[124] Mayer, L., Mastropietro, C., Wadsley, J., Stadel, J. & Moore, B. 2006, MNRAS, 369, 1021

[125] McGaugh, S. S., Schombert, J. M., Bothun, G. D. & de Blok, W. J. G. 2000, ApJ, 533L, 99

[126] McConnachie, A. W., Venn, K. A., Irwin, M. J., Young, L. M. & Geehan, J. J. 2007, ApJ, 671L, 33

[127] Menzies, J., Feast, M., Tanabe, T., Whitelock, P. & Nakada, Y. 2002, MNRAS, 335, 923

[128] Mighell, K. J. 1997, AJ, 114, 1458

[129] Mighell, K. J. & Rich, R. M. 1996, AJ, 111, 777

[130] Monelli, M., Pulone, L. & Corsi, C. E., Castellani, M., Bono, G., Walker, A. R., Brocato, E., Buonanno, R., Caputo, F., Castellani, V., Dall'Ora, M., Marconi, M., Nonino, M., Ripepi, V. & Smith, H. A. 2003, AJ, 126, 218

[131] Mori, M., Yoshii, Y., Tsujimoto, T. & Nomoto, K. 1997, ApJ, 478L, 21

[132] Mouhcine, M. & Lancon, A. 2003, MNRAS, 338, 572

[133] Mouhcine, M., Rich, R. M., Ferguson, H. C., Brown, T. M. & Smith, T. E. 2005, ApJ, 633, 828

[134] Mould, J. R. & Da Costa, G. S. 1988, ASPC, 1, 197

[135] Mould, J. R., Kristian, J. & Da Costa, G. S. 1983, ApJ, 270, 471

[136] Orban, C., Gnedin, O. Y., Weisz, D. R., Skillman, E. D., Dolphin, A. E. & Holtzman, J. A. 2008, ApJ, 686, 1030

[137] Piatek, S., Pryor, C. & Olszewski, E. W. 2008, AJ, 135, 1024

[138] Pont, F., Zinn, R., Gallart, C., Hardy, E. & Winnick, R. 2004, AJ, 127, 840

[139] Putman, M. E., Gibson, B. K., Staveley–Smith, L., et al. 1998, Nature, 394, 752

[140] Putman, M. E., Staveley-Smith, L., Freeman, K. C., Gibson, B. K. & Barnes, D. G. 2003, ApJ, 586, 170

[141] Reid, N. & Mould, J. 1984, ApJ, 284, 98

[142] Rejkuba, M., da Costa, G. S., Jerjen, H., Zoccali, M. & Binggeli, B. 2006, A&A, 448, 983

[143] Renzini, A. 1998, AJ, 115, 2459

[144] Rizzi, L., Held, E. V., Bertelli, G. & Saviane, I. 2003, ApJ, 589L, 85

[145] Rizzi, L., Held, E. V., Saviane, I., Tully, R. B. & Gullieuszik, M. 2007a, MNRAS, 380, 1255

[146] Rizzi, L., Tully, R. B., Makarov, D., Makarova, L., Dolphin, A. E., Sakai, S. & Shaya, E. J. 2007b, ApJ, 661, 815

[147] Roye, E. W. & Hunter, D. A. 2000, AJ, 119, 1145

[148] Rutledge, G. A., Hesser, J. E. & Stetson, P. B. 1997, PASP, 109, 907

[149] Sabbi, E, Gallagher, J. S., Smith, L. J., de Mello, D. F. & Mountain, M. 2008, ApJ, 676, L113

[150] Sakai, S., Madore, B. F. & Freedman, W. F. 1996, ApJ, 461, 713

[151] Sakai, S., Mould, J. R., Hughes, S. M. G., Huchra, J. P., Macri, L. M., Kennicutt, R. C., Jr., Gibson, B. K., Ferrarese, L., Freedman, W. L., Han, M., Ford, H. C., Graham, J. A., Illingworth, G. D., Kelson, D. D., Madore, B. F., Sebo, K., Silbermann, N. A., Stetson, P. B. 2000, ApJ, 529, 698

[152] Sarajedini, A., Grebel, E. K., Dolphin, A. E., Seitzer, P., Geisler, D., Guhathakurta, P., Hodge, P. W., Karachentsev, I. D., Karachentseva, V. E. & Sharina, M. E. 2002, ApJ, 567, 915

[153] Salaris, M., Cassisi, S. & Weiss, A. 2002, PASP, 114, 375

[154] Saviane, I., Rosenberg, A., Piotto, G. & Aparicio, A. 2000, A&A, 2000, 355, 966

[155] Saviane, I., Held, E. V. & Bertelli, G. 2000, A&A, 355, 56

[156] Schlegel, D. J., Finkbeiner, D. P. & Davis, M. 1998, ApJ, 500, 525

[157] Sharina, M. E., Karachentsev, I. D., Dolphin, A. E., Karachentseva, V. E., Tully, R. B., Karataeva, G. M., Makarov, D. I., Makarova, L. N., Sakai, S., Shaya, E. J., Nikolaev, E. Yu. & Kuznetsov, A. N. 2008, MNRAS, 384, 1544

[158] Sirianni, M., Jee, M. J., Bentez, N., Blakeslee, J. P., Martel, A. R., Meurer, G., Clampin, M., De Marchi, G., Ford, H. C., Gilliland, R., Hartig, G. F., Illingworth, G. D., Mack, J. & McCann, W. J. 2005, PASP, 117, 1049

[159] Smecker–Hane, T. A., Stetson, P. B., Hesser, J. E. & Lehnert, M. D. 1994, AJ, 108, 507

[160] Smecker-Hane, T. A., Stetson, P. B., Hesser, J. E. & Vandenberg, D. A. 1996, in ASP Conf. Ser. 98, From Stars to Galaxies: The Impact of Stellar Physics on Galaxy Evolution, ed. C. Leitherer, U. Fritze–von Alvensleben, & J. Huchra (San Francisco: ASP), 328

[161] Starkenburg, E., Hill, V., Tolstoy, E., Gonzalez Hernandez, J. I., Irwin, M., Helmi, A., Battaglia, G., Jablonka, P., Tafelmeyer, M., Shetrone, M., Venn, K. & de Boer, T. 2010, A&A, 513A, 34

[162] Stetson, P. B, Hesser, J. E. & Smecker–Hane, T. A. 1998, PASP, 110, 533

[163] Tolstoy, E., Hill, V. & Tosi, M. 2009, ARA&A, 47, 371

[164] Tolstoy, E., Irwin, M. J., Helmi, A., Battaglia, G., Jablonka, P., Hill, V., Venn, K. A., Shetrone, M. D., Letarte, B., Cole, A. A., Primas, F., Francois, P., Arimoto, N., Sadakane, K., Kaufer, A., Szeifert, T. & Abel, T. 2004, ApJ, 617, 119

[165] van den Bosch, F. C. 2000, ApJ, 530, 177

[166] Vanhollebeke, E., Groenewegen, M. A. T. & Girardi, L. 2009, A&A, 498, 95

[167] Venn, K. A., Irwin, M., Shetrone, M. D., Tout, C. A., Hill, V. & Tolstoy, E. 2004, AJ, 128.1177

[168] Tully, R. B. & Fisher, J. R. 1977, A&A, 54, 661

[169] Walker, M. G., Mateo, M. & Olszewski, E. W., Bernstein, R., Wang, X. Woodroofe, M. 2006, AJ, 131, 211

[170] Walker, M. G., Mateo, M. & Olszewski, E. W. 2009a, AJ, 137, 3100

[171] Walker, M. G., Mateo, M.,Olszewski, E. W., Penarrubia, J., Wyn E. N., Gilmore, G. 2009b, ApJ, 704, 1274

[172] Walker, M. G., Mateo, M. & Olszewski, E. W. 2007, ApJS, 171, 389

[173] Whitelock, P. A., Menzies, J. W., Feast, M. W., Matsunaga, N., Tanabe, T. & Ita, Y. 2009, MNRAS, 394, 795

[174] Williams, B. F., Ciardullo, R., Durrell, P. R., Vinciguerra, M., Feldmeier, J. J., Jacoby, G. H., Sigurdsson, S., von Hippel, T., Ferguson, H. C., Tanvir, N. R., Arnaboldi, M., Gerhard, O., Aguerri, J. A. L. & Freeman, K. 2007, ApJ, 656,756

[175] Williams, B. F., Dalcanton, D. J., Seth, A. C., Weisz, D., Dolphin, A., Skillman, E., Harris, J., Holtzman, J., Girardi, L., de Jong, R. S., Olsen, K., Cole, A., Gallart, C., Gogarten, S. M., Hidalgo, S. L. Mateo, M., Rosema, K., Stetson, P. B. & Quinn, T. 2009, AJ, 137, 419

[176] Willman, B. 2010, AdAst, 2010E, 21

[177] Yun, M. S. 1999, in IAU Symposium 186, Galaxy Interactions at Low and High Redshift, ed. J. E. Barnes & D. B. Sanders, 81

[178] Yun, M. S., Ho, P. T. P. & Lo, K. Y. 1994, Nature, 372, 530

[179] Zinn, R. & West, M. J. 1984, ApJS, 55, 45